Topics in Galaxy Evolution: Early Star Formation and Quenching

Thesis by

Thiago Signorini Gonçalves

In Partial Fulfillment of the Requirements

for the Degree of

Doctor of Philosophy
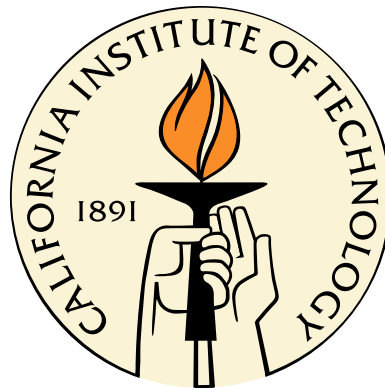
California Institute of Technology

Pasadena, California

2012

(Defended August 26, 2011)

"Ora direis ouvir estrelas! Certo
Perdeste o senso"! E eu vos direi, no entanto,
Que, para ouvi-las, muita vez desperto
E abro as janelas, pálido de espanto...

E conversamos toda a noite, enquanto
A via láctea, como um pálio aberto,
Cintila. E, ao vir do sol, saudoso e em pranto,
Inda as procuro pelo céu deserto.

Direis agora! "Tresloucado amigo!
Que conversas com elas? Que sentido
Tem o que dizem, quando estão contigo?"

E eu vos direi: "Amai para entendê-las:
Pois só quem ama pode ter ouvido
Capaz de ouvir e de entender estrelas."

Olavo Bilac

Acknowledgements

This has been quite a journey. For a long time I have struggled, learned, struggled a bit more, learned much more, and in the end I come out - gasp! - an astronomer, a doctor, a scientist, whatever tag you may want to put on me, but certainly not the same person I was seven years ago. And undoubtedly there are several people I wish to thank (blame?) for this transformation and this journey.

First of all, I believe I should thank Chris Martin, my advisor. Chris has always believed in me and has given me all the necessary tools and resources to conduct my research and take it to new places. On many occasions, through his advice he has pointed me in the right direction, offering keen insights that have helped me advance.

He was not alone, though. I would also like to thank the whole GALEX team, who was always very welcoming and friendly – not to mention a nice crowd to share some fun moments during team meetings, including nice skiing winter days in Aspen and the culinary experience in Paris.

From the team, I wish to mention two people who have helped me particularly. First, a big thank you to Todd Small, who has shown me the ropes of, well, everything, from IDL coding to observing procedures at Keck. Todd certainly helped me hit the ground running once I joined GALEX, and I really appreciate that. In that same spirit, a warm thank you to Ted Wyder, who was a big help all throughout my PhD, always willing to comment on papers and offer friendly advice. Ted was particularly helpful during the last few months and weeks before this document was done, and certainly an integral part of the process.

I should also mention all the people who, as stated before, made the GALEX experience a pleasant one. Kudos to Don Neill, Patrick Morrissey, Karl Forster.

Many, many thanks to Min Hubbard – you are such a cheerful person, and certainly made the group more personable with your great efforts and the incredible cakes. Suvi Gezari, very fun to hang with you in fun places, and thanks for the nice weather at Keck; I know it was you somehow. And David Schiminovich and Tim Heckman, who offered good advice and were very kind to help me at all stages during the job search.

Finally, a big thank you to Antara Basu-Zych and Roderik Overzier. Both have balanced the roles of friend and colleague remarkably well, and the LBA projects, in particular what you can read in Chapter 2, is their merit, too. I honestly hope we can keep collaborating on this, because (1) it is awesome science, and (2) it has been great fun to work with you guys.

However, that is not the only group with which I interacted as a PhD student. Certainly other students in the department, classmates or otherwise, have been a big part of my Caltech experience. I guess I should start with classmates, so thank you Dan Grin, Ann Marie Cody and Hilke Schlichting for the good times. Those all-nighters in the first-year office were quite memorable, and just in case I risk forgetting, I will always keep the infamous compilation of quotes spilled out in moments of rage and frustration.

Other students were just as great companions. Laura Pérez and Walter Max-Moerbeck, you guys will be missed; good thing Santiago and Rio are not that far. Besides, on top of being a great friend, Laura was a great, great help with all the CARMA data. A special note to David and Sarah Law; David was much more than a collaborator, and Sarah a very endearing (albeit foot-munching) person. I don't want you to go to Toronto! Milan Bogosavljević was a good friend, sharing moments at Shorinji Kempo and Coachella. And of course Elisabeth Krause, excellent travel companion – you have to come visit us now so we can have more trips together! I would also like to thank Varun Bhalerao, whose amazing work taking care of outreach in the department is worthy of praise. That was incredibly inspiring, and I just wish I had had more time or discipline to do more in that area – hopefully I'll have the chance now.

And then there was everyone else in the Astronomy Department. Kartik Sheth, Kalliopi Dasyra, Johan Richard, Greg Herczeg, I very much hope we can at least run into each other in meetings; but you are living in great places, so I'll make sure to come and visit you at some point. Isa, so great you could spend some time in town! Michel and Fredeique, I hope we get see Chloe before she is all grown up. Some professors I would like to mention include Tony Readhead and the more recent arrivals, Chris Hirata and John Johnson. These people work hard to make Caltech a better place, and I thank you for it.

Thanks are due to all the people who help maintain Caltech as such a pleasant place. I wish I could name them individually; at least I can mention Marta and Elvira, always so warm, and always asking me about Karín. And I guess this has become commonplace now, but I cannot write this without thanking Ernie for keeping us all well-fed, both physically and spiritually, with good food and broad smiles.

I did not have much time to meet people outside Caltech during my time in Southern California, but the ones I met were special. First and foremost, J.J and John, such a big piece of the puzzle, and such a great comfort, always there in times of need (broken collarbone, I'm looking at you). Sundays will not be the same without Porto's.

How can I not mention all my loved ones in Brazil? Although you all are 10000 km away, you were with me the whole time. All the Miguellitos, I missed you terribly during this whole time. Pedro, Camelo, Aninha, words escape me to explain our friendship. My CAp classmates, same thing; Thais, João Felipe, all the good times of a childhood that thankfully never ends. Man, it feels great to go back home. Oh, and I will individually mention, in addition, all the dear ones who have visited me: Eric, Mari, Manu. Just to make the other ones feel guilty. One other friend I should name is Beto; he was always an inspiration, making me look at Physics and Science a whole different way.

And how can I not mention my parents? They would kill me. And rightly so, they have been the ones who have always put their faith on me. Whenever I was down, stressed, frustrated, they would confront me and make me see how they think

the world of me, and make sure I would never feel inferior or subdued. From the get go, from the moment I left Brazil, they both made it clear how they would miss their only son, but made sure I never regretted my decision. Ligia, the sister I never had – I am coming back to Brazil and you leave for Australia, what is up with that? And my dear grandmother Dulce, stubborn as a mule, used to say she wouldn't make it pass 70 and here she is, at 81. Te amo, vó.

And last, but never least, Karín. My goodness, what would these seven years have been without you? It's not hard to imagine - it's simply surreal. You have been with every. Single. Step. Good, bad, you were there with me and for me. And I love you even more for it. The only way I can repay you is to be there, just as you were, supporting and caring. If you made it through nearly seven years, I guess you can take some more.

Ok, I'll stop here, since this is already sappy beyond belief. On with the science.

Abstract

In this thesis, we present three projects designed to shed light on yet unanswered questions on galaxy formation and evolution. The first two concern a sample of UV-bright starburst galaxies in the local universe ($z \sim 0.2$). These objects are remarkably similar to star-forming galaxies that were abundant at high redshifts ($2 \lesssim z \lesssim 3$) – the Lyman break galaxies – and can help explain the very distinctive properties observed at such epochs. Thus, these galaxies are denominated Lyman break analogs, or LBAs.

First, we describe a survey of kinematics of the nebular gas in such objects, and how that can help explain the formation process, including gas assembly, in these starbursts. We show strong evidence that the gas kinematics resemble those observed at high redshifts. However, by artificially manipulating our observations to mimic our objects at greater distances, we show how low resolution and signal-to-noise ratios can lead to erroneous conclusions, in particular when attempting to diagnose mergers as the origin of the starburst.

Then, we present results from a pilot survey to study the cold, molecular gas reservoir in such objects. Again, we show that the observed properties are analogous to those observed at high redshift, in particular with respect to baryonic gas fractions in the galaxy, higher than normally found in low-extinction objects in the local universe. Furthermore, we show how gas surface density and star-formation surface density follow the same relation as local galaxies, albeit at much higher values.

Finally, we discuss an observational project designed to measure the mass flux density from the blue sequence to the red sequence across the so-called green valley. We obtain the deepest spectra ever observed of green valley galaxies at intermediate redshifts ($z \sim 0.8$) in order to measure spectral features from which we can measure

the star formation histories of individual galaxies. We measure a mass flux ratio that is higher than observed in the local universe, indicating the red sequence was growing faster when the universe was half its present age than today.

Contents

List of Figures

List of Tables

Chapter 1

Introduction

This is a work on galaxy formation and evolution. And the fact is, there is much still unknown (or as yet undiscovered) about the formation and evolution of galaxies across cosmic time – hence why this is such an active field of research within astrophysics. Therefore, what better way to introduce such work with what we actually know – or believe we know - on the topic?

1.1 The Hubble Sequence – galaxies in the local universe

To begin this argument, one should define first what a galaxy is. In the early 1920s, such a definition did not exist. Astronomers could observe *spiral nebulae*, as they were called at the time, but their nature was still unclear. Two papers with discrepant characterizations of such nebulae were published in 1921, in what became known as the Great Debate; the first argued that these objects were part of our own Milky Way, which comprised the entirety of the universe (Shapley, 1921), while the second contended that these nebulae were in fact *island universes*, comparable in size to our own galaxy but separate entities (Curtis, 1921).

Edwin Hubble (1925) settled the debate through observations of Cepheid variables in other galaxies. By using those stars as standard candles (Leavitt, 1908), he was able to infer distances to several nebulae, including the Andromeda Galaxy (M31) and the Triangulum Galaxy (M33). Since the measured distances were too great

in comparison with objects in the Milky Way, it could only be assumed those were galaxies outside our own, after all.

The modern definition of a galaxy, as found in a dictionary, is the following: "Any of numerous large-scale aggregates of stars, gas, and dust that constitute the universe, containing an average of 10^{11} solar masses and ranging in diameter from 1,500 to 300,000 light-years." (The American Heritage Dictionary, 2006).

Now that astronomers knew what a galaxy was, the following job was to classify them. Edwin Hubble was again the pioneer in this field, differentiating primarily between elliptical and spiral galaxies, in addition to irregular galaxies that do not show any obvious structure (Hubble, 1926, see Figure 1.1). This work was very influential, and subsequent classification systems drew heavily from Hubble's seminal paper (e.g., de Vaucouleurs, 1959; Sandage, 1961).

Furthermore, it was seen that the galaxy morphology, whether spiral, elliptical or other kind, was closely related to other properties. de Vaucouleurs (1961) noticed how late-type galaxies (spirals and irregulars) show typically bluer colors, indicating younger stellar populations, while early types, such as ellipticals and lenticulars, tend to be redder, with older stellar populations. Furthermore, Dressler (1980) found that galaxy morphologies are closely related to their environment, with ellipticals and lenticulars being more prevalent in dense environments such as clusters.

But how do galaxies form? How is the spiral structure in a galaxy created from a gas reservoir? One early attempt to explain the process of galaxy formation was made by Eggen et al. (1962). In that work, the authors suggest galaxies form from a monolithic collapse of a large gas cloud, which gradually cools down; the initial angular momentum of the cloud would generate a disk of rotating material, and first-generation stars would enrich the interstellar medium with heavy elements formed in their interiors.

Later, astronomers started to consider the hierarchical formation scenario, in which galaxies do not form from the collapse of a single cloud, but instead are the result of a series of interactions and mergers between smaller objects, which come together in order to form the structures we see in the universe today (White & Rees,
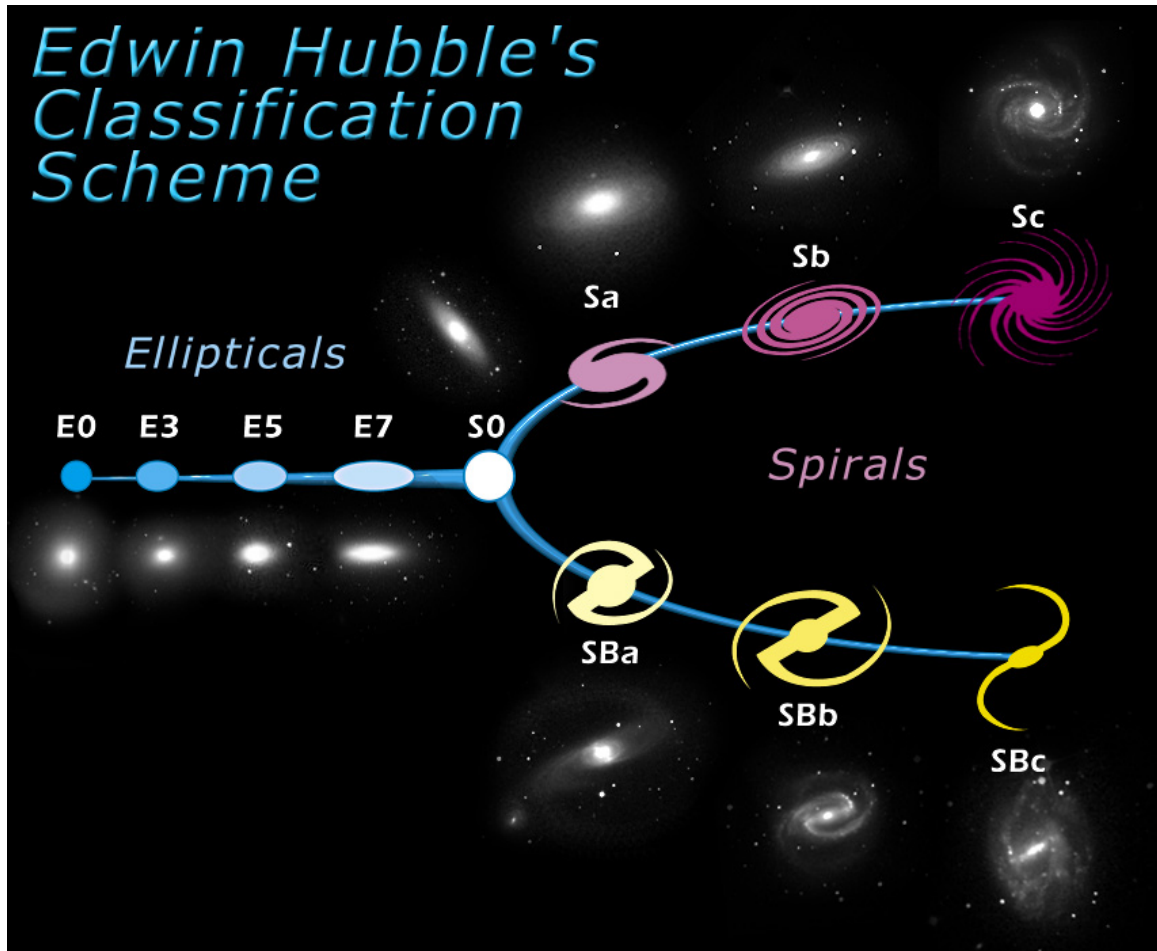
Figure 1.1: Edwin Hubble's tuning fork, differentiating between elliptical (*left*) and spiral galaxies (*right*). Elliptical galaxies are classified according to sphericity (more spherical galaxies to the left), while spiral galaxies are classified as a function of arm strength (Sc's, to the right, have arms more tightly wound and smaller central bulges than Sa's, to the left). Furthermore, Hubble divided spirals into barred and non-barred, depending on the presence of a bright line, or bar, running through their center. (Credit: Space Telescope Science Institute)

1978; Fall & Efstathiou, 1980).

1.2 The Distant Universe – uncovering details of galaxy formation/evolution

At the time those studies were undertaken, most of the attention was geared solely to galaxies in the local universe. The mere detection of galaxies at cosmological redshifts was a challenge, a notable exception being exceptionally bright quasars (e.g., Schmidt, 1963). A number of surveys at low redshift have been done – for instance the CfA Redshift Survey (Huchra et al., 1983) and the Palomar Observatory Sky Survey II (Reid et al., 1991) – but these covered only a small fraction of cosmic time. This has been dramatically changed with the advent of CCD detectors, more efficient than the previous generation photographic plates. With CCDs, detector quantum efficiencies jumped from $\sim 10\%$ to approximately 90%. At the same time, the immediate digitalization of data made handling and reduction easier and more flexible.

The prime example of the advance made possible in the electronic era is arguably the Hubble Deep Field (Williams et al., 1996), at the time the deepest optical astronomic image ever taken using the WFPC2 instrument. One of the Hubble Space Telescope's main objectives was to study galaxies at early epochs, and with that in mind, astronomers have pointed the instrument towards a dark patch of the sky (area 5.3 arcmin^2) for ten consecutive days. The resulting image showed a wealth of high-redshift galaxies, up to $z \sim 6$, indicating the vast amount of information available at these distances. A subsequent survey with the more recent ACS instrument has produced a new record holder for the deepest image (the Hubble Ultra Deep Field, Beckwith et al., 2006).

Blindly staring at dark patches in the sky is arguably an unbiased method to probe for faint distant galaxies. However, the subsequent spectroscopic confirmation of individual objects is very time and resource consuming. The need for an efficient

means of selecting high-z galaxies has led to the advent of wide-field broad-band surveys relying on the "drop-out technique." The pioneering study by Steidel et al. (1996) exploited the Lyman Break, i.e., the flux deficit blueward of the ionization energy of the hydrogen atom (912 Å), to select drop-out candidates from optical filters: at redshifts close to $z \sim 3$, the Lyman break falls between the u and g filters and the object, clearly detected in the redder bands, is not detected in the bluest one (Figure 1.2). This has been a remarkably successful technique, and has been extended to different redshifts using differents sets of filters; likewise, slightly modified surveys have made use of observed optical colors in different bands to select rest-frame ultraviolet-bright objects (e.g., the BM/BX galaxies Steidel et al., 2004) or K-band bright galaxies at redshift $z \sim 2$ (the $BzKs$, Daddi et al., 2004).
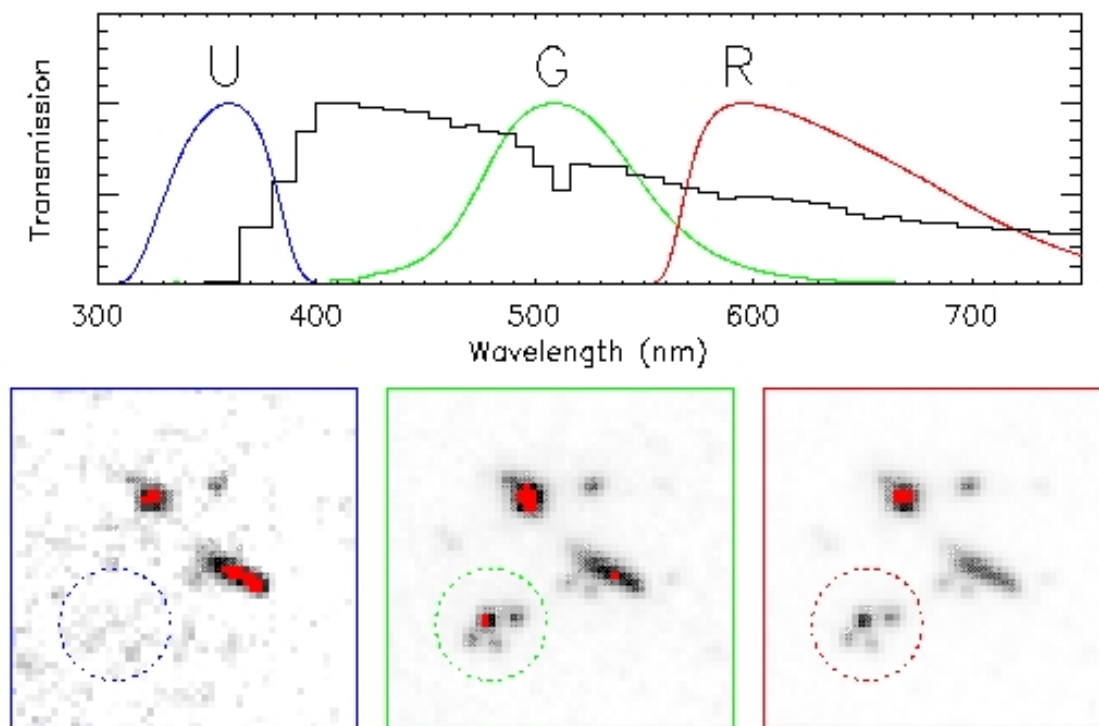
Figure 1.2: Illustration of the Lyman break technique. *Top*: Synthetic spectrum of a $z \gtrsim 3$ galaxy as a function of observed wavelength; notice the absence of flux in the U-band. *Bottom*: Images of an actual Lyman break galaxy. Flux is negligible in the bluest filter. (Credit: Johan Fynbo)

Along with independent techniques for other galaxy selection methods at high

redshift (SMGs, Blain (2002), DOGs, Dey et al. (2008), the use of other instrinsic spectral breaks, such as the Balmer/4000Å break, Franx et al. (2003); see also Shapley 2011), our knowledge over the high-redshift universe has increased exponentially in the last 15 years. Putting all that information together has produced some impressive results. One of the main discoveries coming from these surveys is *downsizing*. The term has been applied for a wide variety of results, but in general it means the shifting of scaling relations towards fainter, less massive galaxies at lower redshifts, or equivalently, an enhancement of activity in more massive galaxies at high-z. One prime example of downsizing is the finding that star-forming galaxies are typically less massive in the local universe than they were several billion years ago (Cowie et al., 1996; Noeske et al., 2007). This type of evolution can also be seen in a variety of physical properties of galaxies, such as stellar mass (Conselice et al., 2007), metallicities (Erb et al., 2006a) and AGN activity (Ueda et al., 2003).

Furthermore, in more general terms, it has been determined that the universe was forming more stars per unit volume at redshift $z \sim$ 2-3 by more than an order of magnitude (Madau et al., 1996; Hopkins & Beacom, 2006, and references therein; see also Figure 1.3). Later, different authors have noted that properties of high-redshift galaxies such as metallicities (Erb et al., 2006a) and morphologies (van den Bergh, 2002; Law et al., 2009; Delgado-Serrano et al., 2010) did not resemble what we see in the local universe. The evolution in such fundamental properties leads to the conclusion that the formation mechanisms operating at high redshift are markedly different from those operating today; but do we have plausible models explaining how these galaxies actually form?

1.3 Theoretical progress and gastrophysics

What insight can theorists offer? If there were a number of technical advances in terms of observational extragalactic astrophysics in the last 20 years, certainly the same can be said about numerical simulations of galaxy formation.

Theoretical astrophysics is capable of generating N-body models that trace the
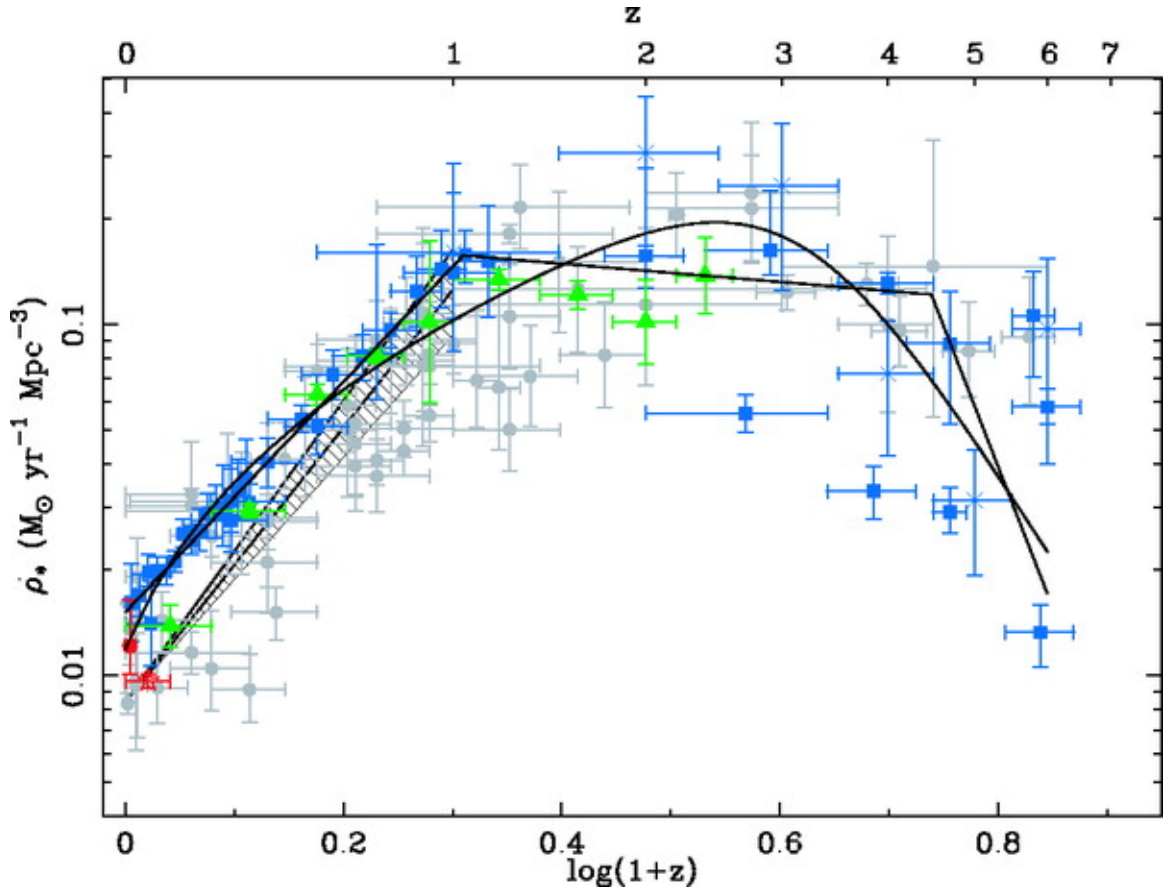
Figure 1.3: Star-formation rate density of the universe as a function of redshift, measured from a variety of surveys at different redshifts. Blue points represent UV data, green points are from 24 μm surveys and the red symbols represent Hα surveys in the low-redshift universe. The gray points are a combination of results from different wavelengths present in Hopkins (2004). Solid lines represent best-fitting parametric forms to the data. Although the location of the peak is still subject to debate, the diagram shows clearly how the universe was forming stars at a substantially higher rate 10 billion years ago. (Hopkins & Beacom, 2006, and references therein)

formation of the large-scale structure of the universe since the Big Bang, using cold dark matter (CDM, Peebles, 1982) as the foundation of choice for the growth of structures from initial perturbations, as seen imprinted on the cosmic microwave background radiation (Smoot et al., 1992; Spergel et al., 2007).

Assuming this CDM cosmological model, N-body simulations have evolved considerably since Davis et al. (1985) simulated 32,768 particles in a $32h^{-1}$ box to investigate hierarchical clustering. The Millennium simulation (Springel et al., 2005), for instance, has used more than 10 billion particles in a $500h^{-1}$ box, achieving remarkable progress in reproducing the observed growth of structure, in great part due to powerful computing resources made readily available in the past decades. The resulting merger trees are then used in semi-analytic models, which use approximations of the underlying physics on top of the galaxy haloes produced in simulations to predict galaxy properties within a cosmological volume (e.g., Croton et al. 2006; Benson & Bower 2010; see also Baugh 2006).

Although numerical simulations reproduce the growth of the large-scale structure in the universe, the small-scale, nonlinear baryonic physics that goes into forming the galactic structure remains an open question. The so-called gastrophysics, comprising AGN feedback and supernova winds among other processes, is still poorly understood. Simulations rely on *ad hoc* recipes, which are in turn based on observational results and are purely phenomenological; the underlying physical processes are not yet known.

The traditional paradigm of galaxies forming from slowly cooling shock-heated gas (e.g., White & Rees, 1978; Mo et al., 1998; Baugh, 2006, and references therein) does not seem to apply in many cases. An elevated fraction of galaxies at high redshift display clumpy structures (Elmegreen et al., 2008), which might form from internal instabilities (Noguchi, 1999; Immeli et al., 2004; Bournaud et al., 2007) or, alternatively, from mergers of subgalactic gas clumps (Taniguchi & Shioya, 2001), in agreement with the idea of hierarchical galaxy formation in LCDM models. Furthermore, recent numerical simulations indicate that star formation at high redshift might be fed through cooling flows supplying the centers of dark matter haloes directly with

gas at just below the virial temperature (Dekel & Birnboim, 2006; Dekel et al., 2009; Kereš et al., 2009). This could explain the extreme star formation rates observed at high redshift, because gas is more efficiently injected into small volumes.

Another hypothesis considered for triggering starbursts at high redshift is that galaxies merge together at a higher rate, and the gas is compressed to high densities, forming stars at very high rates (Hernquist, 1989; Barnes & Hernquist, 1992). There is much evidence that most ultra-luminous infrared galaxies, which are undergoing extreme starburst events, are also the result of major mergers, often being present in pairs or showing tidal tails (Sanders et al., 1988; Veilleux et al., 2002). In fact, if the gas fraction is high enough, disks could even be formed shortly after the merger event (Robertson et al., 2006).

Hence, it becomes evident how gas is such a fundamental component in galaxy-formation models. Are high-redshift galaxies forming through the inflow of gas or is it being compressed through mergers and interactions? Exactly how gas-rich are these objects, and does the gas component correlate with other physical properties in the galaxy? We know stars in galaxies form from the collapse of cold gas, but we don't yet know how that gas is assembled, cooled and processed at high redshifts, especially for such high indices of star-formation rates per unit volume.

1.4   Evolution from the blue to the red sequence

If the formation of galaxies still has a range of unanswered questions, the same can be said about the subsequent evolution of galaxies and quenching of star formation. It is still unclear what processes drive the decrease in star-formation rate in blue spiral galaxies, converting them into passively evolving elliptical galaxies (Figure 1.4).

A number of processes are evoked to explain this evolution. In the local universe, authors cite secular evolution within a spiral galaxy, in which bar structures rearrange gas and drive material into the center of the galaxy, generating a pseudobulge with increased star-formation rates (Kormendy & Kennicutt, 2004, and references therein). This would generate the morphologies observed in red galaxies, while at the same time

exhaust the gas reservoir and quench star-formation activity after a few Gyr (Masters et al., 2011).

The process may be more complicated, though. Di Matteo et al. (2005) and Springel et al. (2005) have produced hydrodynamical simulations in which major merger events fuel the formation of active galactic nuclei (AGN) in the center of the coalesced object. The AGN, in turn, produces strong winds that drive out the remaining gas, efficiently quenching star formation.

Whether we can observationally determine a correlation between AGN activity and star-formation quenching remains an open question. There appears to be a high fraction of AGN hosts in objects transitioning between both populations, but the AGN duty cycle and quenching timescales do not necessarily agree with the aforementioned models (Martin et al., 2007; Nandra et al., 2007; Schawinski et al., 2009). At the same time, there is no clear evidence that more luminous AGN represent faster quenching of star formation (Martin et al., 2007). As we can see, this is simply not yet solved, and further investigation of the physical processes involved is required (for a more detailed discussion, see Chapter 4).

1.5 This thesis – topics on galaxy formation and evolution

As we have seen, there remain a number of unsolved questions on the problem of how galaxies form and evolve. In this thesis we have attempted to offer new information on these problems by looking at distinct populations at redshifts $0.1 < z < 0.9$, covering approximately half the age of the universe and during which period there has been great evolution in galaxy properties and the content of the universe (see Figure 1.3).

In the two following chapters, we describe two distinct projects designed to make use of the Lyman break analog sample. This low-redshift ($z \sim 0.2$) sample presents great similarities to star-forming galaxies at redshift $z = 2$, but their proximity allows for a much more detailed study of the physical processes currently taking place, over-
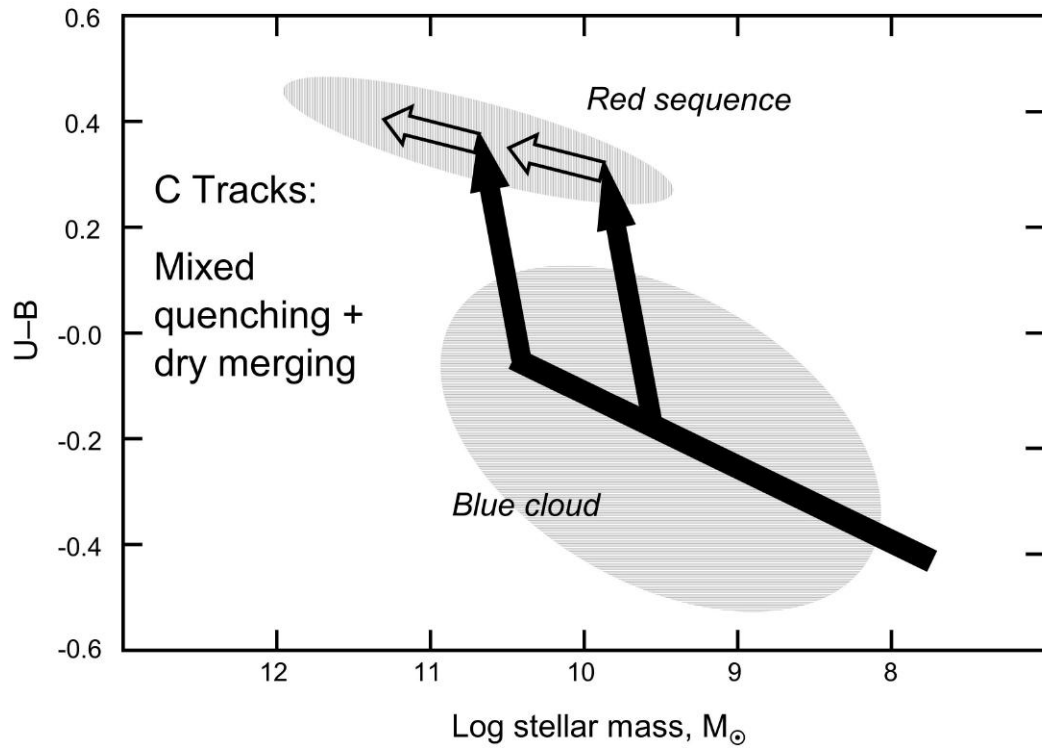
Figure 1.4: .
Schematic view of galaxy evolution in the color-magnitude diagram. Abscissa axis represents absolute magnitudes, while ordinate shows galaxy colors, with blue on the bottom and red on the top. Generally speaking, the "blue cloud" is composed of star-forming spirals and starbursts, while elliptical galaxies, which are mostly passively evolving, populate the red sequence. The scenario showed in this figure combines quenching of star formation in blue galaxies (black solid arrows) with evolution across the red sequence due to dry merging , i.e., the merger of passively evolving, gas-poor ellipticals (hollow arrows; figure from Faber et al., 2007).

coming hurdles generated by low signal-to-noise ratios and poor angular resolution. We present the sample in detail, including selection criteria, in Section 2.2.1.

The first project aims to study the kinematics of the nebular gas in Lyman break analogs. This remains one of the most active fields on the study of high-redshift galaxy formation, and the question of whether these extreme starburst galaxies are regular rotating disks or else present an irregular velocity field, more characteristic of mergers and interactions, can offer clues towards their formation mechanisms and the trigger for the observed starbursts. However, when compared to galaxies at $z \sim 2$, Lyman break analogs offer better resolution by a factor of 3, and less cosmic dimming by a factor of almost 200.

The second project aims to study the molecular gas reservoir in this sample. It has been inferred that gas fractions at high redshift are much higher (Erb et al., 2006b; Daddi et al., 2010a; Tacconi et al., 2010), offering a considerable amount of fuel for the formation of stars in these objects. However, at the same time, star-formation rates can be very high as well, in some cases so much so that the timescales for gas depletion (assuming no replenishing of the gas) is shorter than expected in the local universe (e.g., Genzel et al., 2011). At lower redshifts, the detection of molecular gas is considerably easier, and we observe a subsample of Lyman break analogs in search of connections with the high-redshift universe, as well as new insight into the interplay between star-forming regions and the gas reservoir.

The goal of the project described in the fourth chapter concerns not the formation, but the late evolution of galaxies, in an effort to characterize the quenching of star formation and the resulting transformation of spirals into red ellipticals. With that in mind we have selected a sample of intermediate color galaxies at redshifts between $0.55 < z < 0.9$, and have taken extremely deep spectra, pushing the limits of the Keck telescope and integrating for approximately 8 hours per object mask. This is arguably the deepest spectra ever taken of such a sample at these epochs.

With that data in hand, we have compared measured spectral features with synthetic models to infer star formation histories of individual galaxies. In conjunction with measured stellar masses and the observed number density of galaxies, that allows

us to measure the amount of mass traversing the region of intermediate colors per unit time, in what will eventually become the red sequence of galaxies today. This is a reproduction of the method developed in Martin et al. (2007), only now performed for higher redshift galaxies. We can therefore trace the evolution of the mass flux across cosmic time.

This thesis is organized as follows. Chapter 2 describes a survey we have performed to study the kinematics of the nebular gas in Lyman break analogs. We show our results and how they support our analogy hypothesis. We also discuss the implications for formation mechanisms at low and high redshift. Chapter 3 then presents our recent work involving millimeter interferometry observations and the search for molecular gas in these objects. Once again, we show how this supports the analogy between LBAs and LBGs, and discuss the insights into the relation between gas and star formation in UV-bright starburst galaxies. Finally, in Chapter 4 we attempt to determine the mass flux from the blue to the red sequence and the star-formation quenching timescales at higher redhifts. We show how this process has evolved in the last ~ 6 billion years, and discuss this evolution in light of the observed downsizing of scaling relations in the universe. We summarize all results in Chapter 5, and offer perspectives for future work related to all aforementioned projects.

Chapter 2

Kinematics of the nebular gas in LBAs

2.1 Introduction

Our understanding of galaxy formation has changed considerably over the course of the last two decades. As we have seen in the previous chapter, while great advances have been made in the field of galaxy formation modelling and simulations, still the processes occurring in small scales (of a few kpc) are not entirely understood, due to the complications of baryonic physics. In other words, while the assembly of mass into haloes and clusters is reproducible in numerical models, the cooling of gas and subsequent conversion into star formation within individual galaxies is still hard to simulate, and must rely heavily on observations instead of primary physical principles.[1]

In this context, it becomes important to analyze the kpc and sub-kpc scale kinematics in these galaxies, and to confront the relative contributions from ordered rotation, random motions and merger-induced features with predictions from the aforementioned models. Because *stellar* kinematics at high redshift are largely beyond reach of current instruments and telescopes, the bright nebular emission line gas is often used as a tracer for the underlying kinematics

In an early attempt to study kinematics of star-forming galaxies at $z \sim$ 2–3,

---

[1]This chapter has been published in similar form as Gonçalves et al. (2010).

Erb et al. (2006b) analyzed one-dimensional spectra of Hα emission in UV-selected galaxies (Steidel et al., 2003, 2004), detecting significant velocity shears in 12% of the objects in their sample. In all cases, velocity dispersion in the ionized gas was high in comparison with the observed velocity shears, with $v_{\rm c}/\sigma \sim 1$. These observations are challenging, since they are seeing-limited and slit-alignment plays an important role in actually detecting any shears (Erb et al., 2006b; Law et al., 2006).

More recently, Law et al. (2009) improved on this result, with spatially resolved kinematics of the gas from adaptive-optics (AO) assisted integral-field spectroscopy of 12 star-forming galaxies at redshift $z \sim 2.5$. This technique has the advantage of not depending on alignment choice, detecting velocity shears all across the extent of the galaxy, while the AO system resolves features at sub-kpc scales. The authors detect, again, high velocity dispersion values of $\sigma \simeq 60$–70 km s^{-1}. In most cases there is no evidence for ordered rotation across the galaxy, and in general the gas dynamics appear to be dominated by random motions. The authors also find a mild trend of rotational properties with stellar mass, with massive galaxies displaying more pronounced velocity shears.

In a similar study, Förster Schreiber et al. (2009) studied a large sample of 62 star-forming galaxies at similar redshifts with the SINFONI instrument. This work differs from Law et al. (2009) in that most observations are seeing-limited, with spatial resolution elements of approximately 4 kpc. In addition, most galaxies in this sample were drawn from the BzK sample of Daddi et al. (2004), and are typically 2 times as massive as the UV-selected galaxies. The authors found that their sample can be subdivided into three groups: rotation-dominated objects, with pronounced velocity shears and $v_{\rm c}/\sigma$ values of up to 4; dispersion-dominated objects, with little to no velocity shear across the major axis; and mergers, with multiple components or peculiar velocity profiles. In addition, Förster Schreiber et al. (2009) also found a trend of properties with stellar mass, with more massive galaxies presenting higher v_c/σ ratios and larger sizes. A number of observations at intermediate and high redshifts also support the hypothesis of extreme starbursts being protodisks resulting either from minor mergers or smooth accretion from the intergalactic medium (Bouché

et al., 2007; Cresci et al., 2009; Wright et al., 2009).

Jones et al. (2010) also studied the kinematics of the ionized gas in high-redshift star-forming galaxies, but a sample of strongly lensed objects was used instead. The authors were then able to reconstruct the kinematic structure from models of the gravitational lens, achieving much higher spatial resolution ($\sim$100 pc) in one spatial dimension. Out of a sample of six objects, five display characteristics of rotating gas disks, again with trends in velocities as a function of size and dynamical mass. Although the results help us understand the dynamical structures of such galaxies, it is challenging to construct a statistically significant sample of lensed objects. Additionally, in many cases the major axis is not aligned with the lens shear, in which case the velocity shear comprises few resolution elements in the data.

Studies to date explore complementary regions of parameter space. The difference in the prevalence of different kinematics observed is probably a function primarily of parent sample, compounded with differences in the sensitivity regime of different techniques. The benefit of AO is that it obtains greater spatial resolution but misses low surface brightness features (if present), while non-AO probes lower surface brightnesses and larger radii but with less fidelity. In both cases observations are technically challenging, due to the distance to the galaxies, which results in low intrinsic spatial resolution and surface brightness dimming issues. Therefore, it is advantageous to observe similar galaxies at lower redshifts in order to assess whether certain features derived from observations at high redshift are intrinsic or biased due to observational effects.

Heckman et al. (2005) have selected a sample of UV-bright galaxies in the low-redshift universe ($z \sim 0.2$) from GALEX data (Martin et al., 2005), referred to as ultraviolet-luminous galaxies (UVLGs). The authors found that these galaxies could be subdivided into two main groups, one consisting of massive spirals, and the other consisting of compact objects with intense star-formation rates. Hoopes et al. (2007) further expanded this analysis, classifying UVLGs with respect to their FUV surface brightness.

The UV characteristics for the most compact of these galaxies, the supercompact

UVLGs, were chosen to match those of typical LBGs (e.g., $L \sim L^*_{z=3}$, where $L^*_{z=3}$ is the characteristic luminosity of LBGs at $z \sim 3$). Hoopes et al. (2007) found that these objects indeed present similar properties to star-forming galaxies at higher redshift, with comparable star-formation rates, colors and metallicities, as inferred from their SDSS spectra. Basu-Zych et al. (2007) also determined, from radio continuum and mid-infrared observations, that these objects have significantly less dust attenuation when compared to galaxies of similar star-formation rates in the local universe, as is the case for LBGs. We will therefore refer to these galaxies as Lyman break analogs (LBAs) for the remainder of this chapter.

To study the morphologies of LBAs, Overzier et al. (2009, 2010) obtained HST ultraviolet and optical imaging of 30 galaxies. In general, their ultraviolet morphologies are dominated by clumpy features indicative of massive and compact star-forming regions. Many of them show clear signs of recent merger events. Interestingly, when the data are redshifted to $z \sim 2$–3, their morphologies are remarkably similar to LBGs at these epochs (e.g., Giavalisco et al., 1996; Papovich et al., 2005; Law et al., 2007b), while the subtle, low surface brightness merger features tend to disappear even in the deepest rest-frame UV or optical imaging data. This implies that on the basis of morphologies alone, it cannot be ruled out that LBGs grow through clumpy accretion and mergers, perhaps together with rapid gas accretion through other means (Overzier et al., 2010).

Furthermore, strong hydrogen lines and compact sizes make them ideal candidates for IFU spectroscopy. In Basu-Zych et al. (2009a), we presented preliminary results of this survey for three LBAs, showing how these galaxies resemble the kinematic structures of high-redshift star-forming galaxies. In this work, we expand the sample to investigate the ionized gas kinematics of 19 LBAs, observed with spatial resolution down to ~ 200 pc. The chapter is divided as follows: in Section 2, we describe the data acquisition and analysis, including target selection and how we artificially redshift our data to $z = 2.2$ in order to make direct comparisons with LBGs; in Section 3, we describe properties of individual objects; in Section 4 we describe our results, including general trends for these galaxies; in Section 5 we discuss and analyze the

results described in the previous section, and in Section 6 we summarize our findings.

Throughout this chapter, we assume standard cosmology, with $H_0 = 70$ km s^{-1} Mpc^{-1}, $\Omega_m = 0.30$ and $\Omega_\Lambda = 0.70$.

2.2 Observations and data reduction

2.2.1 Sample selection

We investigate a subsample of the ultraviolet-luminous galaxies (UVLGs). These objects were first defined by Heckman et al. (2005) to have far-ultraviolet (FUV) luminosities $\geq 2 \times 10^{10} L_\odot$, which is roughly halfway between the characteristic luminosity of present-day galaxies and that of higher redshift Lyman break galaxies (LBGs).

As described in the previous section, Hoopes et al. (2007) later expanded the analysis of these objects and subdivided the sample in terms of average FUV surface brightness (I_{1530}), using the SDSS u-band half-light radius as proxy for the UV size of the galaxies. The sample was divided in three categories: large UVLGs ($I_{1530} \leq 10^8 L_\odot$ kpc^{-2}), compact UVLGs ($I_{1530} > 10^8 L_\odot$ kpc^{-2}) and supercompact UVLGs ($I_{1530} > 10^9 L_\odot$ kpc^{-2}). The latter represents the aforementioned LBAs.

The LBAs are compact systems undergoing intense star formation; in fact, they are among the most star-forming galaxies in the low-redshift universe. The observed physical properties, such as metallicity, dust attenuation, UV/optical morphologies and star formation rates, are remarkably similar to those of high-redshift LBGs. We further discuss the analogy between low- and high-redshift objects in subsequent sections.

2.2.2 Observations and data reduction

LBAs are selected to have high surface brightness values, which translate into small physical sizes, ranging from 0.4 to 1.9 kpc half-light radii in the ultraviolet (Overzier et al., 2010). Together with the high star-formation rates up ~ 100 M$_\odot$yr^{-1} (Hoopes

et al., 2007), which translates into extremely bright nebular hydrogen emission lines, LBAs are highly suitable targets for adaptive-optics (AO) assisted integral-field spectrography.

We have used OSIRIS in the Keck II telescope (Larkin et al., 2006). OSIRIS is an integral field unit (IFU) available solely for use with AO. It provides a spectral resolution of $R \sim 3800$ and a field of view (FOV) of a few arcseconds, depending on the configuration utilized. Its design is based on a lenslet array, with variable spatial pixel scales (spaxels) depending on the need for better PSF sampling or a larger FOV. In good weather conditions, we are able to achieve near diffraction limited resolution, or approximately 70 milli-arcseconds (mas) FWHM in angular size.

We have targeted the Pa-α emission line (rest wavelength $\lambda = 1875.1$ nm), which is expected to be ~ 8 times fainter than the H-α line, depending on gas temperature (Osterbrock & Ferland, 2006). In all cases this is redshifted into the redder half of the K-band, with observed wavelength varying between 2055 nm $< \lambda_{\mathrm{obs}} <$ 2350 nm for the objects in our sample.

The objects observed for this work were selected from the original 30 objects observed with HST presented in Overzier et al. (2010). Due to a lack of bright nearby guide stars, we have used the Laser Guide Star Adaptive Optics (LGS-AO) system for all objects presented here (van Dam et al., 2006; Wizinowich et al., 2006). The selection of galaxies for each observing run was based purely on availability during a given night, proximity of prominent sky lines to the wavelength of the Pa-α line at each redshift and lesser impact of Space Command closures (when observers are prevented from using the laser due to possible collisions with artificial satellites). Therefore, no biases were introduced in the data beyond the original LBA selection.

The properties of individual objects are shown in Table 2.2.2 along with observing information. Stellar masses are measured from SED-fitting of SDSS data as available on the SDSS/DR7 catalog. These values are derived from Bruzual & Charlot (2003) models and optical data only; the lack of near-infrared data and TP-AGB stars from the synthesis library should introduce an uncertainty of ~ 0.3 dex (see Overzier et al., 2009), small enough that our results, spanning 2 orders of magnitude in stellar mass,

are unaffected. Star-formation rates presented here are measured from combined Hα and MIPS-24μ data; they typically present an uncertainty up to 0.3 dex (Overzier et al., 2009). For an in-depth discussion of properties of LBAs and comparison with high-z galaxies, see Hoopes et al. (2007) and Overzier et al. (2009, 2010).

Given the limited physical size of the CCD detector, there is a trade-off between spatial coverage and wavelength coverage; since we are interested in a single emission line, we have chosen to use the narrowband mode for most galaxies in order to maximize the spatial coverage of the data. In most cases we observed with the 50 mas spaxel scale; the UV sizes of the remaining objects were larger and we chose to use the 100 mas scale with double the FOV.

In many cases, the object occupies a significant portion of the FOV of the instrument. Because appropriate sky subtraction is crucial for a reliable detection of emission lines in the data, we have ensured an exclusive sky frame was taken in conjunction with each science frame. The best strategy to maximize on-target telescope time was to observe in 45 minute blocks of science-sky-science frames, with 15 minute exposures in each case. Weather ranged from acceptable to excellent in all cases, with uncorrected seeing (in V-band) varying from ~ 1" in moderate conditions to 0.5" in the best cases. Weather conditions directly affect spatial resolution in our data, since the quality of AO corrections depend on the stability and brightness of the laser guide star and the tip-tilt star.

Data were reduced with the OSIRIS pipeline, which subtracts the sky frames and translates the two-dimensional detector image into a 3D datacube, composed of two spatial dimensions and one wavelength dimension (for details, see Wright et al., 2009). In addition, we have written custom IDL code to further subtract sky emission residuals still present in the datacube. This is done for each galaxy simply by fitting the 1D spectrum at spaxels where we believe no signal from the observed galaxy exists; this is then subtracted from all spaxels in the datacube.

Table 2.1: Summary of LBA observations

Name	z	Observing date (UT)	Spaxel scale	Exposure (s)	AO FWHM (mas)	SFR ($M_\odot$ yr^{-1}) Hα + 24μm	R_l (kpc)	log M (M$_\odot$
005527	0.167	Oct 01, 2007	50	900	90	55.4	0.36	9.7
015028	0.147	Oct 20, 2008	50	2400	82	50.7	1.34	10.3
021348	0.219	Oct 19, 2008	100	2100	177	35.1	0.38	10.5
032845	0.142	Jan 24, 2010	50	1800	103	8.7	0.86	9.8
035733	0.204	Oct 20, 2008	100	1800	116	12.7	1.00	10.0
040208	0.139	Sep 13, 2009	50	2100	80	2.5	0.80	9.5
080232	0.267	Jan 24, 2010	100	1800	115	30.4	3.01	10.7
080844	0.096	Feb 06, 2010	100	1200	187	16.1	0.08	9.8
082001	0.218	Jan 25, 2010	50	2400	69	40.0	2.78	9.8
083803	0.143	Feb 05, 2010	50	1800	105	6.2	1.02	9.5
092600	0.181	Feb 26, 2008	50	1800	101	17.0	0.68	9.1
093813	0.107	Feb 06, 2010	50	1800	77	19.8	0.65	9.4
101211	0.246	Feb 06, 2010	50	1200	96	6.2	N/A	9.8
113303	0.241	Jan 24, 2010	50	2400	76	7.7	1.36	9.1
135355	0.199	Feb 05, 2010	50	2100	68	19.4	1.45	9.9
143417	0.180	Feb 26, 2008	50	2700	98	20.0	0.90	10.7
210358	0.137	Oct 20, 2008	50	1500	65	108.3	0.44	10.9
214500	0.204	Sep 13, 2009	50	2400	70	16.4	1.13	9.9
231812	0.252	Sep 13, 2009	100	1800	130	63.1	2.77	10.0

2.2.3   Kinematic maps

In order to produce velocity moment maps, we fit gaussian functions to the emission lines detected at each spaxel. In most cases, our LBA spectra do not show any continuum, only the Pa-α line emission. The zero-point of the fit is the center of a gaussian fit to the integrated one-dimensional spectrum of the collapsed datacube.

We smooth every datacube spatially with a kernel of 1.5–2 pixels, depending on the data quality and seeing in each case. While this results in a slight loss of spatial resolution, it also reduces noise, allowing detection of line emission at regions with lower surface brightness, especially at the outskirts of the galaxies, where gas velocity offsets from the center will likely be higher and thus can strongly affect our kinematic measurements. In addition, to produce the images shown in Fig. 2.1, we oversample the image by a factor of 2, so that features are smoother. This is simply a visualization technique and has not been used in any of the quantitative analyses discussed in the following sections.

The signal-to-noise (S/N) ratios shown are obtained by dividing the area of the gaussian fit to the emission line in each spaxel by the sum of the noise fluctuation over the same wavelength range. The noise is determined from a region of the sky with no emission line detection. We introduce a minimum threshold of $S/N = 6$ for a fit to be deemed acceptable; anything smaller is discarded. This minimizes the presence of artifacts in the final maps. This S/N threshold represents a detection limit in star formation surface density of order $\Sigma_{\rm SFR} \sim 0.1~{\rm M_\odot~yr^{-1}~kpc^{-2}}$, comparable to surface brightness limits determined in Förster Schreiber et al. (2009) and an order of magnitude deeper than the data presented in Law et al. (2009). The velocity-dispersion (σ) maps, corrected for instrumental broadening, always show values greater than the intrinsic instrumental resolution of $\sim 35~{\rm km~s^{-1}}$, with the exception of some low surface brightness spaxels.

Figure 2.1 shows the recovered kinematic maps for each of the objects in our sample. In each case, the two left panels show the HST images of the galaxy, with line emission contours overlaid. The third panel shows the zero-th moment of the

fit, which is simply the total intensity in each spaxel, shown as the signal-to-noise of the fit in each spaxel. The fourth panel shows the velocity maps, and the final panel shows the velocity-dispersion maps. We also show the resolution element, given by the FWHM of a star observed before the galaxy, in the exact same configuration (band filter and pixel scale). Also shown is a horizontal bar indicating a physical size of one kpc at the redshift of the galaxy. Three of these galaxies (092600, 143417 and 210358) have been previously analyzed in Basu-Zych et al. (2009a).

2.2.4   Comparison with HST morphologies

Figure 2.1 shows the HST images for each galaxy in rest-frame optical (left panel) and UV (second-to-left). Images are scaled at logarithmic (black) and linear (blue) stretch, to distinguish between low surface brightness structures and more compact ones. Pa-α flux contours, in red, typically enclose one-third of the rest-frame optical flux, and above 60% of the UV flux. In general we are able to detect emission where the bulk of the stellar mass is present, unless no significant star formation is present (e.g., the southeast components in 080844 and 210358).

Comparison between both bands in HST shows more extended structures in the rest-frame optical, in particular at low surface brightness (black). This might indicate an underlying older stellar population in which star-forming regions exist. A complete discussion of LBA morphologies in both bands can be found in Overzier et al. (2009, 2010).

2.2.5   Comparison with high-redshift galaxies

As briefly discussed in Section 2.1, LBAs have been defined on the basis of UV luminosity and surface brightness thresholds as appropriate for high-redshift Lyman break galaxies. Previous studies have supported the analogy, finding both apparent and physical properties consistent with those of their high-z counterparts. In this section we investigate the parallel in terms of gas kinematics of LBAs compared to LBGs.
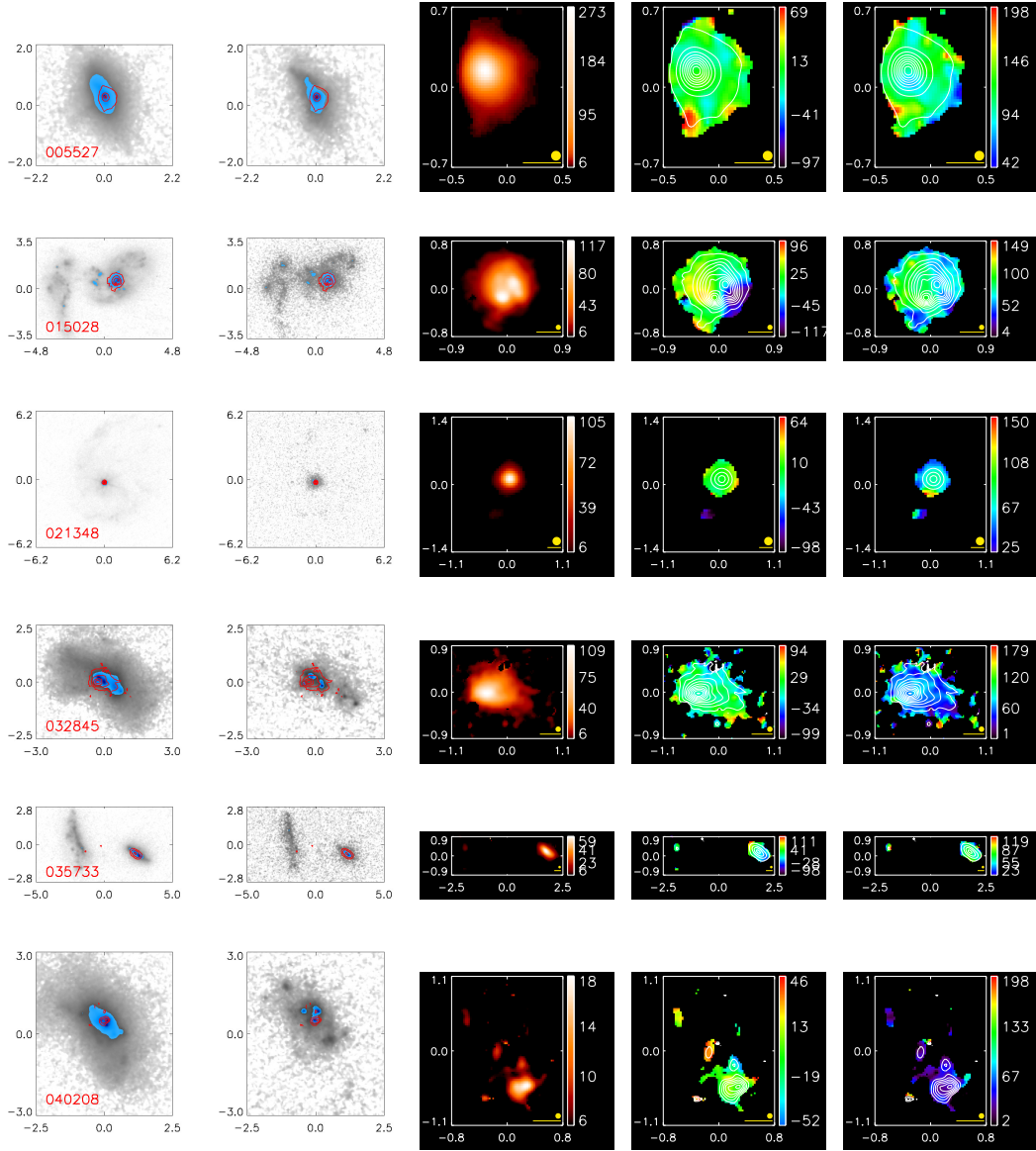
Figure 2.1: We show here the velocity moment maps for all galaxies observed for this work. The two leftmost figures show the HST rest-frame optical (left) and UV (right) morphologies, with logarithmic (black) and linear (blue) stretches. The Pa-α S/N levels are overlaid in red. There is no UV image available for 101211. The following images show, from left to right, the signal-to-noise ratios, line-of-sight velocity in km s^{-1} and line-of-sight velocity dispersion, also in km s^{-1}. For the latter two we overplot S/N contours in white. The axes show the angular scale in arcsec; orientation is the same in every panel, with north pointing up and east to the left. We indicate in each panel the FWHM of a point source as a proxy for spatial resolution and the physical scale corresponding to 1 kpc at the redshift of each galaxy.
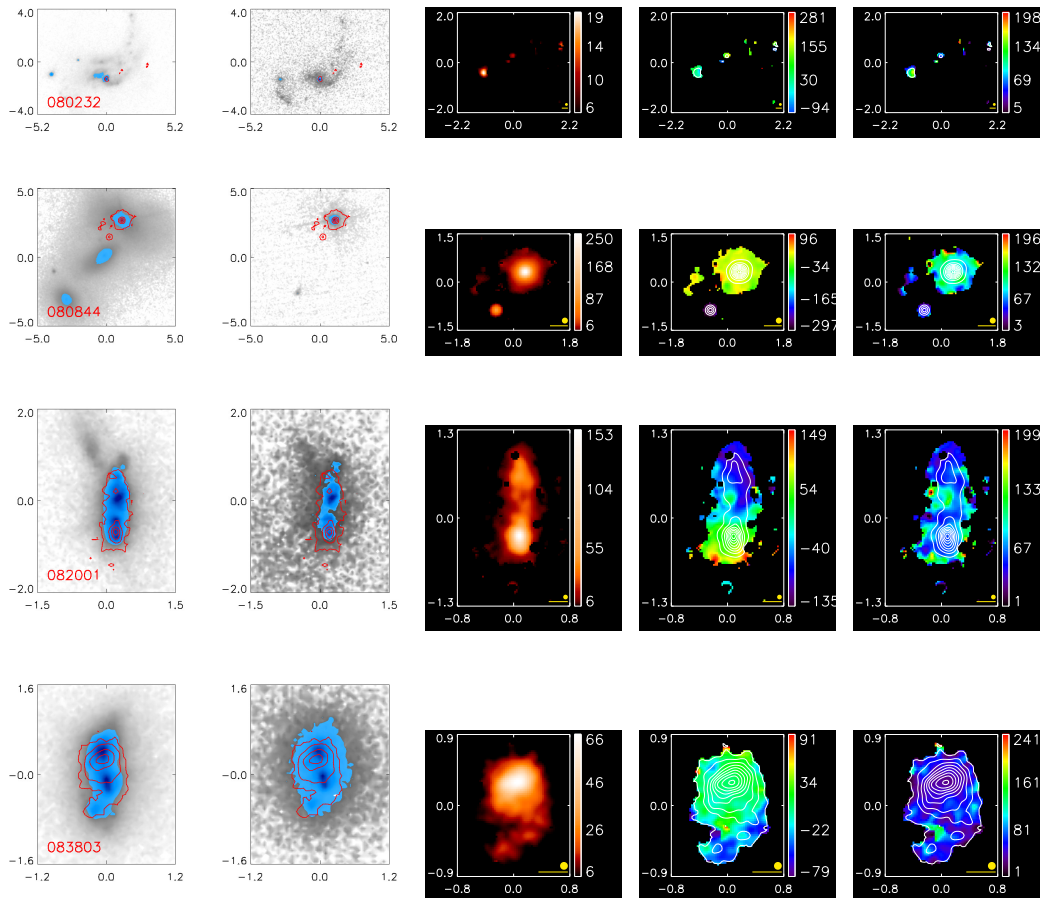
Figure 2.1: Continued.
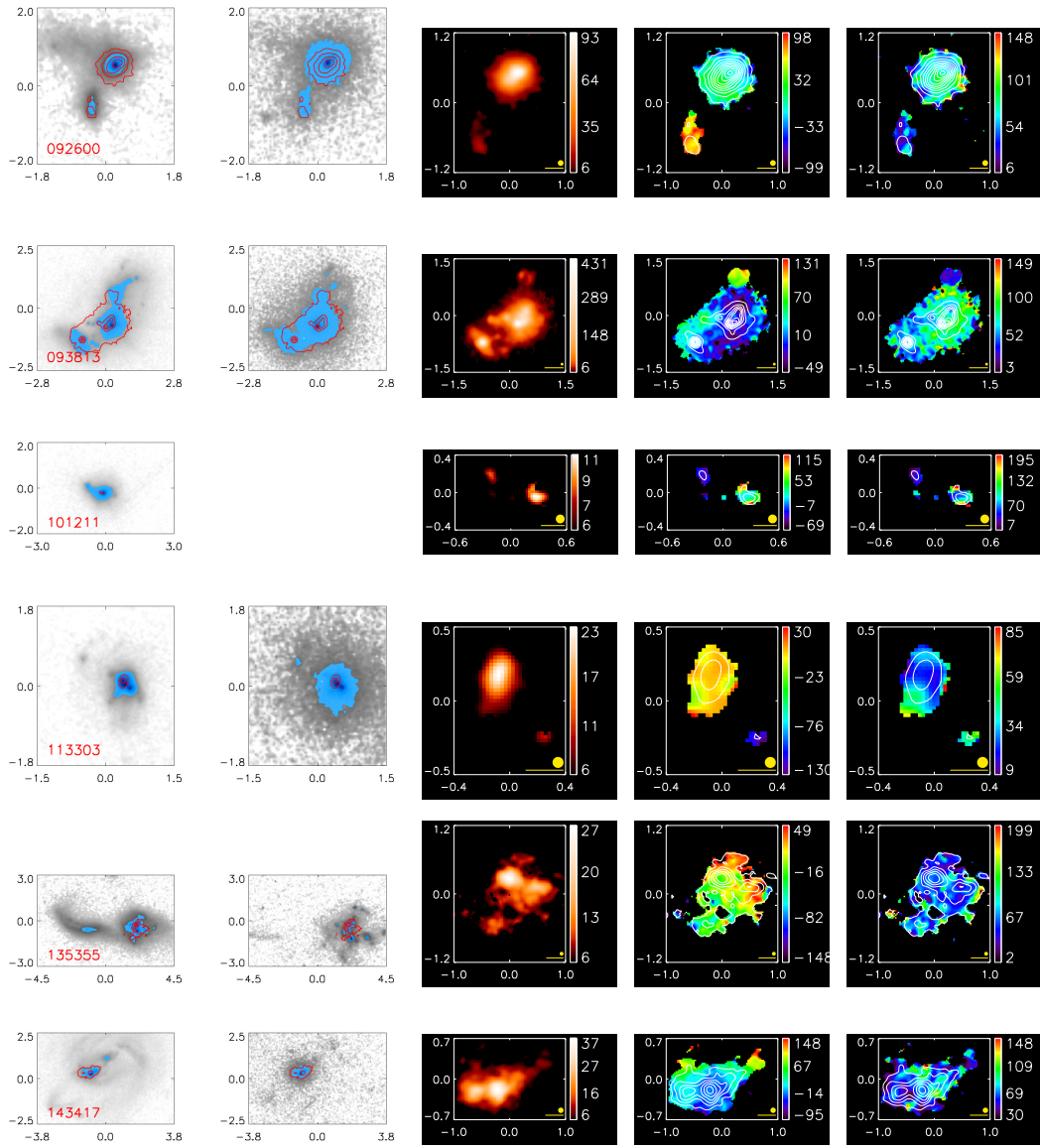
Figure 2.1: Continued.
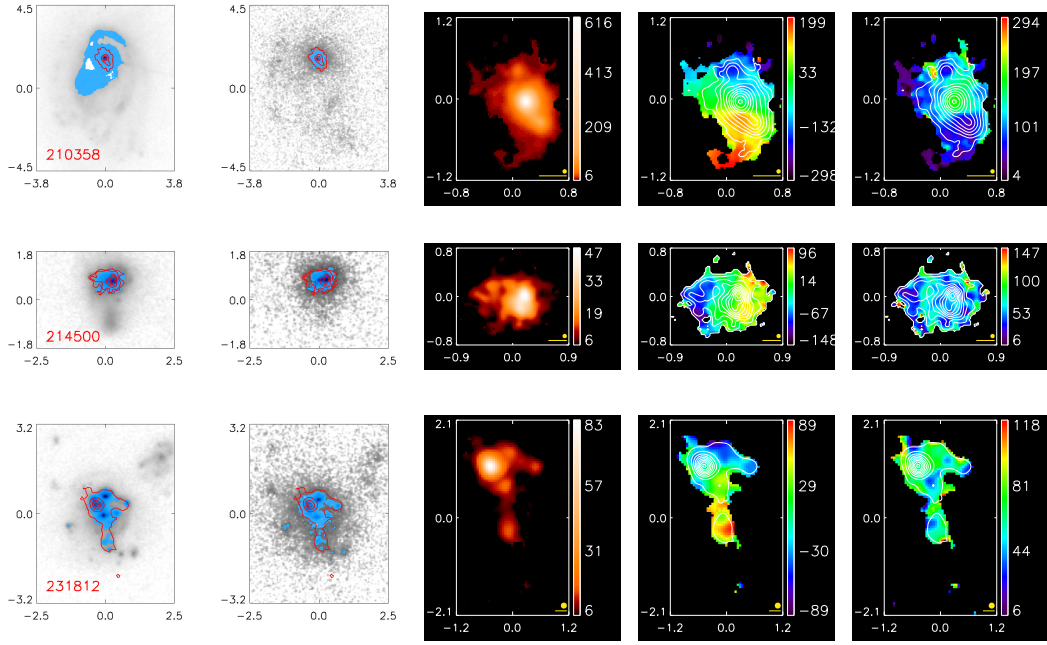
Figure 2.1: Continued.

In order to allow for a direct comparison between kinematics of LBA- and LBG-type systems, we have artificially redshifted all our galaxies to $z \sim 2.2$[2], and reobserved with the simulated IFU prescriptions described by Law et al. (2006). At this redshift, these galaxies would be observed in Hα. We scale our observed Pa-α flux maps to the total Hα fluxes determined by SDSS.

We have also artificially redshifted our data and simulated observations with the SINFONI instrument, in non-AO mode. In this case, the hydrogen line-emission surface brightness detection limits in Förster Schreiber et al. (2009) is comparable to our sample: on one hand the instrument is more sensitive, Hα is brighter and there is no loss due to the adaptive optics system; on the other hand, cosmological surface brightness dimming would make sources up to 200 times fainter per solid angle unit. Therefore, we simply degrade our spatial resolution with a 0.5" gaussian kernel, rebinning our datacubes to the nominal 0.125" pixel scale of SINFONI. Examples for the resulting velocity maps can be seen in Fig. 2.2.

As discussed in Overzier et al. (2010), where the same technique has been used

---

[2]This precise redshift was chosen to avoid major OH emission lines.

for HST images, much detail is not observed due to loss of spatial resolution and/or surface brightness dimming. As in the case of HST observations, the loss in spatial resolution causes different star-forming regions to be confused into one larger clump. This might lead to misinterpreting multiple clumps with velocity differences as one larger, smoother rotating disk, with implications for inferences about its formation mechanism (see Sections 2.4, 2.5). This is particularly true for the simulated SINFONI data, in which case many LBAs are not even spatially resolved.

These simulations will be used below when comparing kinematical measurements of LBAs and actual high-redshift galaxies observed.
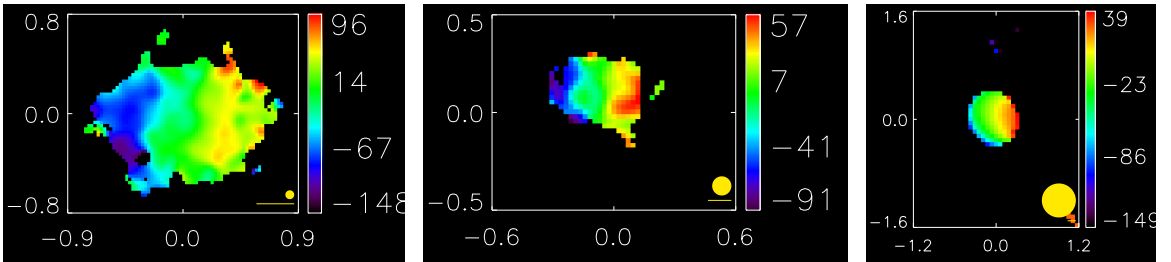
Figure 2.2: Velocity maps of 214500 at its intrinsic redshift (*left*) and artificially redshifted to $z \sim 2.2$, as observed by OSIRIS (*center*) and SINFONI (*right*). Legends are the same as in Figure 2.1. As expected, spatial resolution is lower, and low surface brightness features are harder to distinguish.

2.3   Analysis of Individual Objects

In the following sections we briefly describe each object in more detail. Two of these objects (021348 and 080232) are not resolved even with adaptive optics. They present dominant central objects (DCOs) as discussed in Overzier et al. (2009). A third object (101211) is too faint, and no extended structure is detected. We exclude these three objects from the kinematic analysis in subsequent sections.

2.3.1   005527

This is the only object observed in broadband mode. Velocity dispersion is rather uniform across the whole galaxy, at about 100 km s^{-1}. The optical morphology is

evidently much more extended than the Pa-α emitting region, which might indicate an underlying, more extended, older stellar structure.

2.3.2 015028

This is an object showing two clearly distinct star-forming regions. There is also a clear velocity shear in the east-west direction, which is not aligned with the axis connecting the two bright clumps. Velocity dispersion is higher in the eastern half of the galaxy. In addition, there is some additional emission to the south, at higher velocity than the rest of the galaxy; it is unclear whether this represents a spiral arm or a tidal tail from an ongoing interaction.

2.3.3 021348

This is the faintest object observed, and we have only been able to detect an unresolved point source in the center of the galaxy, in addition to a low S/N region ($S/N < 10$) to the south. It is the first of five objects observed with OSIRIS that were classified as having a DCO, according to Overzier et al. (2009). Since we cannot make any inferences about the resolved kinematic structure of the galaxy, we have excluded it from any further analysis.

2.3.4 032845

032845 is a bright object, and a significant amount of structure is detected. However, velocity shear is remarkably small, and velocity dispersion is, again, relatively homogeneous across the galaxy. The HST optical image shows an antenna-like structure, with distinct nuclei, in what appears to be a merger.

2.3.5 035733

We have been able to detect not only the brightest component, but the faint companion to the east, where line emission is evidently weaker. A comparison with the

HST image shows a much more extended structure than what is seen here. The western region, however, is clearly defined, and shows a definite velocity shear across its major axis, resembling a rotating disk, but still with line-of-sight velocity dispersion values of approximately 70 km s^{-1}, close to the value of the velocity shear across the major axis. The companion to the east is at the same systemic velocity as the main component.

2.3.6   040208

This is one of the faintest galaxies we have observed (SFR= 2.5$M_\odot$ yr^{-1}), therefore the signal-to-noise ratio is considerably smaller. There are a number of star-forming regions northeast of the main component, and the velocity offset between them is rather small.

2.3.7   080232

This is another DCO, like 021348. Again, we detect very little emission besides a bright point source in the center of the galaxy. This object is also excluded from further analysis.

2.3.8   080844

This is another DCO, but in this case we were able to detect emission from the companion to the southeast. There is little velocity structure within the main component, but the companion is offset more than 200 km s^{-1} from the point source.

2.3.9   082001

082001 is one of the most elongated objects in our sample, which leads to the assumption that it might be disk-like structure seen edge-on. The velocity structure seems to confirm this hypothesis, with a strong shear across the major axis. We are able to

detect multiple components, indicating there are distinct star-forming regions within this disk.

2.3.10 083803

This object shows a main emission region larger than a kpc across, with little velocity structure. In addition, we were able to detect emission from a fainter structure to the south, with a velocity offset from the main component of ~ 50 km s^{-1}. This structure is also seen in the HST image.

2.3.11 092600

This is another example of an LBA with a companion structure, also evident in the HST image. The companion presents an ~ 50 km s^{-1} shift with respect to the main structure. Also evident is a velocity shear across the main region itself, albeit small – ~ 50 km s^{-1} – especially when compared to the velocity dispersion of approximately ~ 100 km s^{-1} found in the galaxy. This is the least massive of our objects (log $M_*/M\odot = 9.1$) and has also been described in Basu-Zych et al. (2009a).

2.3.12 093813

This is one of the galaxies with the strongest line emission in our sample (the Pa-α line is detected at $S/N > 400$ in some regions), and therefore we are able to detect the substructure with great amount of detail. Multiple components are observed, with velocity offsets greater than 100 km s^{-1} between them. Showing signs of a recent or ongoing strong merger event in the HST optical data, the velocity dispersion seems higher where the merging galaxies appear to meet, to the west, where Pa-α emission is strongest.

2.3.13 101211

The emission is weak, and little structure is detected beside a faint companion to the northeast. Due to lesser data quality in comparison with other galaxies in our sample, we do not use this object for our subsequent analysis.

2.3.14 113303

This galaxy shows a remarkable lack of velocity structure within the main component, with a shear of a few tens of km s^{-1}, comparable to the instrument resolution itself. However, we were able to detect some faint emission from a component to the southwest, offset from the main region at approximately 100 km s^{-1}.

2.3.15 135355

135355 is composed of a large number of small star-forming regions, each measuring a few hundred pc across. These components show a gradual velocity shear at a 45 degree angle, indicative of a global velocity structure across the entire galaxy. In addition, there is an elongated component to the east, visible only in the optical HST data and which is likely a merging companion.

2.3.16 143417

This object presents two clearly distinct regions of star formation, along the east-west axis. The regions are at distinct velocities with respect to each other. In addition, we detect fainter emitting regions to the north and northwest, at very different velocities from the two brightest regions. These two regions are part of much more elongated structures, as can be seen in the HST image, which shows strong signs of an ongoing interaction. This has also been discussed in Basu-Zych et al. (2009a).

2.3.17 210358

This is the most massive object we have observed, and one with unique features. It is one of the DCO objects as described in Overzier et al. (2009), and we confirm the existence of a bright, unresolved region in the center of the galaxy. This region has high Pa-α surface brightness, with values above 10^{-13} erg s^{-1} cm^{-2} arcsec^{-2}. This galaxy presents the strongest velocity shear across its major axis, $v_{\mathrm{shear}} \sim 250$ km s^{-1}. This is the third object presented in Basu-Zych et al. (2009a).

2.3.18 214500

This galaxy presents high velocity shear across its major axis, uncommonly so for its low stellar mass (see Section 2.4.1). However, its structure is not smooth, and there are undetected stellar components to the south, seen in the HST image. Likewise, the velocity-dispersion map is not as well structured as other disk-like galaxies. This may indicate a recent merger event.

2.3.19 231812

This is one of the largest galaxies in our sample, and therefore was observed with the 100 mas spaxel scale to maximize its field of view. It shows a bright component with fainter structure to the south and west. The star-forming region to the south has a velocity offset of ~ 75 km s^{-1} from the brightest part of the galaxy.

2.4 Results

In this section we discuss some of the analytic results obtained from the data. The velocity dispersion σ measured for the galaxies is an average of each spaxel, weighted by flux. This allows for a more accurate measurement than simply measuring the velocity dispersion of the whole cube, since it does not incorporate the intrinsic velocity shear within the galaxy.

2.4.1 Kinematics and dynamics of star-forming galaxies

The ionized gas in LBAs exhibit very high velocity dispersions, with median ~ 67 km s^{-1} and some galaxies reaching values above 100 km s^{-1}. This is much higher than those observed in ordinary local star-forming galaxies (typical gas velocity dispersions of 5–15 km s^{-1}, e.g., Dib et al. 2006) but analogous to the increased velocity dispersions observed in local (ultra-)luminous infrared galaxies (e.g., Arribas et al., 2008; Monreal-Ibero et al., 2010).

We also measure the velocity shear within each galaxy. Since we cannot always precisely define an axis of rotation, we simply determine the difference between the maximum and minimum velocities observed within the main body of the galaxy (excluding companions in order to probe for intrinsic rotation of one star-forming region). We determine v_{max} and v_{min} as the median of the fifth-percentile at each end of the velocity distribution, so that outliers and artifacts are excluded. The velocity shear is then simply defined as $v_{\mathrm{shear}} = \frac{1}{2}(v_{\mathrm{max}} - v_{\mathrm{min}})$. The values vary between a few tens of km s^{-1} and over 200 km s^{-1}. These measurements are presented in Table 2.2. In many cases, the velocity shear is not caused by actual rotation of the whole galaxy, since there is not a significant velocity gradient observed across the entire object.

There is a strong trend of velocity shear with stellar mass: more massive objects tend to show greater velocity differences between distinct regions of ionized gas. This can be seen in detail in Figure 2.3. Velocity dispersion σ also correlates with stellar mass, albeit with a shallower slope. For comparison, we also show in Figure 2.3 the local Tully-Fisher relation derived in Bell & de Jong (2001), corrected for an average inclination factor of $\langle \sin i \rangle = 0.79$ (see Appendix in Law et al., 2009). Although an inference for such a relation for LBAs is not reasonable, since these objects are not necessarily rotating disks, this serves as a comparison with velocity shear in local spirals. These values are slightly smaller for a given stellar mass, especially at lower masses (up to a factor of 2). Also shown is the derived relation for star-forming galaxies at $z \sim 2.2$ from Cresci et al. (2009), which shows higher v_{circ} values than spirals in the present day; however, in the former, the galaxies studied are more

Table 2.2: Kinematic data for LBAs

Name	$v_{\rm shear}$	σ	v/σ	$v_{\rm shear,hiz}$ (OSIRIS)	$\sigma_{\rm hiz}$ (OSIRIS)	$v_{\rm shear,hiz}$ (SINFONI)	$\sigma_{\rm hiz}$ (SINFONI)	$K_{\rm asym}$	$K_{\rm asym,hiz}$ (OSIRIS)	$K_{\rm asym,hiz}$ (SINFONI)
005527	42	104	0.41	35	89	18	122	0.77	0.46	0.93
015028	78	74	1.05	57	73	31	82	0.21	0.19	0.09
032845	73	68	1.08	13	46	101	78	1.60	0.63	0.59
035733	50	66	0.76	28	47	19	62	0.27	0.26	0.25
040208	53	50	1.06	N/A	N/A	23	35	0.89	N/A	0.44
080844	27	92	0.30	16	95	14	117	2.16	0.46	0.41
082001	119	67	1.78	85	65	67	91	0.17	0.11	0.08
083803	41	49	0.83	28	29	13	45	1.38	0.50	0.53
092600	36	71	0.51	23	54	25	69	0.61	0.94	0.19
093813	63	67	0.94	38	63	30	85	0.55	0.25	1.85
113303	14	30	0.45	30	41	66	66	0.66	0.60	0.09
135355	77	67	1.15	46	51	50	82	0.70	0.43	0.19
143417	73	67	1.09	41	65	37	67	1.19	0.21	0.29
210358	183	136	1.35	72	161	109	210	0.17	0.12	0.16
214500	81	55	1.47	56	58	64	96	0.18	0.20	0.19
231812	70	63	1.11	55	55	47	65	0.28	0.33	0.10

massive ($M_* > 2 - 3 \times 10^{10} M_\odot$), and were pre-selected to look like rotating disks.

Due to the difference in slopes, the ratio between velocity shear and velocity dispersion (v/σ) is also a function of stellar mass (black triangles in Figure 2.4). A Sperman's ρ correlation test shows an $\sim 6\%$ null-hypothesis probability of M_* and v/σ not being correlated. This indicates that more massive LBAs have a stronger component of rotational support against gravitational collapse, as opposed to less massive ones, which are more dispersion dominated.

When artificially redshifted, the v/σ ratio decreases, from a combination of two effects: on one hand, surface brightness dimming causes the high-velocity values at the outskirts of the galaxy to be undetected – this is particularly true for the artificial OSIRIS high-z data (shown as red downward triangles in Figure 2.4). On the other hand, loss of spatial resolution, especially for non-AO observations performed with instruments such as SINFONI (blue downward triangles in Figure 2.4), causes blending of features and inner velocity values to dominate, due to higher signal-to-noise. The net result is lower v_{shear} values. Although our observed v/σ values are higher than high-redshift ones (open circles and squares in Figure 2.4), when artificially redshifted these galaxies look very similar to high-z star-forming galaxies, with 72% chance of being drawn from the same parent population according to a standard Kolmogorov-Smirnov test. We present all relevant values in Table 2.2, along with measurements at their real redshift. We caution the reader, however, to the fact that the observed ratios at low redshift are still much smaller than found in local spiral galaxies, which have v/σ values of 10–20.

The main kinematic difference when comparing LBAs and local spirals comes from gas velocity dispersions, indicating that LBAs have a dynamically thick structure, disk or otherwise. We find it unlikely that the dynamics in all of the LBAs is actually dominated by rotation, given low overall v/σ values. Instead, the trend with stellar mass might simply indicate a colder, less random dynamical structure in the process of forming a disk from the dynamically hot gas in more massive galaxies.
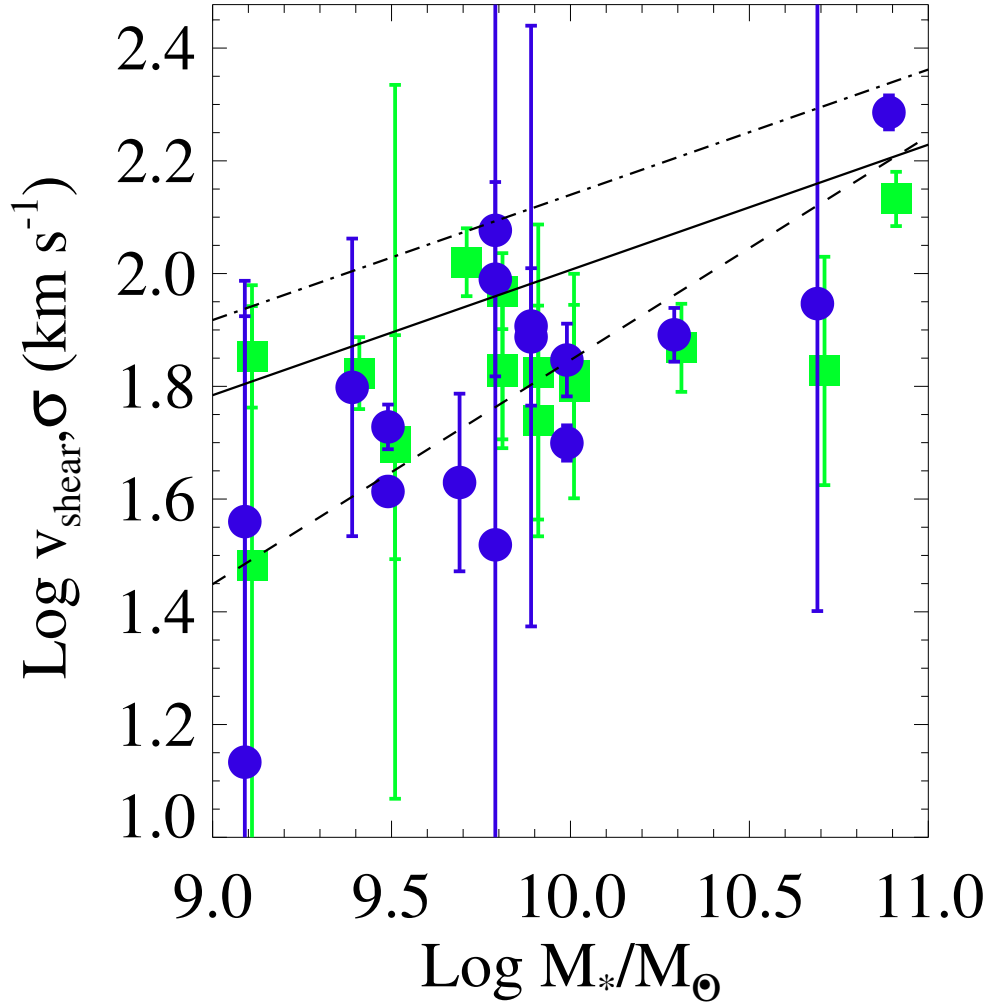
Figure 2.3: Velocity shear v_{shear} (*blue circles*) and velocity dispersion σ (*green squares*) as a function of stellar mass. The plot shows clearly how more massive galaxies show a stronger velocity shear than less massive ones, particularly the ones above $\sim 10^{10}$ $M_{\odot}$. The same trend, albeit weaker, exists for velocity dispersion σ. Dashed line shows a power-law fit to our data, while the solid line is the Tully-Fisher relation at $z \sim 0$ according to Bell & de Jong (2001). The dotted-dashed line shows the Tully-Fisher relation at $z \sim 2$ according to Cresci et al. (2009).
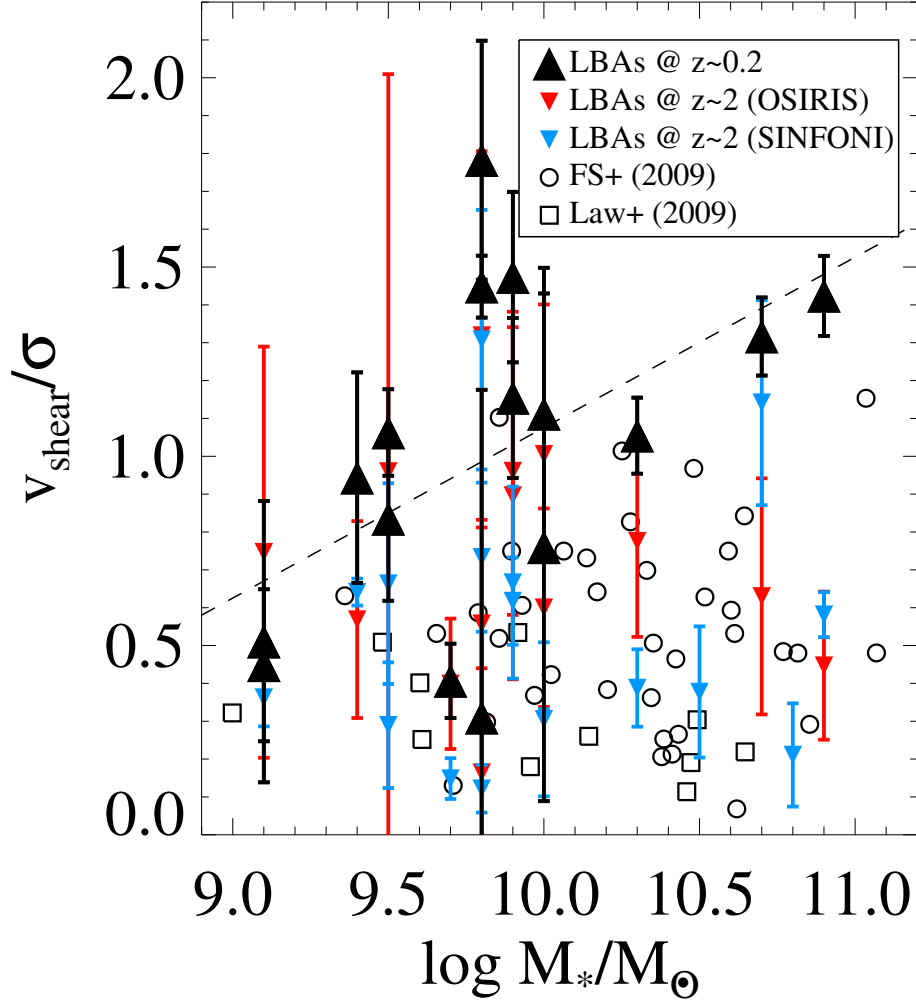
Figure 2.4: Ratios between velocity shear and velocity dispersion v_{shear}/σ as a function of stellar mass (*black triangles*). The dashed line shows a fit to the v_{shear}/σ data at their intrinsic redshift. We see a moderate trend, indicating more massive galaxies have a stronger rotational dynamical component than less massive ones. Also shown as downward triangles are v_{shear}/σ values for galaxies artificially redshifted to $z \sim 2$ (see text in Section 2.2.5). In this case, red triangles represent the OSIRIS simulated data, and blue triangles represent SINFONI non-AO simulations. Values from actual high-redshift observations are presented as hollow symbols, representing data from Förster Schreiber et al. (2009)(open circles) and Law et al. (2009)(open squares).

2.4.2 Kinemetry measurements

Another way of assessing the presence of a rotational component within the dynamics of the gas in each galaxy is provided by the kinemetry method, as introduced by Krajnovic et al. (2006). The method comprises a decomposition of the velocity moment maps into its Fourier components, that is, for a given ellipse:

$$K(\psi) = A_0 + A_1 \sin(\psi) + B_1 \cos(\psi) + A_2 \sin(2\psi) +$$
$$+ B_2 \cos(2\psi) + ..., \tag{2.1}$$

where ψ is the azimuthal angle along which one measures a given velocity moment K (in our case, velocity v or velocity dispersion σ). Written in another way,

$$K(r, \psi) = A_0(r) + \sum_{n=1}^{N} k_n(r) \cos\left[n\left(\psi - \phi_n(r)\right)\right], \tag{2.2}$$

where the expansion terms have been redefined as $k_n = \sqrt{A_n^2 + B_n^2}$ and $\phi_n = \arctan\left(A_n/B_n\right)$. For a detailed discussion of the method, see Krajnovic et al. (2006) and Shapiro et al. (2008).

For an ideal rotating disk, one would expect the velocity profile to be perfectly antisymmetric, that is, the B_1 term would dominate the Fourier expansion. Likewise, the velocity-dispersion map is expected to be perfectly symmetric, and therefore all terms with the exception of A_0 would vanish.

Shapiro et al. (2008) have used this method to analyze the dynamics of high-redshift star-forming galaxies observed with the SINFONI instrument. In quantifying the asymmetry of the velocity moment maps, they have defined the quantities

$$v_{\text{asym}} = \left\langle \frac{k_{\text{avg,v}}}{B_{1,v}} \right\rangle_r \tag{2.3}$$

and

$$\sigma_{\text{asym}} = \left\langle \frac{k_{\text{avg},\sigma}}{B_{1,v}} \right\rangle_r . \tag{2.4}$$

By using local galaxies and numerical models as if observed at high redshift as templates for disk versus merger events, they have found the threshold of

$$K_{\mathrm{asym}} = \sqrt{v_{\mathrm{asym}}^2 + \sigma_{\mathrm{asym}}^2} = 0.5 \tag{2.5}$$

to distinguish between rotating disks and mergers. Galaxies previously identified by eye as rotating disks were correctly classified as disks by the kinemetry method, as were galaxies previously identified as mergers.

We have used the same IDL code as presented in Krajnovic et al. (2006), which at each semi-major axis determines values for inclination and ellipticity of the curve that will minimize asymmetry. The ellipse center was determined as a flux-weighted average of the main body of the galaxy, again excluding companions not connected to the brightest star-forming region. The ellipses defined using the velocity map would then be used with the velocity-dispersion map.

In Figure 2.5 we show average kinemetric asymmetry as a function of stellar mass. As before, we notice a trend in which the most symmetric objects tend to be those with high stellar mass. We use the same threshold of $K_{\mathrm{asym}} = 0.5$ to distinguish between two categories of symmetry. The histogram in the plot shows that more asymmetric galaxies (gray bars) are predominantly less massive, with one single exception; the symmetric galaxies, on the other hand (green hatched bars), are typically more massive, the least massive object having $\log M_*/M\odot = 9.9$. According to a standard Kolmogorov-Smirnov test, there is a 0.7% probability that stellar masses from $K_{\mathrm{asym}} > 0.5$ are drawn from the same parent population as the $K_{\mathrm{asym}} < 0.5$ ones.

Evidently, the threshold of $K_{\mathrm{asym}} = 0.5$ is a simplification; in fact, an inspection of Figure 7 in Shapiro et al. (2008) shows an overlap of disks and mergers in the region where $0.1 < K_{\mathrm{asym}} < 1.0$, which might indicate instead a transition region between disk galaxies and mergers in the kinemetry plot. This region is where most star-forming galaxies at high-redshift lie, as is the case for the LBAs.

Finally we compare our results with the high redshift simulations from Section 2.2.5. In Figure 2.6, we show the measurements based on the simulations and compare
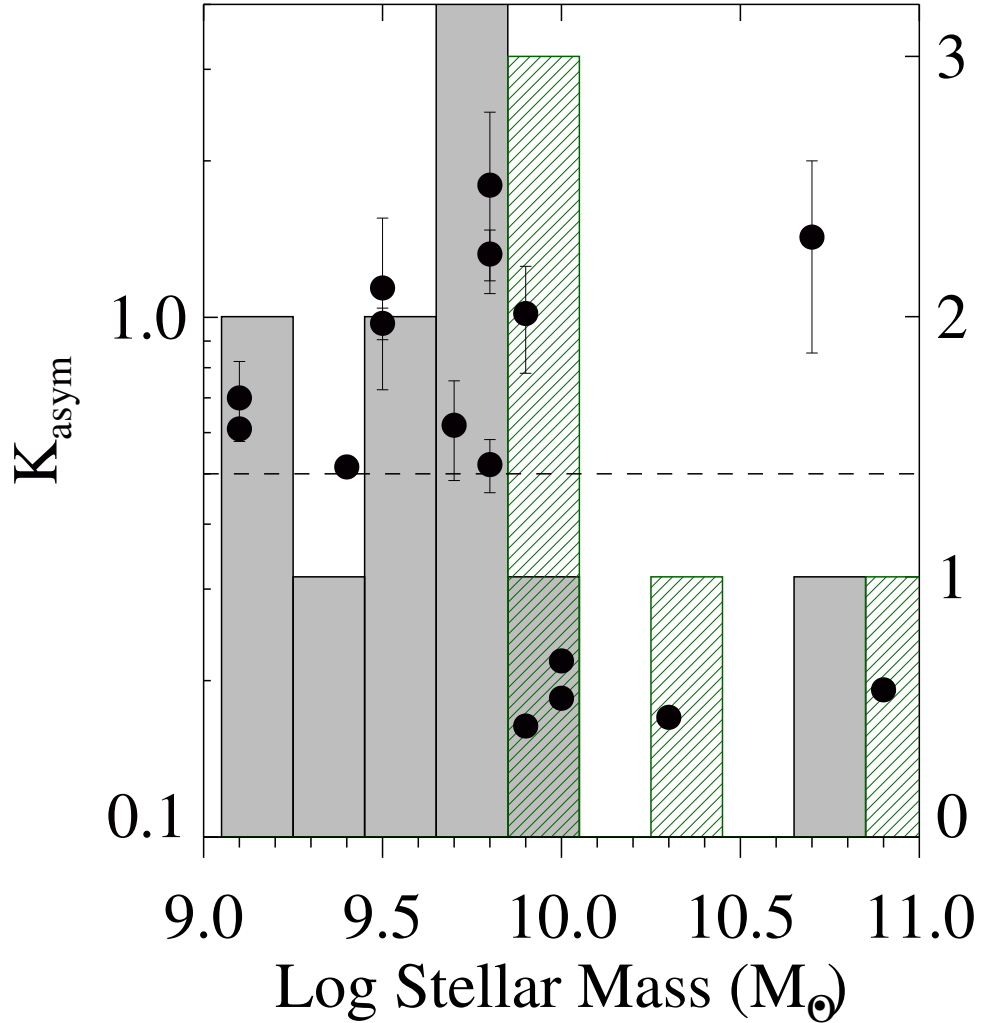
Figure 2.5: Kinemetric asymmetry measurements as a function of galactic stellar mass. Left y-axis shows values of K_{asym}, while right y-axis shows quantities for histograms. Gray histogram shows number of galaxies that would be classified as mergers in Shapiro et al. (2008), while the green hatched histogram shows the number of galaxies that would be classified as disks. Galaxies with high K_{asym} are predominantly less massive, but the lowest value of stellar mass for a galaxy with $K_{asym} < 0.5$ is 9.9.

them to the "intrinsic" values measured in the original (i.e., low-redshift) data. The dashed lines show the same threshold of $K_{\mathrm{asym}} = 0.5$ used to distinguish between disks and mergers. In general, galaxies at high redshift present smaller values of K_{asym}, i.e., they appear more symmetric than they actually are. One-third of the galaxies would be classified differently at high redshift (lower-right quadrant). The net effect is that the percentage of galaxies classified as mergers drop from $\sim 70\%$ to $\sim 38\%$. This is a combined effect of signal loss at higher radii (where kinematics are less symmetric) and confusion and blending, smoothing out features that would otherwise show departures from a rotating disk.

2.5   Discussion

In this section we briefly discuss some of the current models for galaxy formation, and how they relate to both low-redshift LBAs and the high-redshift IFU observations of LBGs. In addition, we discuss some of the implications of the stellar mass dependence of observables discussed in the previous section.

2.5.1   Ionized gas kinematics as a diagnostic for galaxy formation mechanisms

In light of new techniques and integral-field instruments, recent studies of the kinematics of ionized gas at high redshifts have been used as diagnostics for galaxy-formation models attempting to explain the distinctive properties observed in star-forming galaxies at $z \sim 2$–3. In particular, the existence of a large number of rotating gas disks with high velocity dispersions at these redshifts has been pointed out to support the hypothesis of cold gas flows from the IGM directly feeding vigorous star formation at the center of sufficiently massive dark matter haloes (Dekel & Birnboim, 2006; Dekel et al., 2009; Kereš et al., 2009). The high densities generated would then be Toomre unstable, leading to subsequent fragmentation into multiple regions and the observed clumpiness of star-forming galaxies and, in particular, the clump-cluster
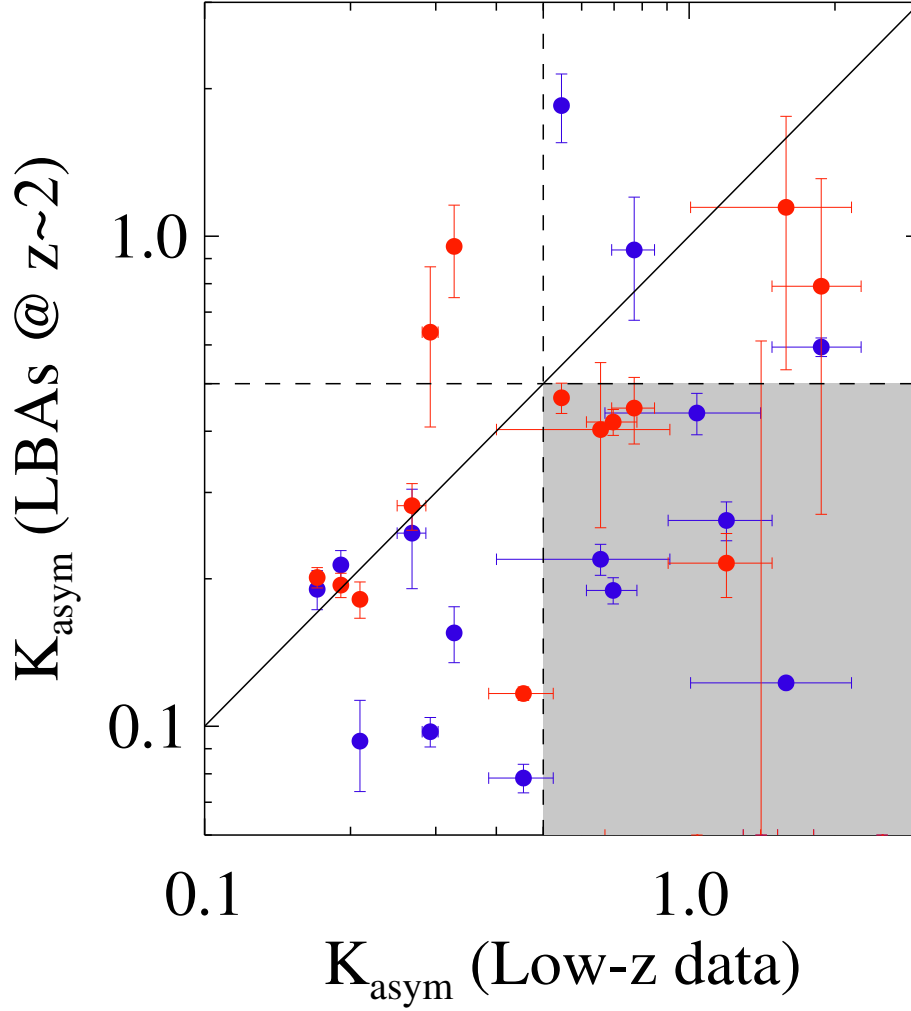
Figure 2.6: Kinemetry measurements for our high-redshift simulations as a function of "intrinsic" values measured at low redshift. Dashed lines show the same threshold of $K_{\mathrm{asym}} = 0.5$. Red points represent OSIRIS-AO simulations, while blue points represent the SINFONI non-AO simulations. The gray shaded area indicates the region of the plot where one finds LBAs having high-asymmetry values at low redshift but low values at $z \sim 2.2$ (lower-right quadrant). In the classification scheme of Shapiro et al. (2008) these objects would likely be classified as rotationally-supported "disks."

galaxies at such redshifts (Immeli et al., 2004; Elmegreen & Elmegreen, 2005; Bournaud et al., 2008). These galaxies are ultimately expected to coalesce, with individual clumps migrating inwards and creating a bulge at the center of the galaxy (Noguchi, 1999; Immeli et al., 2004; Elmegreen et al., 2008, 2009; Genzel et al., 2008).

It should be noted that the emission lines are produced by ionized gas close to star-forming regions, and might therefore not be ideal tracers for the dynamics of the galaxy as a whole. In fact, comparison between our HST rest-frame optical and Pa-α images show we are tracing regions that contain approximately a third of the total stellar mass in the galaxy. Furthermore, the gas in these regions is subject to a number of local feedback effects from stellar winds and turbulence, and thus may not always represent motion of the bulk of the dynamical mass within. Lehnert et al. (2009) argue that the high velocity-dispersion values could not be sustained simply by cosmological gas accretion; instead, self-gravity drives the early stages of galaxy evolution until dense clumps collapse, at which point star formation is self-regulated by mechanical output of massive stars. LBAs seem to support this idea; in Figure 2.7 we show v_{shear} and σ as a function of star-formation rates. Since all variables correlate with stellar mass, we present the residuals of a power-law fit for all of them with respect to M_*, in order to exclude any induced correlations. v_{shear} is independent of star-formation rates (52% null-hyphotesis probability according to Spearman's ρ test), but more star-forming galaxies show stronger velocity dispersion (2% null-hypothesis probability), supporting the idea that star formation drives high σ values. This means the high velocity dispersions observed might simply be a consequence of high densities of gas and star formation driving turbulence and generating high velocity dispersion within the nebular gas.

Another relevant point in this discussion is that rotating kinematics do not exclude the possibility of a merger-triggered starburst. In a hydrodynamical simulation of a gas-rich major merger, Robertson et al. (2006) show that for wet mergers rotating disks may form ~ 100 Myr after the final coalescence. At this point, a large, rotating gaseous disk is formed, with kinemetric asymmetry indices that would in principle rule out the merger scenario (Robertson & Bullock, 2008). The signature for interactions
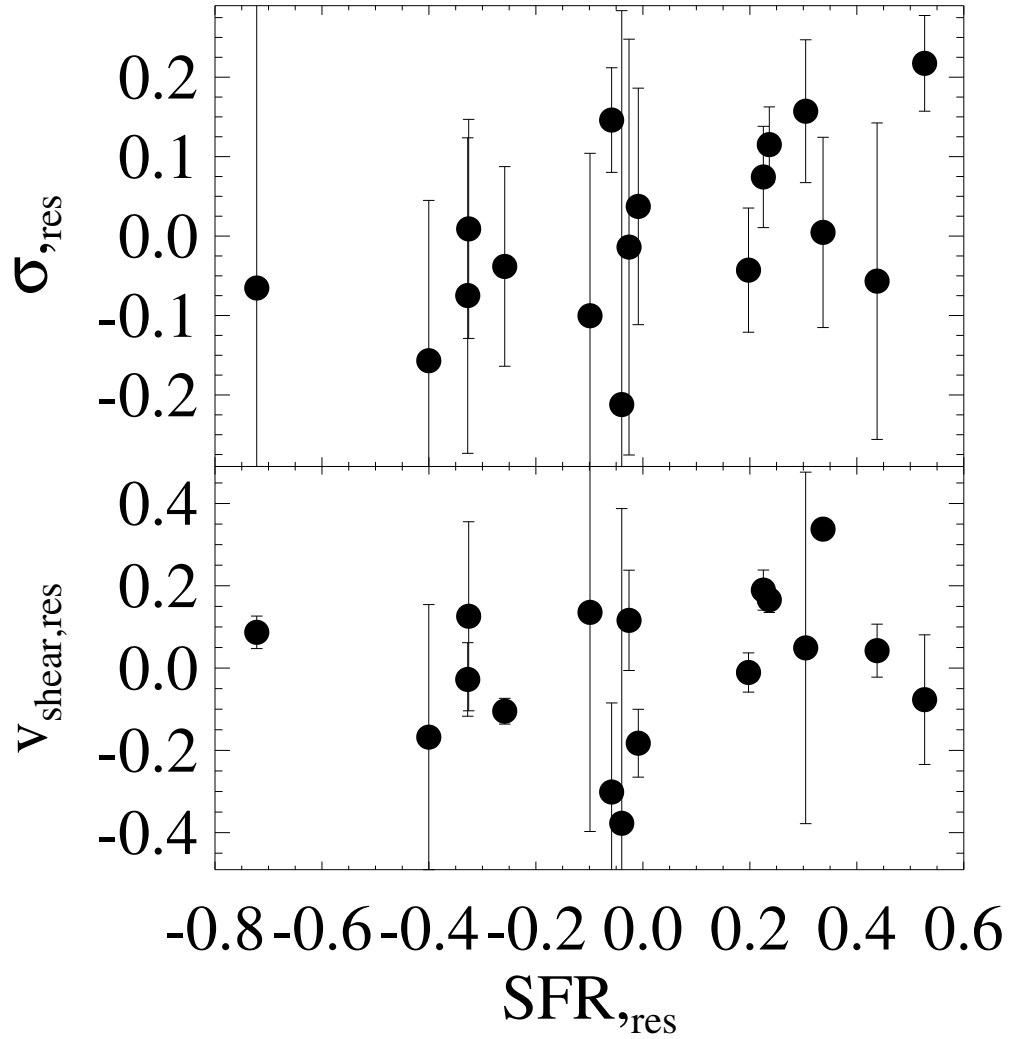
Figure 2.7: Velocity shear and velocity dispersion as a function of star-formation rates. Values are the residuals from a fit with respect to stellar mass (*see text*).

might be as subtle as small displacements of the σ map peak from the center of the galaxy (Flores et al., 2006). Puech (2010) have used similar arguments through IFU studies of clumpy, intermediate redshift ($z \sim 0.6$) galaxies to claim that interactions might be responsible for driving star formation at all redshifts. In these cases, high gas fractions are a fundamental ingredient in the formation of the disk. Indeed, a number of recent CO observations indicate that star-forming galaxies at high redshifts have a much larger gas fraction than standard spirals in the local universe (Tacconi et al., 2010; Daddi et al., 2010a).

It is revealing to compare kinematics of some LBAs in our sample with their optical morphologies as observed with HST (Overzier et al., 2009, 2010). In Figure 2.8 we reproduce the velocity map of 210358 and 135355 and compare them with their optical image. Although they appear as rotating disks in Pa-α, their optical morphologies indicate recent major merger events, with quantitative classification supporting that view. The effect is even more dramatic at higher redshifts (Figures 2.2, 2.8).

Also, on larger scales LBAs seem to support the idea of mergers as triggers for the high star-formation rates observed in these galaxies, as these galaxies tend to pair with other galaxies more strongly than a random sample does (Basu-Zych et al., 2009b). Similar studies at high redshift conclude that the pair fraction is not high enough to account for all observed starbursts (Conroy et al., 2008; Genel et al., 2008), but direct morphological studies of these galaxies indicate the merger fraction is high, up to 50%, with $M_* > 10^{10} M_\odot$ galaxies undergoing $\sim$ four major mergers at $z > 1$ (Conselice et al., 2003; Conselice, 2006). Furthermore, Lotz et al. (2008) argue that the merger fraction might be even higher, since starbursts may outlast morphological asymmetries. On the other hand, the aforementioned morphological studies are all based on rest-frame UV images; these may differ dramatically from the rest-frame optical morphologies, which better trace the mass distribution of the stellar population – the LBAs themselves presenting such contrast (Overzier et al., 2010). Whether or not the same mechanism is triggering star formation at either redshift is still unknown. We do not discard the possibility of an increasing fraction

of galaxies at low redshift being created by major merger events, and that mergers of varying mass ratios may be taking place at either epoch.
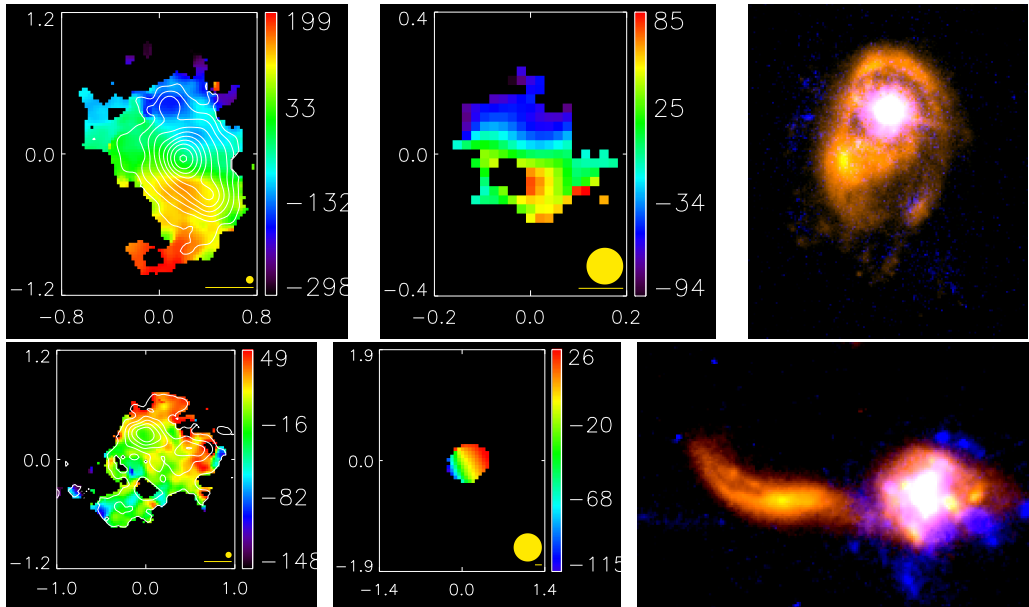
Figure 2.8: Velocity maps at low (left) and high (center) redshifts for 210358 and 135355. On the right we show the optical morphologies of each object as seen by HST, combining optical(orange) and ultraviolet(blue) data. High-z simulated map for 210358 is for OSIRIS data, while for 135355 this is the simulated SINFONI data. In the top case we see a galaxy for which a disk is apparent even at low redshift, while in the second case we notice the effect of loss of spatial resolution. Both these galaxies are classified as mergers through quantitative morphological analysis of the optical images.

2.5.2 The dependence of rotational properties on stellar mass

It has been shown that stellar mass in star-forming galaxies at high redshift correlates with a number of physical properties, such as metallicity, star-formation rates and age (Erb et al., 2006b,a; Magdis et al., 2010). Some results from kinematic studies of the H-α emission at high redshift also indicate this dependence, with more massive objects being more extended and presenting higher v/σ ratios (Law et al., 2009; Förster Schreiber et al., 2009).

In this work, we have shown that massive galaxies are more likely to present disk-like features, as evidenced by higher v/σ ratios and higher levels of symmetric

kinematics, while gas kinematics in less massive objects is dominated by random motions. This distinction is particularly important when taking into account the stellar mass function of LBGs at $z \sim 2$–3. Reddy & Steidel (2009) have found that the stellar mass function is particularly steep at these redshifts, which means an elevated contribution from less massive galaxies. That in turn would suggest more random dynamics for the majority of star-forming galaxies in the early universe, which are responsible for a significant fraction of the stars observed today – $\sim 45\%$ of the present-day stellar mass has formed in galaxies with $L_{bol} < 10^{12} L_{\odot}$ (Reddy & Steidel, 2009).

The dependence on mass is predicted even in more traditional star-formation models. From a large N-body/gasdynamical simulation, Sales et al. (2009) have shown that the angular momentum in a $z \sim 2$ galaxy depends on halo mass. This dependence extends to stellar mass in the galaxy, albeit with varying amounts of scatter according to feedback efficiency (L. Sales, private communication). Whether that can be also a result of wet mergers remains unknown.

It should be noted that the stellar mass presented is the global value for the whole galaxy, while Pa-α traces a region containing a fraction of the stellar mass. It would be interesting to determine whether these relations still hold for the stellar mass contained within that small region, but for accurate measurements we need high-resolution near-infrared imaging, in order to trace stellar mass distribution at sub-kpc scales. Alternatively, longer exposures or more sensitive instruments capable of tracing stellar dynamics instead of nebular gas could probe the kinematic properties at low surface brightness regions. Evidently, this is more difficult at high redshift, where cosmological dimming decreases surface brightness values by a factor of up to 200.

It is also unclear whether the trend with stellar mass represents an evolutionary effect or simply distinct formation scenarios. It is tempting to assume these galaxies keep forming stars for a period of time, increasing stellar mass while at the same time settling onto a rotating disk. However, this would mean that LBAs would necessarily keep elevated star-formation rates for a period over 1 Gyr. Dynamical times of objects

containing multiple star-forming regions, however, are too short (on the order of few tens of Myr), and the galaxy would coalesce much more rapidly. Therefore, a continuous inflow of gas or a sequence of minor mergers feeding star formation in these galaxies would be necessary to keep the observed star-formation rates. Alternatively, it is possible that more massive galaxies have experienced more violent star-formation episodes in the past, after which the dynamical structure has cooled down. An in-depth comparison with hydrodynamical simulations, with careful examination of star-formation histories in LBAs, is required to examine each hypothesis in detail.

2.6   Summary and conclusions

We have performed adaptive-optics assisted observations of 20 Lyman break analogs (LBAs) with the OSIRIS spectrograph at the Keck telescope. By studying spatially resolved Pa-α emission in these objects, we are able to draw the following conclusions:

(1) All galaxies show high velocity dispersions, indicating gas dynamics with a strong random component. Most galaxies show velocity shears of the same order of magnitude as velocity dispersions along the line of sight. This is consistent with our general picture of LBAs as dynamically young, starburst-dominated galaxies frequently undergoing mergers as shown by our HST data;

(2) The kinematics in LBAs are remarkably similar to high-redshift LBGs, which have also been the target of other IFU studies. This is demonstrated by artificially redshifting the LBA sample to $z \sim 2$ and comparing simulated observations of these galaxies to observations of real $z \sim 2$ LBGs that have been presented by other groups (see also Basu-Zych et al., 2009a). All quantitative indicators of gas kinematics agree with those found for LBGs (e.g., Figure 2.4). This indicates that our identification of LBAs as being good local analogs of LBGs based on other, previously determined properties (e.g., SFR, mass, dust, size, metallicity and morphology) can be extended to include their gas dynamical properties as well;

(3) As opposed to IFU observations of high-redshift star-forming galaxies, the proximity of LBAs allows for a more detailed picture of galactic dynamics. In par-

ticular, we have high physical resolution and are less subject to surface brightness dimming. We show this bias at high redshift can lead to erroneous classification of star-forming galaxies, with the kinematic profile appearing smoother and more symmetric (e.g., Figure 2.5);

(4) Even in cases where the LBAs resemble a disk at low redshift, we cannot rule out mergers as the starburst trigger based solely on the gas kinematics. Some disk-like galaxies show clear signs of recent interaction in the optical imaging data (Figure 2.8), and the gas disk might simply be a result of rapid coalescing of a gas-rich merger. Alternatively, a starburst was triggered by a recent infall event, while the underlying disk formed previously in a more gradual fashion;

(5) We have shown that whether a galaxy resembles a rotating disk depends strongly on stellar mass. The relationships between stellar mass and disk-like properties such as observed velocity shear and the light profile support this conclusion. This has strong implications regarding the prevalence of disks at high redshift, and might indicate many of the stars in the local universe have not formed in disk-like galaxies.

Future prospects to study gas assembly in extreme starbursts at low and high redshift are excellent. As illustrated by our work on LBAs, a joint analysis of both morphologies and gas kinematics at high resolution and sensitivity is absolutely essential for deriving an unambiguous picture of the dynamical state of these systems. An important step toward achieving this goal at high redshift will be provided by the combination of the existing Hα kinematical data with accurate rest-frame optical morphologies that can now be measured with the IR channel on Wide Field Channel 3 aboard HST. Furthermore, ALMA will come online soon, and that will allow detection of molecular gas in a large number of star-forming galaxies at redshifts $z \sim 2$–3, which should shed more light on the issue of gas-rich mergers. At low redshifts, ALMA will allow high-resolution measurements of molecular gas distribution and kinematics, providing deeper understanding of the conversion of gas into stars. Finally, the upcoming 20- and 30-m class telescopes, which should be operational at the end of the decade, will allow IFU studies of LBGs with higher sensitivity and

resolution levels comparable to what is available now to LBAs, while the latter will be resolved at scales of giant molecular clouds, and we will be able to study the physical processes of star formation *in situ.* In all cases, the LBA sample offers a unique low redshift dataset useful for contrasting and comparing with starbursts at high redshift.

Chapter 3

Molecular gas in LBAs

3.1   Introduction

In the previous chapter we discussed our work on the detailed study of kinematics of the ionized gas in Lyman break analogs (LBAs). However, this represents a tiny fraction of the total mass, and the observed velocity fields might not represent the dynamic structure of the whole galaxy. In this chapter, we investigate the cold gas, abundant in star-forming galaxies and an additional clue regarding the starburst mechanism in each case.

Molecular gas is one of the most fundamental ingredients in the formation of stars in galaxies. Stars form from the collapse of cold hydrogen gas; therefore H_2 can be seen as the fuel reservoir for star formation in a system. Nevertheless, although it is so abundant in star-forming galaxies – sometimes being the dominant component of the baryonic mass (Erb et al., 2006b; Tacconi et al., 2010; Gonçalves et al., 2011) – we cannot directly observe it. Since it has no permanent dipole, no rotational millimeter lines are observable, and the direct detection of H_2 is very difficult (with the exception of very hot gas outside photodissociation regions; see Zakamska, 2010). Therefore, we rely on emission from rotational transitions in carbon monoxide (CO, the most abundant dipolar molecule in molecular clouds) to study the total molecular gas reservoir. In order to determine the molecular gas masses, we then assume that

$$M(H_2) = \alpha_{CO} L'_{CO}, \tag{3.1}$$

where gas masses are measured in $M_\odot$ and CO luminosities L'_{CO} are measured in K km s^{-1} pc^2. From dynamical mass measurements, the α_{CO} factor has been determined to be 4.6 in the Milky Way (Solomon & Barrett, 1991). However, using the same factor for ultra-luminous infrared galaxies (ULIRGs) yields gas masses larger than dynamical masses (Downes & Solomon, 1998). Therefore, a value of $\alpha_{CO} = 0.9$ is used in these cases.

The case is even more uncertain for lower metallicity galaxies. Leroy et al. (2011) have found that, in the local group, low metallicity objects such as the Small Magellanic Cloud (SMC) show α_{CO} values as high as 70 – at this level, CO is no longer self-shielded from ionizing radiation in the galaxy, while hydrogen is still present in molecular form; therefore CO emission is much fainter for the same amount of gas (Wolfire et al., 2010).

Even with all aforementioned caveats, CO observations have been a key instrument to our understanding of the molecular gas distribution of our local universe. It was established early on that a correlation exists between star formation and gas density in the Milky Way (Schmidt, 1959). Later work by Kennicutt (1998) based on a combination of CO, HI and far-infrared observations determined that the correlation extends to gas and star-formation surface brightness for star-forming galaxies, given by

$$\Sigma_{SFR} = A\Sigma_{gas}^N. \qquad (3.2)$$

This relation is known as the Schmidt-Kennicutt law, with $A = 2.5 \times 10^{-4}$ and $N = 1.4$ empirically determined by Kennicutt (1998) and Daddi et al. (2004), for Σ_{gas} in units of $M_\odot$ pc^{-2} and Σ_{SFR} in units of $M_\odot$ yr^{-1} kpc^{-2}.

More recently, Bigiel et al. (2008) analyzed data from nearby galaxies to resolve the Schimidt-Kennicutt relation down to scales of 750 pc. The authors found that the relation in the nearby universe can be divided into two: one for atomic gas alone, which saturates at approximately 10 M$_\odot$ pc^{-2}; and a linear relation ($N = 1$) for molecular gas, mostly above that saturation level. The linearity has an interesting

consequence: since the Schmidt-Kennicutt law relates star-formation rates and the gas reservoir, an $N = 1$ index means a constant gas depletion timescale for the observed spirals, $t_\mathrm{depletion} = \Sigma_{H_2}/\Sigma_\mathrm{SFR}$. This value was measured to be approximately 2×10^9 Gyr (Bigiel et al., 2008).

In an attempt to offer a theoretical scenario for the formation of stars in giant molecular clouds, Krumholz et al. (2009) proposed a simple model listing three main factors that determined the gas depletion timescales: gas fractions, internal star-formation feedback and turbulence. At first the fraction of gas available for star formation is dependent on self-shielding from the interstellar radiation field – it is this factor that sets the threshold of conversion from atomic to molecular hydrogen. Once molecular clouds are formed, feedback determines their properties, since the internal pressure is higher at this stage than the average ISM pressure. Ongoing star formation in these objects is regulated by turbulence to a universal rate of 1% of the mass per free-fall time. These can be combined into an analytic formalism capable of predicting the linear correlation between gas surface densities and constant depletion timescales.

Understanding the detailed process through which molecular gas translates into stars becomes even more complicated for extreme objects, as has been shown for ultra-luminous infrared galaxies (ULIRGs; $L_\mathrm{bol} > 10^{12}\ L_\odot$; Sanders & Mirabel, 1996) both at low and high-redhifts. As previously discussed in Section 1.3, the observed gas densities in these galaxies is well above the limit of $\sim 100\ \mathrm{M_\odot\ pc^{-2}}$ mentioned in the work of Krumholz et al. (2009), which means the assumption of the properties in giant molecular clouds being determined by internal dynamics is no longer valid, and the end result is likely a distinct scenario for conversion of gas into stars.

In an effort to understand the conversion of gas into stars in these environments, Bouché et al. (2007) and Tacconi et al. (2008) have measured the surface density of molecular gas in submillimeter-selected high-redshift ULIRGs, and have determined that the exponent in the Schmidt-Kennicutt law seems to be higher for these objects, i.e., the star-formation surface density is higher than expected for a given value of gas surface density. The same is true for intermediate redshift ULIRGs: Combes et al.

(2010) have measured CO luminosities of 30 galaxies between $0.2 < z < 0.6$ and have found star-formation efficiencies 3 times higher than those found in the local universe.

Daddi et al. (2010a) have done the same exercise for a number of star-forming galaxies at $z \sim 2$ selected in the optical and near-infrared (the BzK sample), which present more regular structures, with signs of a rotating gas disk. Although these galaxies present higher SFR and gas densities than spirals in the local universe, they appear to follow the same gas-star-formation relation as their low-redshift counterparts. In a later paper, Daddi et al. (2010b) have shown the existence of a "bimodal" Schmidt-Kennicutt law, with distinct normalizations for disk galaxies and dusty, ultraluminous starbursts. Interestingly, this bimodality ceases to exist once the dynamical times in such galaxies is taken into account, i.e., the universal Schmidt-Kennicutt law can be written as

$$\Sigma_{SFR} = \alpha \left(\frac{\Sigma_{gas}}{t_{dyn}} \right)^{\nu}. \tag{3.3}$$

Nevertheless, these studies are still biased towards more massive galaxies, simply because smaller objects are faint and difficult to observe. To date, only two Lyman break galaxies (LBGs) have been observed, both of which are strongly lensed and therefore highly magnified (Baker et al., 2004; Coppin et al., 2007). In order to understand how the star-formation process operates on all scales, it is important to study starburst galaxies at all masses.

So far, we have discussed only observations of the total CO emission for each galaxy, but there is also the possibility of resolving the emission and determining gas dynamics. This is more difficult, since the flux per beam will be reduced by a factor proportional to the decrease in beam size, but is feasible for local galaxies (Bigiel et al., 2008; Leroy et al., 2008). At larger distances this becomes much more difficult, due to loss of angular resolution and cosmic dimming. Still, in the past decade high-resolution observations of the molecular gas have also provided key insights to the dynamical structure of galaxies out to high redshift (e.g., Tacconi et al., 2008). These observations were challenging and required tens of hours of integration time

per object. Over the course of the next year the field will evolve dramatically, with the now online Atacama Large Millimeter Array (ALMA).

Once again, all difficulties presented above are minimized for starburst galaxies observed at low redshift, and our Lyman break analog sample. If we can show that LBAs present the same molecular gas properties as high-redshift LBGs, we can then examine the interplay between gas and star formation at high surface densities more easily than currently achievable at earlier epochs. Plus, with lower limits for the detection of molecular gas, LBAs may shed some light on the critical mass range that current instrument sensitivities have been unable to probe.

In this work, we present results from a molecular gas survey of six LBAs with the CARMA interferometer. We target the lowest CO transition, CO(1-0), to most accurately trace the cold molecular gas in these galaxies. This chapter is divided as follows: in Section 3.2, we present details on sample selection, observations and data reduction; in Section 3.3, we present the results from our survey; and in Section 3.4 we discuss our results, with caveats and future perspectives on our work, including a proposed project for the ALMA interferometer. We summarize our results in Section 3.5.

3.2 Observations and data reduction

3.2.1 Sample selection

Our sample was drawn from the same parent sample as that studied in Chapter 2. In an effort to optimize the CO detection of our pilot program, we further constrained our sample to LBAs with estimated total fluxes above $S_{\rm CO} > 1.0$ Jy km s^{-1}. This was calculated by inverting the Schmidt-Kennicutt relation (Kennicutt, 1998). If the gas surface density and star formation surface density are related according to Equation 3.2, then the total gas in a galaxy will be given by

$$M_{gas} = \frac{SFR}{\alpha} \left(\pi r^2 \right)^{(\nu-1)/\nu} , \qquad (3.4)$$

assuming the relation between CO luminosities and total mass is given by Equation 3.1. In this work we have assumed $\alpha_{\rm CO} = 4.6$, to ensure consistency with mass values determined at low and high redshift. The conversion between CO luminosities and line flux is

$$L'_{\rm CO} = 3.25 \times 10^7 \, S_{\rm CO}\Delta\nu \, \nu_{\rm obs}^{-2} \, D_{\rm L}^2 \, (1 + z)^{-3}, \qquad (3.5)$$

where $L'_{\rm CO}$ is the CO luminosity in units of K km s^{-1} pc^2 and $S_{\rm CO}\Delta\nu$ is the measured flux in Jy km s^{-1}. $\nu_{\rm obs}$ is the observed frequency of the CO(1-0) transition and $D_{\rm L}$ is the luminosity distance to the galaxy in Mpc (Solomon & Vanden Bout, 2005).

Following Equation 3.4, we have inferred gas masses for all galaxies in our sample from observed star-formation rates and optical half-light radii, and converted those values into expected CO fluxes.

The summary of observations, including observation dates and total integration time, can be found in Table 3.1. We have selected the CO(1-0) transition as the line of choice for these observations. Although higher transitions would provide us with higher S/N for the same integration times, targeting the lowest CO transition allows us to better trace the cold molecular mass, without the need to rely on any assumptions about gas excitations levels. At zero-th order, one could infer that CO luminosities are constant throughout all transitions, assuming the gas is thermalized. However, higher transitions require higher gas densities and may be tracing distinct regions of the ISM; furthermore, the gas may be subthermally excited (e.g., Weiß et al., 2007; Riechers et al., 2009; Harris et al., 2010). In addition, observations in the 3 mm band are simpler, since they do not have as strict weather requirements.

3.2.2 Data reduction

Data reduction was performed with the Miriad package.[1] Baseline solutions were chosen for each individual observed track. Data were mainly flagged according to variations in system temperature and resulting flux for a given gain calibrator, al-

---

[1]The package is available at http://bima.astro.umd.edu/miriad/

Table 3.1: Summary of CARMA observations

ID	RA	Dec	z	Observing date	ν_{obs} (GHz)	Total integration time (h)
001054	00:10:54.85	00:14:51.35	0.243	April 2010	92.7	7.2
015028	01:50:28.41	13:08:58.40	0.147	June 2011	100.5	20.7
080844	08:08:44.27	39:48:52.36	0.091	April 2010	105.6	3.4
092159	09:21:59.39	45:09:12.38	0.235	April 2010	93.3	5.4
210358	21:03:58.75	07:28:02.45	0.137	June 2011	101.4	15.3
231812	23:18:13.00	00:41:26.10	0.252	June 2011	92.1	16.1

though specifics vary greatly on an individual basis. When data were flagged only for a fraction of a track, care was taken always to include a gain calibrator observation up to 10 minutes before or after each astronomical datapoint. In the case of multiple observed tracks for a single source, those were later combined through use of the uvcat task in Miriad.

Visibility files were later inverted from UV-plane into real spatial/velocity flux datacubes. Velocity resolution varies according to signal-to-noise in the observations, but in most cases spectra shown here are defined in steps of 10 km s^{-1}, with 30 km s^{-1} smoothing. "Dirty" maps were cleaned through use of the "clean" procedure, and care was taken never to use a cutoff below the observed peak flux in Jy/beam of the galaxy.

3.3   Results

The final CO maps are shown in Figure 3.1. In Figure 3.3 we show the CO(1-0) line profile of galaxies in our sample as a function of velocity with respect to the measured systemic redshift in each case. This is determined from a box 6x6 arcsec^2 centered on the peak of emission in each map. Conversion from surface brightness (Jy beam^{-1}) to total flux per velocity element is done through determination of the synthesized beam shape (as given by the miriad *imfit* task).

To determine total flux in the galaxy, we fit a gaussian in each case. Flux is
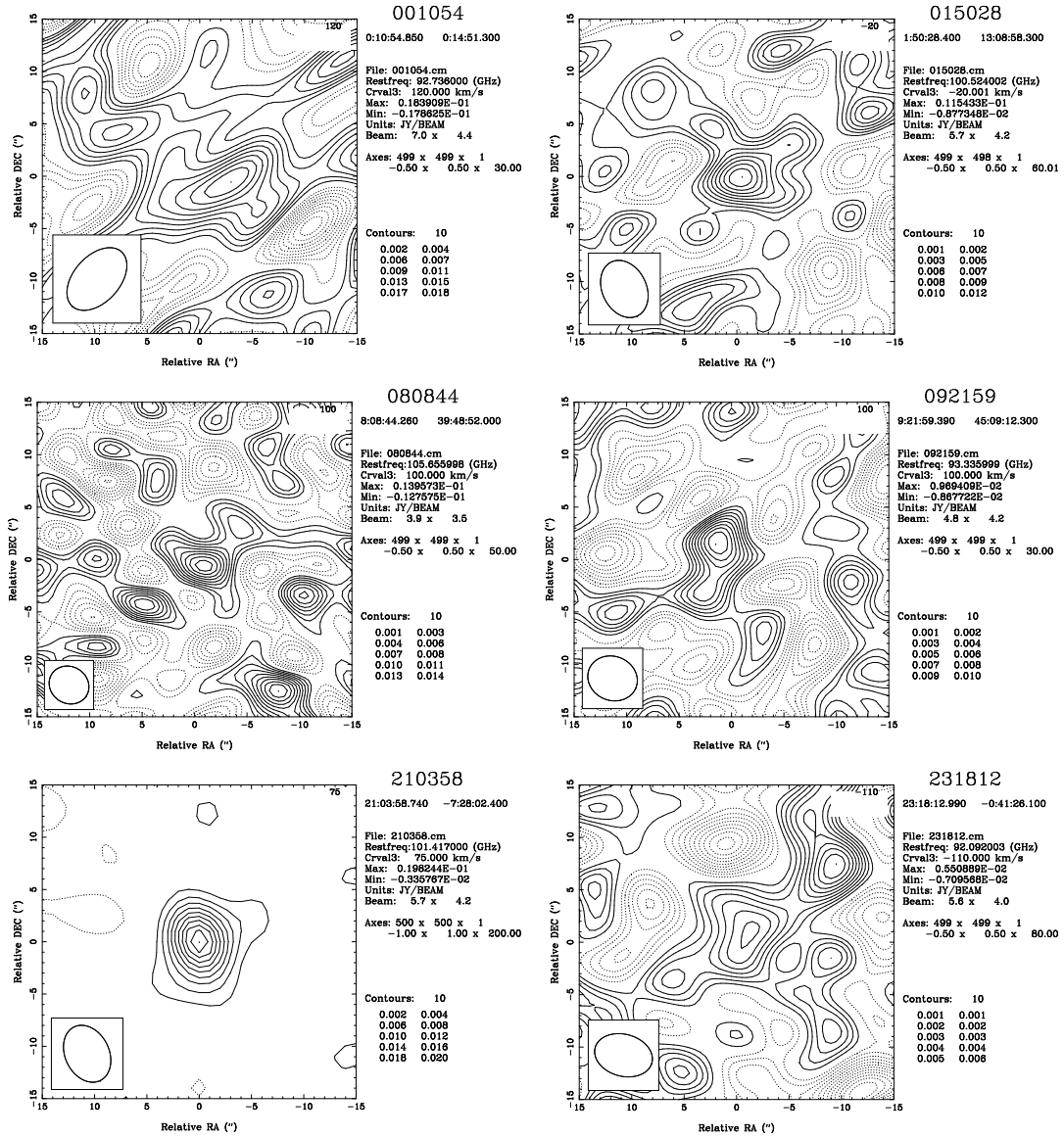
Figure 3.1: CO(1-0) contour maps showing the line emission in each galaxy. Also shown on the bottom-left corner is the synthesized beam size and shape in each case.

Table 3.2: Summary of CARMA results

ID	$S_{\mathrm{CO}}\Delta\nu$	L'_{CO}	$M(\mathrm{H}_2)$	f_{gas}
	(Jy km s^{-1})	(10^9 K km s^{-1} pc^2)	(10^9 $M_\odot$)	
001054	0.84±0.23	2.5	11.3	0.12
015028	1.50±0.45	1.5	7.2	0.26
080844	1.60±0.43	0.6	2.9	0.31
092159	1.97±0.89	5.4	24.8	0.28
210358	11.1±1.1	10.0	46.1	0.37
231812	1.00±0.42	3.1	14.6	0.59

then given simply by the area below the curve. This is subsequently converted to CO luminosities according to the relation given by Equation 3.5. Errors in flux measurements are the sum of the standard deviation on each velocity channel over 2σ (where σ is the velocity dispersion measured from the gaussian fitting).

In Table 3.3 we present the total CO(1-0) flux measured for each galaxy, along with inferred CO luminosities, molecular gas mass and gas fractions. In Figure 3.1 we show contour maps of all galaxies in our sample, and Figure 3.4 shows those same contours overlaid on HST blue or ultraviolet images (showing regions of intense star formation within each galaxy). Alignment is reasonable, although not perfect; however, resolution at this stage is not good enough to affirm whether there is a real offset between the gas reservoir and the starburst regions.

Greve et al. (2005) have shown that there is a clear correlation between the CO luminosity of a galaxy, L'_{CO} and its far-infrared (FIR) luminosity (L_{FIR}) that can be represented by

$$\log L'_{\mathrm{CO}} = 0.62 \log L_{\mathrm{FIR}} + 2.33. \tag{3.6}$$

In Figure 3.2 we show (as blue symbols) such correspondence between L'_{CO} and L_{FIR} for LBAs as measured with CARMA. For illustrative purposes, we also show this relation for the entire LBA sample; in this case, L'_{CO} is inferred from a simple inversion of the Schmidt-Kennicutt relation, as described by Equation 3.4. We notice that our sample is in very good agreement with the estimates from Greve et al. (2005), indicat-

erb
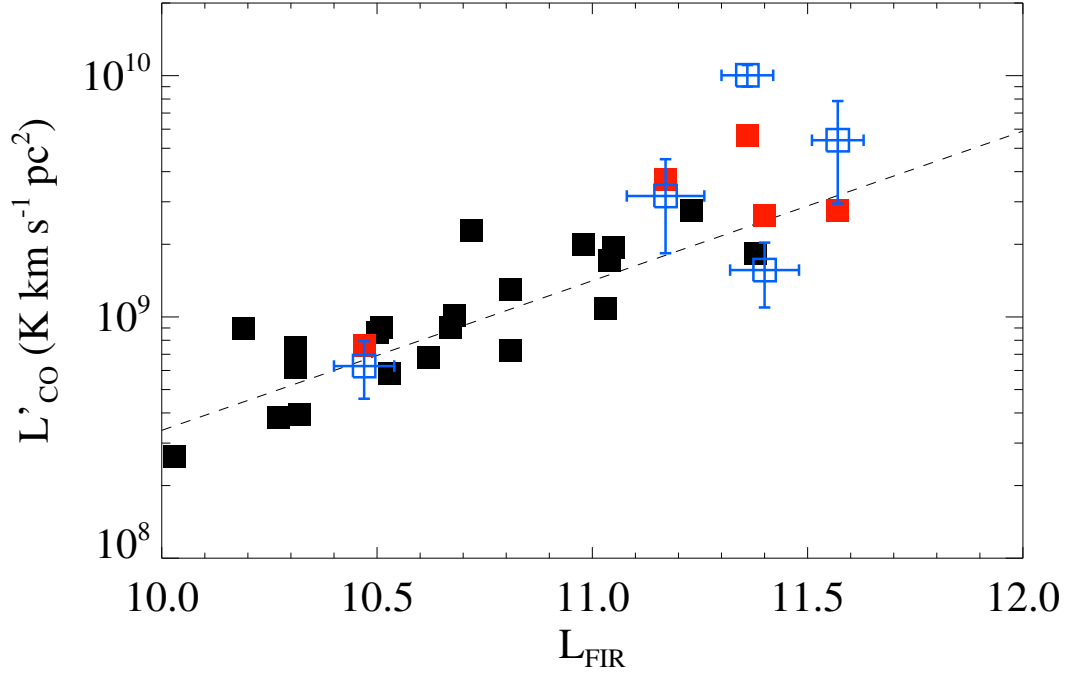
Figure 3.2: L'_{CO} versus L_{FIR} for LBA galaxies. The solid squares represent values inferred from inverting the Schmidt-Kennicutt relation, with galaxies observed with CARMA marked in red for quick comparison. Hollow blue squares show actual luminosity measurements from CARMA interferometric data. The dashed line is the correlation between L'_{CO} and L_{FIR} as described in Greve et al. (2005). One of the galaxies (001054) is not indicated here because we do not have L_{FIR} measurements for it.

ing star-formation processes in LBAs (and LBGs, by extension), is not dramatically different from other galaxies of similar luminosities.

3.3.1 Gas masses and fractions

We have converted the measured CO luminosities into molecular gas masses following the relation described in Equation 3.1. In doing so we have assumed the standard value of $\alpha_{CO} = 4.6$, as determined for the Milky Way galaxy. By defining the gas fraction as
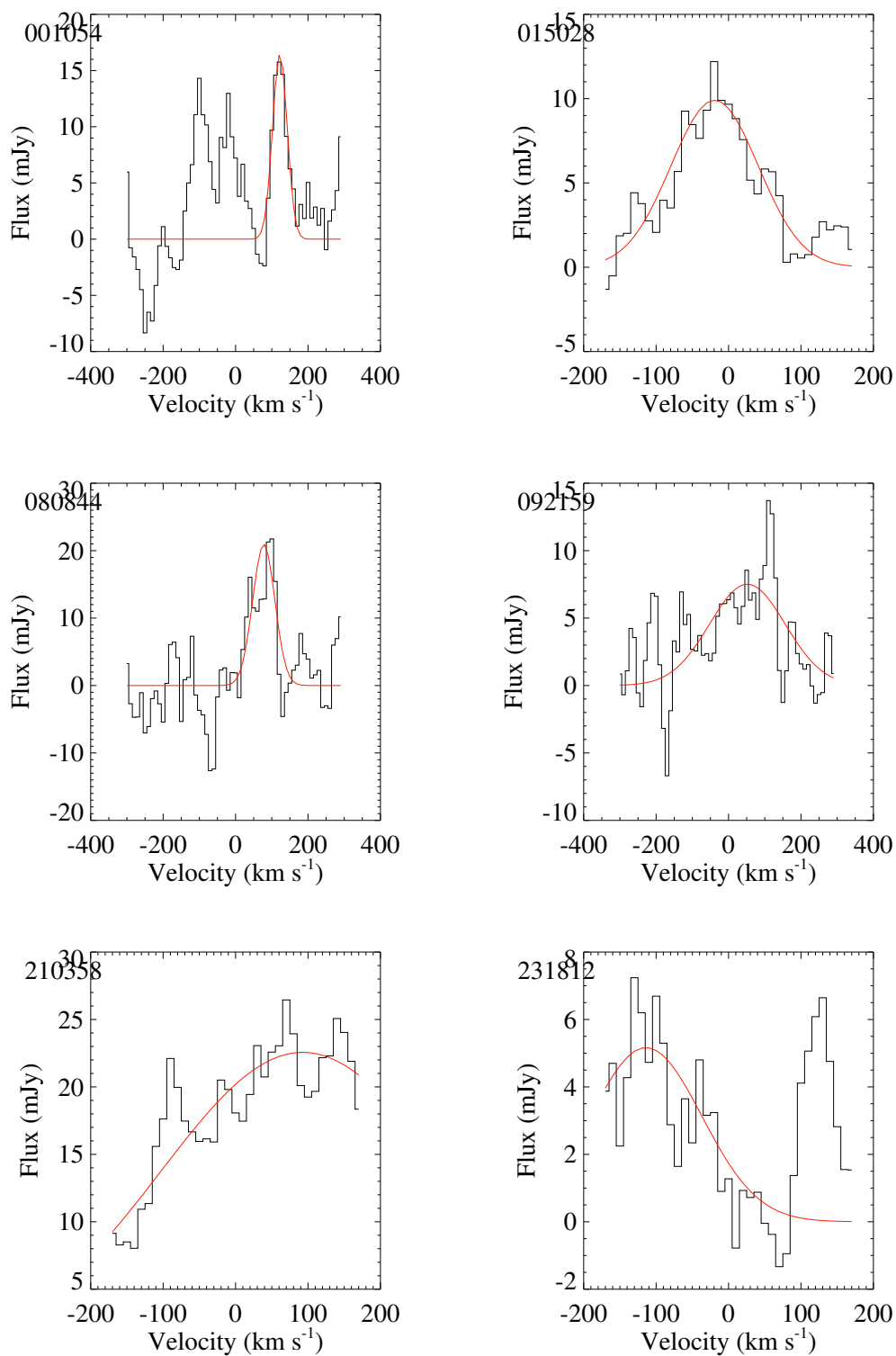
Figure 3.3: CO(1-0) velocity profiles of detected lines. A simple gaussian fit, used for flux measurements, is shown in red. Zero velocity is given by the measured redshift from the SDSS survey.
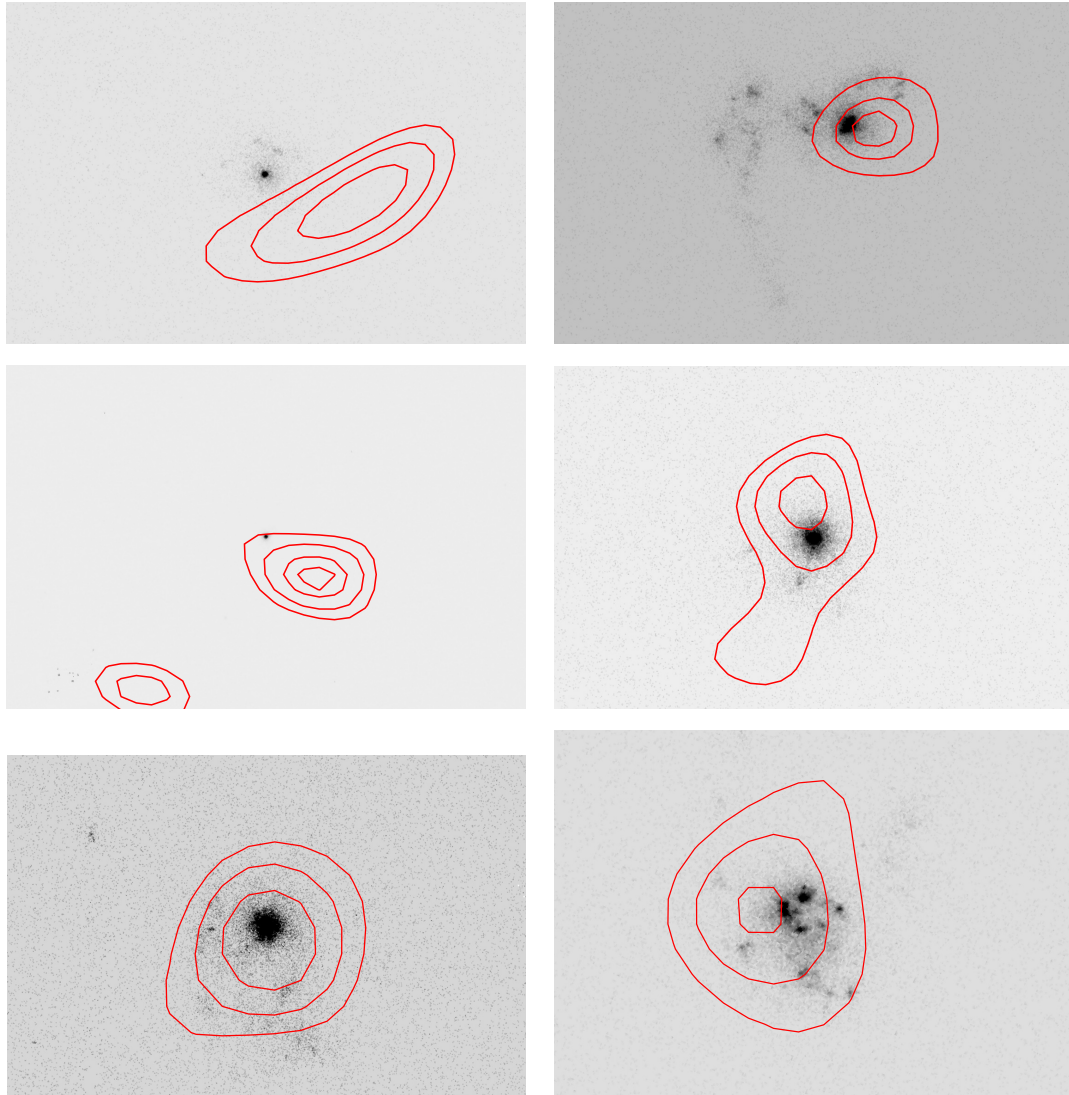
Figure 3.4: CO(1-0) images (red contours) on top of HST blue or ultraviolet images.

$$f_{\text{gas}} = \frac{M_{\text{gas}}}{M_* + M_{\text{gas}}},$$

(3.7)

one can also estimate the fraction of baryonic mass in the form of gas for each galaxy. We present these values in Table 3.3.

In Figure 3.5 we show the LBA gas fractions as a function of stellar mass, including also additional LBAs that have not yet been observed with gas fraction values inferred from inverting the Schmidt-Kennicutt relation. For comparison, we also include gas fractions estimated in the same manner for LBGs from Erb et al. (2006b). The first thing to notice is that measured values are in agreement with expectations, given the uncertainties. There is a clear trend of more massive galaxies showing smaller gas fractions, possibly indicating these galaxies have already consumed a larger portion of their gas reservoir and converted it into stellar mass. This trend is well reproduced by our LBA sample, again reinforcing the validity of the analogy between both galaxy populations.

3.3.2 The Schmidt-Kennicutt relation at low and high redshift

Whether the Schmidt-Kennicutt relation holds true for high-redshift starbursts – where higher SFR densities have been shown to exist (Shapley, 2011) – is still subject to some debate, as we have noted in Section 3.1. We expect the LBA sample, with more reliable measurements of CO luminosities, can shed some light on the issue.

In Figure 3.6, we show the most up-to-date compilation of the Schmidt-Kennicutt relation for star-forming galaxies, as presented in Daddi et al. (2010a). The low-density end of the plot shows low-redshift spiral galaxies from the sample of Kennicutt (1998). The remainder of the points show low- and high-redshift infrared bright samples (Kennicutt, 1998; Bouché et al., 2007) and "normal" star-forming galaxies at $z > 1$ from Tacconi et al. (2010) and Daddi et al. (2010a). To ensure consistency, we have measured gas surface densities for all galaxies on the lower relation (excluding SMGs and ULIRGs) with a uniform $\alpha_{\text{CO}} = 4.6$ value, from total gas and size
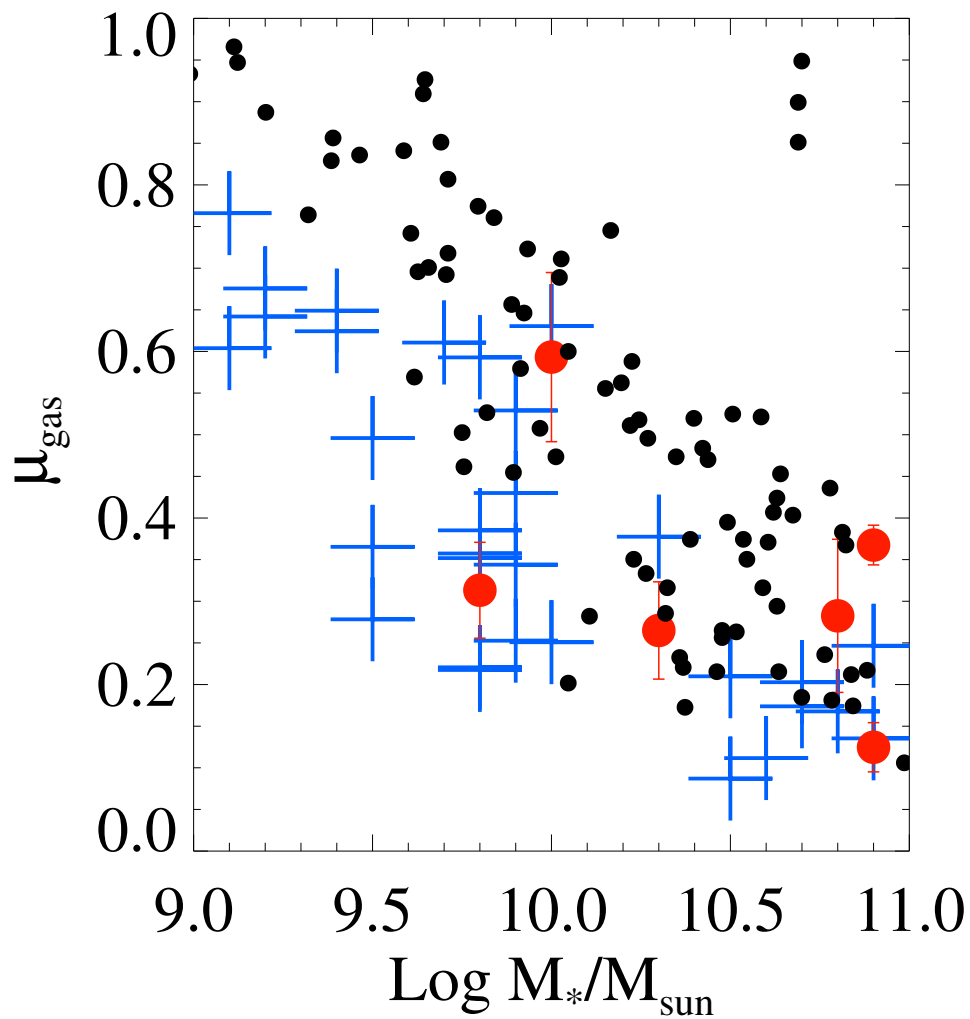
Figure 3.5: Gas mass fractions as a function of stellar mass for all LBAs in our sample, shown as blue crosses, estimated from Equation 3.4. The black dots show estimates for high-redshift LBGs, from Erb et al. (2006b). The red symbols indicate actual CARMA measurements.

measurements as mentioned in the original works.

As we can see, the relation is apparently bimodal, as indicated by both the solid and the dashed lines. The solid line is a fit to the "normal" galaxies at all redshifts, while the dashed line has the same slope, only displaced by 0.9 dex to fit through the ULIRGs and SMGs. Physically speaking, that means the latter are almost 10 times as efficient in converting cold gas into stars.

In Figure 3.7, we show the same points, only now the abscissa values have been divided by the dynamical times in the galaxy. Daddi et al. (2010b) have argued that this correction takes into account the ratio between dense gas and the more disperse reservoir, since dynamical times are expected to correlate with densities as $\tau_{\mathrm{dyn}} \propto \rho^{-0.5}$ (Silk, 1997). In that sense, the starburst galaxies have most of their gas highly concentrated in the star-forming regions, thus their star formation efficiencies are much higher. The end result is a single relation for *all* galaxies given by

$$\log \mathrm{SFR}/[\mathrm{M}_\odot \ \mathrm{yr}^{-1}] = 1.42 \times \log(\mathrm{M}_{H2}/\tau_{\mathrm{dyn}})/[\mathrm{M}_\odot \ \mathrm{yr}^{-1}] - 0.86. \qquad (3.8)$$

Whether that holds true for LBAs is not clear; our sample presents short dynamical timescales (of order a few tens of Myr), and appear to lie below the relation inferred by Daddi et al. (2010a). A larger sample is required to confirm whether this is actually the case, or if this is just an effect of scatter.

3.4 Discussion

One must be careful to take into account possible caveats in order not to over-interpret the data. In this section we list possible caveats that might affect how we view our results: the distinction between atomic and molecular gas, the adopted definition for dynamical timescale and the α_{CO} conversion factor.
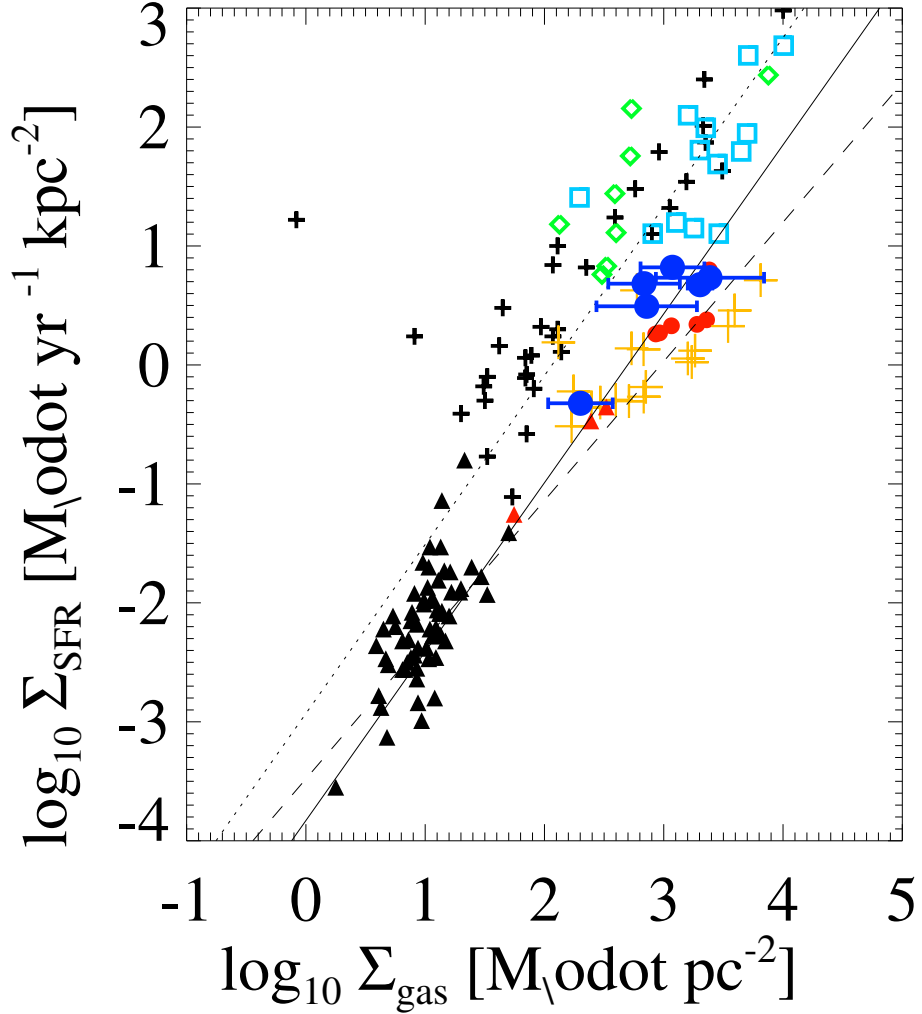
Figure 3.6: Star formation surface densities as a function of gas surface densities in extreme starburst galaxies. The two parallel lines describe the relation for regular star-forming galaxies and ULIRG-like objects, as described in Daddi et al. (2010a). Black crosses, green diamonds and blue squares represents ULIRGs and SMGs; black triangles, red triangles and red circles indicate spirals and disk-like galaxies at low and high redshifts. See Daddi et al. (2010a) and references therein for details. Blue filled circles represent our observed LBA sample, with range represented by the uncertainty in α_{CO}, as in Figure 3.5. The dashed line indicates the S-K relation for molecular gas as determined in (Genzel et al., 2010, see Section 3.4.1)
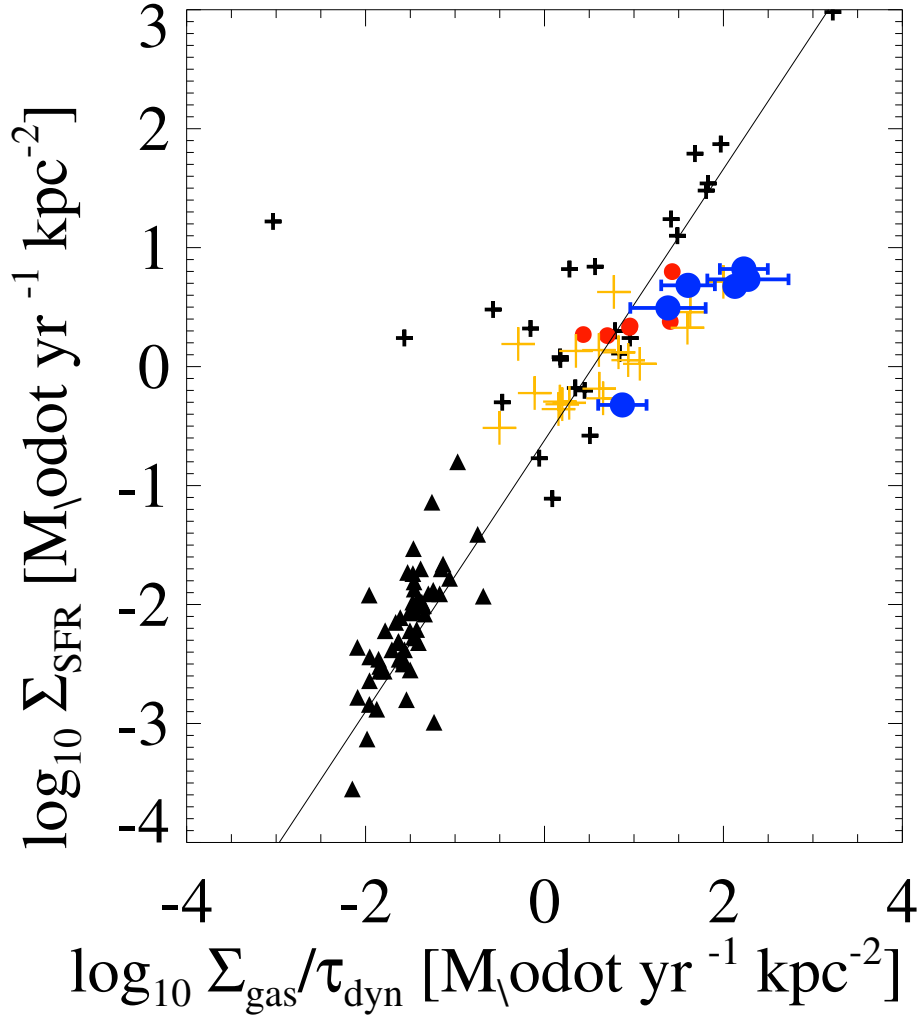
Figure 3.7: Star formation surface densities as a function of gas surface densities divided by dynamical time in star-forming galaxies. Symbols are the same as in Figure 3.6. The solid line is the universal relation for all star-forming galaxies as inferred by Daddi et al. (2010a). However, LBAs seem to indicate lower star formation rates for a given gas surface density even when dynamical times are taken into account, especially at higher densities.

3.4.1   Atomic and molecular hydrogen

First of all, one needs to be careful regarding total gas versus the molecular gas alone. At high redshifts, in particular, where the direct detection of atomic hydrogen is nearly impossible, it seems that *total* and *molecular* gas are used indistinguishably.

In fact, at the observed scales, it is true we expect the molecular gas to dominate the baryonic mass in the galaxy. As Bigiel et al. (2008) pointed out, the surface density of HI saturates at about 10 $M_\odot$ pc^{-2}, at least in the local universe. In our LBA sample the surface density of (molecular) gas is about a hundred times higher; therefore we would expect the atomic hydrogen to dominate the bulk of the mass only at distances greater than 10 times its optical radii, assuming constant surface density at this saturation level over the whole area.

Still, one needs to be careful to distinguish between both definitions. While Daddi et al. (2010a) have made comparisons with the Schmidt-Kennicutt relation for *total* gas, Genzel et al. (2010), for example, determine the relation between star formation surface density and the surface density of *molecular* gas, finding an exponent closer to the linear ($N = 1$) relation found for molecular gas only by Bigiel et al. (2008):

$$\log \text{SFR}/[\text{M}_\odot \ \text{yr}^{-1}] = 1.17 \times \log(\text{M}_{H2})/[\text{M}_\odot] - 3.48. \qquad (3.9)$$

This is indicated as the dashed line in Figure 3.6. While this latter relation seems more appropriate for the galaxies described in Tacconi et al. (2010), the S-K relation for LBAs is more accurately by Equation 3.2. We argue that different samples yield different results, which ultimately means an uncertainty in the fit for the Schmidt-Kennicutt relation.

3.4.2   The dynamical timescale

Likewise, we need to ensure we understand the meaning of dynamical time in these galaxies. In principle, the dynamical time represents the amount of time a single star takes to orbit around the galaxy. This timescale can be linked to the duration of processes that can spread throughout a given radius; for instance, a simple model

for star formation in a galaxy through the collapse of cold molecular gas requires the cooling time to be shorter than the dynamical timescale within a given radius.

In the case of high-redshift galaxies, however, the definition of the dynamical timescale is not so clear. In Figure 3.7, for example, all "normal" galaxies at high redshift have dynamical timescales defined as the rotation timescale at the half-light radius, while for the local sample of spirals and ULIRGs (Kennicutt, 1998) this quantity is defined at the outer radii of galaxies.

More importantly, though, we question the validity of characterizing dynamical timescales in all star-forming galaxies by use of circular velocities. As we have seen in Chapter 2, not all star-forming galaxies at high redshift can be accurately described as rotating disks, especially at low stellar masses. Velocity dispersions in SMGs, in particular, are remarkably high, so perhaps using $t_{\mathrm{dyn}} \sim r/\sigma$ might be a better description (for a detailed discussion of the resolved gas kinematics in SMGs, see Menéndez-Delmestre et al., in prep.). Therefore, one should be careful when comparing different samples like those, in that a uniform analysis of their dynamics is perhaps not so simple.

3.4.3   The CO→ H$_2$ conversion factor

This determination is particularly important because the bimodality observed in the Schmidt-Kennicutt relation can be attributed, at least in part, to the use of different α_{CO} values for dusty and ultraviolet bright samples.

In the case of high-redshift galaxies, such measurements are nearly impossible, and one has to rely on empirical results for low-redshift galaxies, which present dramatically different ISM properties and might misrepresent the problem.

As an example, Genzel et al. (2011) have attempted such a measurement at high redshift, assuming gas masses from simple inversion of the S-K law and comparing with observed CO luminosities. The authors then attempt to infer a power-law relation between metallicity and α_{CO}, by using measured values from Leroy et al. (2011). The resulting empirical relation is as follows:

$$\log \alpha_{\mathrm{CO}} = -1.3 \times \mu_0 + 12.1, \tag{3.10}$$

where μ_0 is the metallicity as defined by Denicolo et al. (2002). However, whether that parallel between local spirals and high redshift is valid is debatable. We know that at $z \gtrsim 2$, densities, metallicities and stellar masses, amongst other observables, are distinct from those seen in local galaxies, and it would be expected that the α_{CO} for a galaxy of given metallicity will be different at $z = 0$ and $z = 2$.

To illustrate this statement, we compared estimated values for α_{CO} in all objects in our sample (estimating gas masses from Equation 3.4 and CO luminosities from Equation 3.6). We converted between metallicities following the empirical relation found in Kewley & Ellison (2008). We then compared these estimates with values found in Genzel et al. (2011). At high metallicities there is good agreement between our sample and the high-redshift one; however, at low metallicities, our inferred α_{CO} are smaller than local galaxies with similar metallicities almost by a factor of 5.

Another way to look at the problem is pictured in Figure 3.9, where we show values of L'_{CO} versus L_{FIR}, as in Figure 3.2, but this time we infer CO luminosities assuming an α_{CO} conversion factor as described in Genzel et al. (2011). We notice that the inferred CO luminosities are much lower than expected for a given FIR luminosity, because at lower luminosities (i.e., lower metallicities) the same gas masses would produce much fainter CO emission. The conclusion is that one of three assumptions must be wrong: either (1) the $L'_{\mathrm{CO}} - L_{\mathrm{FIR}}$ is not valid for LBAs; (2) the S-K relation is not valid for LBAs; or (3) the $\alpha_{\mathrm{CO}} - Z$ relation is not valid for LBAs.

3.4.4 Future perspectives

We expect this work to be the beginning of a larger, more ambitious project aiming to investigate the molecular gas in UV-bright starburst galaxies. Thus far we have only observed six objects with the CARMA interferometer, but this is partly because so far we have only used the CO(1-0) transition, for reasons explained in Section 3.2.1. However, according to Equation 3.5, if we assume thermalized emission from
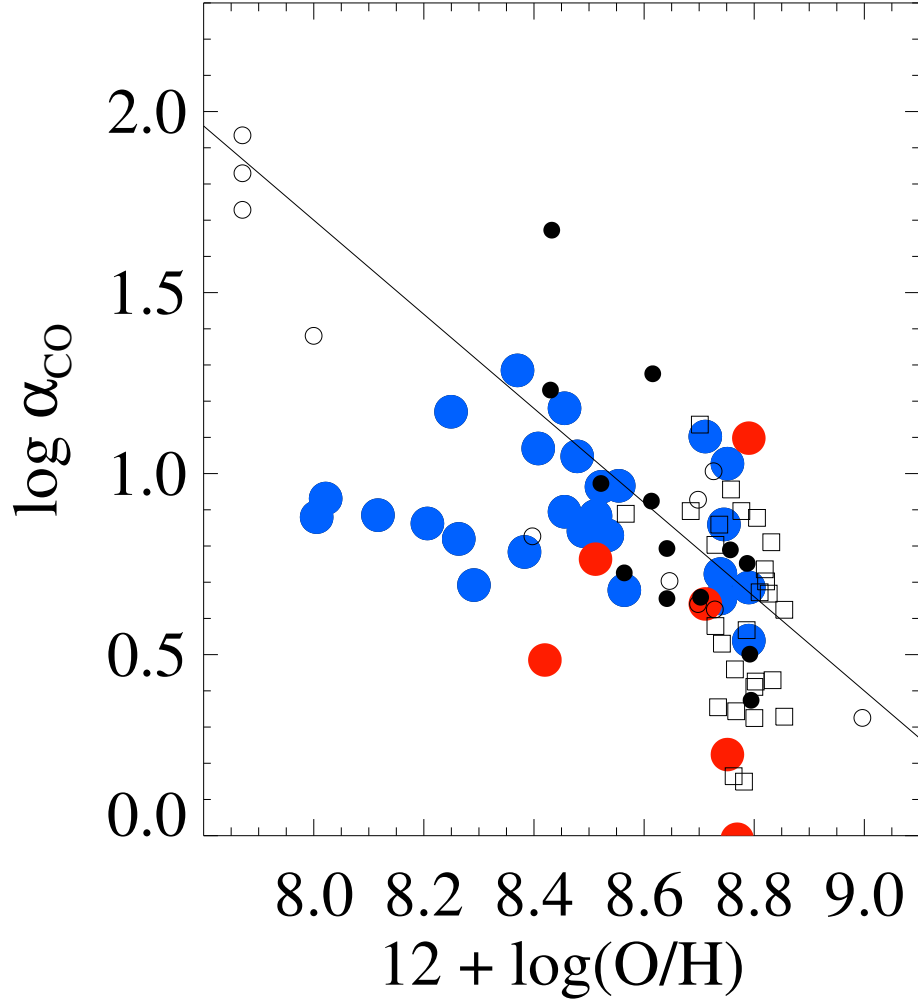
Figure 3.8: α_{CO} as a function of metallicity. Colored symbols indicate our LBA sample; red circles represent the observed objects, while blue circles are α_{CO} inferred from the S-K relation. Small black dots and squares are the high-redshift objects from Tacconi et al. (2010) and Daddi et al. (2010a). Hollow small circles are the local galaxies from Leroy et al. (2011). There is good agreement between LBAs and high-redshift galaxies. The solid line represents the empirical relation found in Genzel et al. (2011) using all samples; low-metallicity LBAs appear to lie below that relation by a factor of ~ 5.
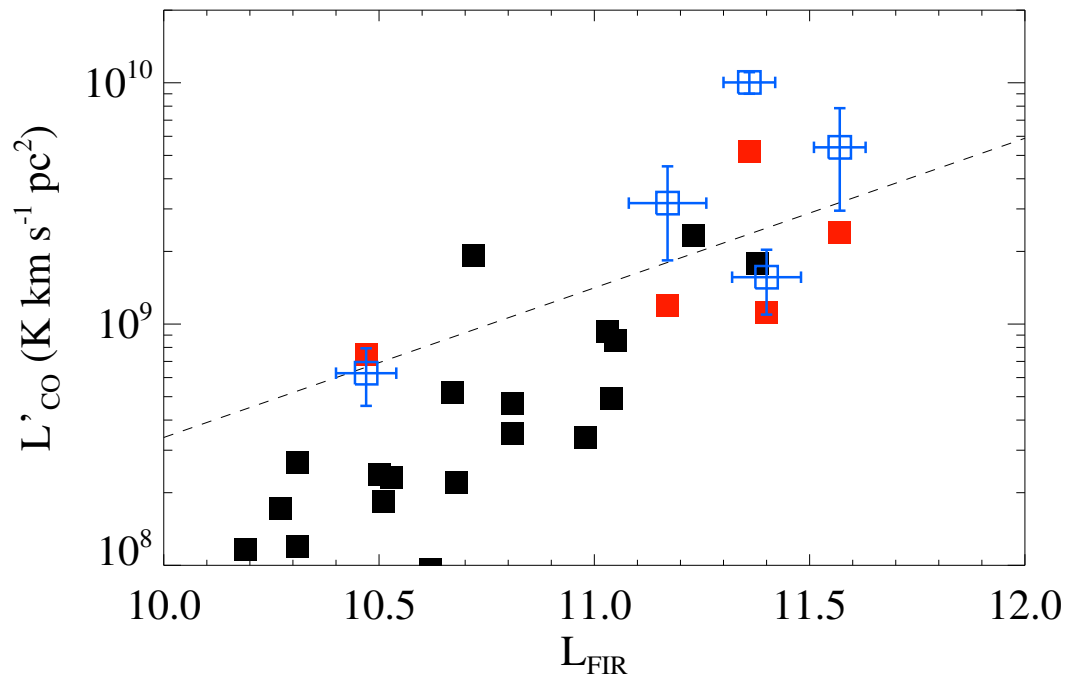
Figure 3.9: Same as Figure 3.2, but following the metallicity dependence of α_{CO} described in Genzel et al. (2011).

all CO transitions, then total flux will scale as ν^2. Since higher transitions of CO have rest frequencies which are multiples of the CO(1-0) 115 GHz line, one would expect fluxes 9 times higher for CO(3-2), for instance. Even though this is generally not true, due to subthermal excitation of the CO line at higher transitions, and the fact that different transitions trace molecular gas at distinct densities, the CO(3-2) line is generally expected to be 4–6 times brighter than CO(1-0) in star-forming galaxies.

Furthermore, the advent of ALMA will dramatically improve current capabilities of CO studies at low and high redshift. ALMA will provide much faster survey speeds than currently possible, due to a number of technical improvements on antenna and receiver design, as well as a much larger collecting area than existing instruments. ALMA is currently going through its early science phase, which already contains 16 12-m antennas. Once completed in 2013, the array will comprise 50 such antennas, for unparalleled sensitivity in millimeter-wave interferometry. As an example, one of ALMA's goals is to be able to detect a Milky-Way-like galaxy at redshift $z = 3$ in under 24 hours.

We have recently proposed to observe a sample of 14 LBAs with the ALMA interferometer. We have proposed to search for CO(3-2) emission, which, according to our estimates, should take less than 5 minutes per object for an average $S/N > 5$ per velocity resolution element in most cases. In addition, this survey will allow us to extend our data to much fainter galaxies, reaching values of approximately $1/10 \, L^*(z = 2)$. In that way, we will be able to study the gas reservoir in less metal-rich, less massive galaxies, which are believed to dominate the star formation density of the universe at high redshfits Reddy & Steidel (2009).

3.5 Summary

We have initiated a survey searching for CO(1-0) emission in Lyman break analogs, in an attempt to measure gas fractions in these galaxies and obtain further insight toward the interaction between star formation and the gas reservoir in UV-bright starbursts. We discuss expectations using well-established relations for the local universe (such

as the Schmidt-Kennicutt relation) and observed surface densities and gas fractions of high-redshift star-forming galaxies.

Using the CARMA interferometer, we have detected six objects at high signal-to-noise. These galaxies show strong emission, indicative of high gas masses and gas fractions. These values agree with our expectations, further supporting our use of LBAs as low-redshift proxies for galaxy formation scenarios at earlier epochs.

Furthermore, we have shown that LBAs follow the local Schmidt-Kennicutt relation, albeit at much higher surface densities than typical spirals at $z \sim 0$. This is in accordance with other high-redshift populations (Daddi et al., 2010b), and the result distinguishes our sample from infrared-bright objects such as ULIRGs and SMGs. The authors in that work have argued that the bimodality can be removed if one takes into account the dynamical times of each object. This is still uncertain in the case of our galaxies; there is an apparent shift to smaller star formation rate surface densities even when taking into account dynamical times, but with only six objects this is not a definitive result.

The upcoming operations of ALMA will definitely make a great impact on this project. We will be able to observe fainter, lower metallicity objects, and at the same time we will map the CO emission at much higher densities. Once those data become available, we hope the scenario for the physical processes regarding the collapse of the molecular clouds and subsequent star formation will become clearer.

Chapter 4

Mass flux in the green valley at intermediate redshifts

4.1 Introduction

There has long been a distinction between blue star-forming galaxies and red passively evolving ones. In his seminal classification article, Hubble (1926) classified galaxies into two main groups, spirals and elllipticals. Although unintended as a timeline for secular evolution – in Hubble's own words, "The entire classification is purely empirical and without prejudice to theories of evolution" (Hubble, 1927) – ellipticals were referred to as "early-type galaxies" and spirals as "late types" (see also Fortson et al., 2011).

Our knowledge of stellar populations in galaxies has evolved considerably since then. Today we know that spiral galaxies are blue due to young stars, and that their current star formation rates are higher than in ellipticals, with a younger population, on average. We also know that spiral galaxies in the local universe are preferentially found where the galaxy number density is higher within clusters (Dressler, 1980), which gives us important clues regarding the late evolution of galaxies. This leads to the conclusion that galaxies *somehow* evolve from spirals into ellipticals at later times. However, the existing bimodality in the galaxy distribution, with a clear distinction between blue spirals and red spheroids, and its establishment still remain a puzzle.

The color bimodality has been observed at low redshifts ($z \sim 0.1$) with the Sloan

Digital Sky Survey (SDSS; Baldry et al. 2004). Willmer et al. (2006) have shown this bimodality extends to a time when the universe was approximately half its current age, based on a large sample of intermediate redshift galaxies ($z \sim 0.7$). If the color distribution of galaxies can be described as two distinctive peaks, then one can denominate the minimum at intermediate color values the "green valley." The question then arises: why does such a minimum exist, instead of a homogeneous distribution across the color-magnitude diagram?

In order to study this intermediate population, one needs to determine proper selection criteria. Wyder et al. (2007) have measured number densities in the color-magnitude diagram at low redshift ($z \sim 0.1$) and found that GALEX NUV minus r-band magnitudes represent an easier color criterium to select green valley galaxies. Ultraviolet emission originates from recent (over the last tens of millions of years) star-forming regions in the galaxy, while the r-band is more sensitive to the bulk of stellar mass, formed over the course of the galaxy's history. By subtracting the two, one can clearly distinguish two populations, one actively star-forming and the other older, more passive, with a dynamic range of about 6 magnitudes in color. Nevertheless, we need to be careful when defining transition galaxies; contamination from obscured galaxies is high, since these are typically galaxies with high ratio of current to past star formation, but which present redder colors due to dust obscuration (Martin et al., 2007; Salim et al., 2009, see also Section 4.3.4).

The low number density (or number deficit) of galaxies in the green valley indicates that the transition between both groups occurs rapidly. A number of works attempt to explain why there is such a rapid evolution. Menci et al. (2005) postulate that supernova winds and outflows can play an important part, driving out gas that fuels star formation in the galaxy. Di Matteo et al. (2005), on the other hand, have produced a hydrodynamical simulation of a major merger event that shows that, after a period of brief increase of star formation, the supermassive black hole created in the center of the merger remnant drives strong outflow winds that rapidly quench star formation. Nandra et al. (2007) and Schawinski et al. (2009) provide observational support to this hypothesis, finding a large number of active galactic nuclei (AGN) in

the green valley and concluding that feedback from such objects might be somehow quenching the star formation process. This is further supported by Coil et al. (2008), who note that the coadded spectra of green valley galaxies at $z \sim 1$ is distinct from coadded spectra of blue and red galaxies, with line ratios that show increased AGN activity. Nevertheless, Mendez et al. (2011) note that the merger fraction in the green valley is low, from quantitative morphological analysis of $0.4 < z < 1.2$ optically selected transition galaxies. The authors then conclude that mild external processes (such as galaxy harassment) or secular evolution are the dominant factors at these redshifts.

To infer how rapidly galaxies are moving across the green valley, Martin et al. (2007) (hereafter Paper I) have used spectroscopic features in green valley galaxies to obtain information on their star formation histories (see Section 4.2 for details). Along with measurements of typical galaxy masses and number densities in the color-magnitude diagram, the authors have been able to determine the mass flux across the green valley at low redshifts ($z \sim 0.1$). The measured value of $\dot{\rho} = 0.033$ M$_\odot$ yr^{-1} Mpc^{-3} agrees remarkably well with expectations from the growth of the red sequence and the depletion of galaxies in the blue sequence at such redshifts (Bell et al., 2004; Faber et al., 2007). Furthermore, the authors find evidence for an increase in number density of AGN in the green valley (from measured [OIII] luminosities), supporting aforementioned studies that relate AGN activity with the quenching of star formation (although the correlation between [OIII] luminosities and quenching timescales is not unequivocal).

In this work, we attempt to reproduce the methodology introduced in Paper I, but at higher redshifts. This will allow us to measure the mass flux in the green valley at intermediate redshifts, comparing with results found for galaxies in the low-redshift universe. Although the technique is simple, the data acquisition process proves challenging, since it requires reliable measurements of absorption features in galaxies at redshifts of ($z \sim 0.8$). We have set out to obtain the required data, and the work presented here includes the deepest spectra of green valley galaxies to date.

This chapter is organized as follows. In Section 4.2, we describe in detail the

methodology used to infer star formation histories of galaxies, including modelling of stellar populations. In Section 4.3 we describe the observations and data reduction used to produce the spectra that were then used to measure star formation histories and quenching timescales, in addition to ancillary data used to measure number densities in the color-magnitude diagram, luminosity functions and extinction correction. Section 4.4 shows our results, including the measured mass flux density at $z \sim 0.8$ and in Section 4.5 we discuss those results in light of galaxy evolution models. We summarize our findings in Section 4.6.

4.2 Methodology

The method to study the mass flux in the green valley has been introduced by Martin et al. (2007). We summarize here the description presented in that work.

4.2.1 The mass flux density in the color-magnitude diagram

In order to measure the mass flux for a given color in the color-magnitude diagram, $\dot{M}(r, y)$, where y is the $NUV - r$ color of the galaxy, we can assume that

$$\dot{M}(r, y) = M(r, y) \times \frac{dy}{dt}, \tag{4.1}$$

where $M(r, y)$ is the average mass of a galaxy in that color-magnitude bin, and dy/dt is how fast galaxies are moving through the same bin. In practice, we measure average values in a two-dimensional bin. Dividing the above equation by the comoving density probed, we calculate

$$\dot{\rho}(r, y) = \Phi(r, y) < M(r, y) > \frac{dy}{dt}. \tag{4.2}$$

In this case, the comoving mass density $\rho(r, y)$ is simply the comoving number density $(\Phi(r, y))$ multiplied by the typical galaxy mass in that bin $(< M(r, y) >)$. What we propose to measure is the mass flux density $\dot{\rho}$. Since we can constrain $\Phi(r, y)$ and $< M(r, y) >$ independently from the star formation histories, we are only left with

the task to measure the color evolution rate for a given galaxy or bin.

4.2.2 Star-formation histories

In order to measure the color evolution rates, we make some simplifying assumptions:

1. Galaxies only move towards redder colors, i.e., we do not consider starbursting red galaxies moving downward in the color-magnitude diagram;

2. The star formation histories in all galaxies are described by a constant star formation rate for the first few Gyr (approximately 6 Gyr) followed by a period of exponentially declining star formation rates:

$$
\text{SFR}(t) = \begin{cases} \text{SFR}(t=0), & t < t_0 \\ \text{SFR}(t=0)e^{-\gamma t}, & t > t_0 \end{cases}
\tag{4.3}
$$

We discuss the implications of this model in Section 4.5.2.

In order to measure the exponential index γ, we apply the same methodology described in Kauffmann et al. (2003) to measure the rest-frame 4000 Å break and the equivalent width of H_δ absorption. The first is created by the accumulation of a large number of ionized metal line absorption shortward of 4000 Å (Bruzual, 1983). These lines are multiply ionized in hot stars, with smaller opacities in younger galaxies, and thus the break correlates with the age of the stellar population. The latter is mainly present in the stellar photosphere of smaller early-type stars (mostly A stars), which dominate 0.1–1.0 Gyr after a starburst event (and after evolution of O and B stars off the main sequence).

In this work, we use the same definitions as in Paper I, in order to maintain uniformity across different redshifts. The first index, $D_n(4000)$, is defined as the ratio of the average flux density F_ν in the bands 3850–3950 and 4000–4100 Å, following the definition of Balogh et al. (1999). The narrow bands ensure that the ratio is weakly dependent on flux calibrations and other broad-band effects that may arise from data reduction. For the latter, $H_{\delta,A}$ is the absorption equivalent width; the continuum is

defined by fitting a straight line through the average flux density between 4041.60 and 4079.75 Å, on one end, and 4128.50 and 4161.00 Å, on the other. The equivalent width, then, is given simply by

$$H_{\delta,A} = \sum_{\lambda=4083.5}^{4122.25} \left(1 - \frac{F_\nu}{F_{\nu,cont.}} \right). \tag{4.4}$$

Kauffmann et al. (2003) showed that these indices trace a well-defined region in a $Dn(4000)$ vs. $H_{\delta,A}$ diagram. Furthermore, different star formation history tracks – for instance a single starburst event versus a continuous star formation rate – trace distinct regions within this diagram. We therefore use our measured spectral indices as defined above to distinguish between different star formation histories, in our case as given by different γ values.

In Figure 4.1, we show five tracks on the $Dn(4000)$ vs. $H_{\delta,A}$ diagram given by five distinct γ values (0.5, 1.0, 2.0, 5.0 and 20.0 Gyr^{-1}). These models were produced with the Bruzual & Charlot (2003) models – with Chabrier (2003) initial mass functions, Padova 1994 stellar evolutionary tracks and solar metallicities – by varying ages throughout star formation histories as described in Equation 4.3. The range of values for t_0 is limited to $t_0 < t_z$, so that the oldest models are always below the universe age at the highest redshift we measure. This does not have a major impact on our results, since t_0 is typically larger than the time when $D_n(4000)$ and $H_{\delta,A}$ have stabilized. We notice very distinct tracks, with the strongly quenched models (higher γ presenting higher $H_{\delta,A}$ values).

Finally, the measurement of dy/dt is given by the width of the color range in magnitudes used to determine the green valley divided by the duration of time when the galaxy is within those boundaries. We illustrate this in Figure 4.2, where we plot the NUV $- r$ color as a function of time after the initial period of constant star formation, with the green valley limits indicated by horizontal lines. As expected, models with higher values of gamma (i.e., that are quenching their star formation more rapidly) change colors faster. The timescales to cross the green valley in these models varies between 0.26 and 2.7 Gyr.
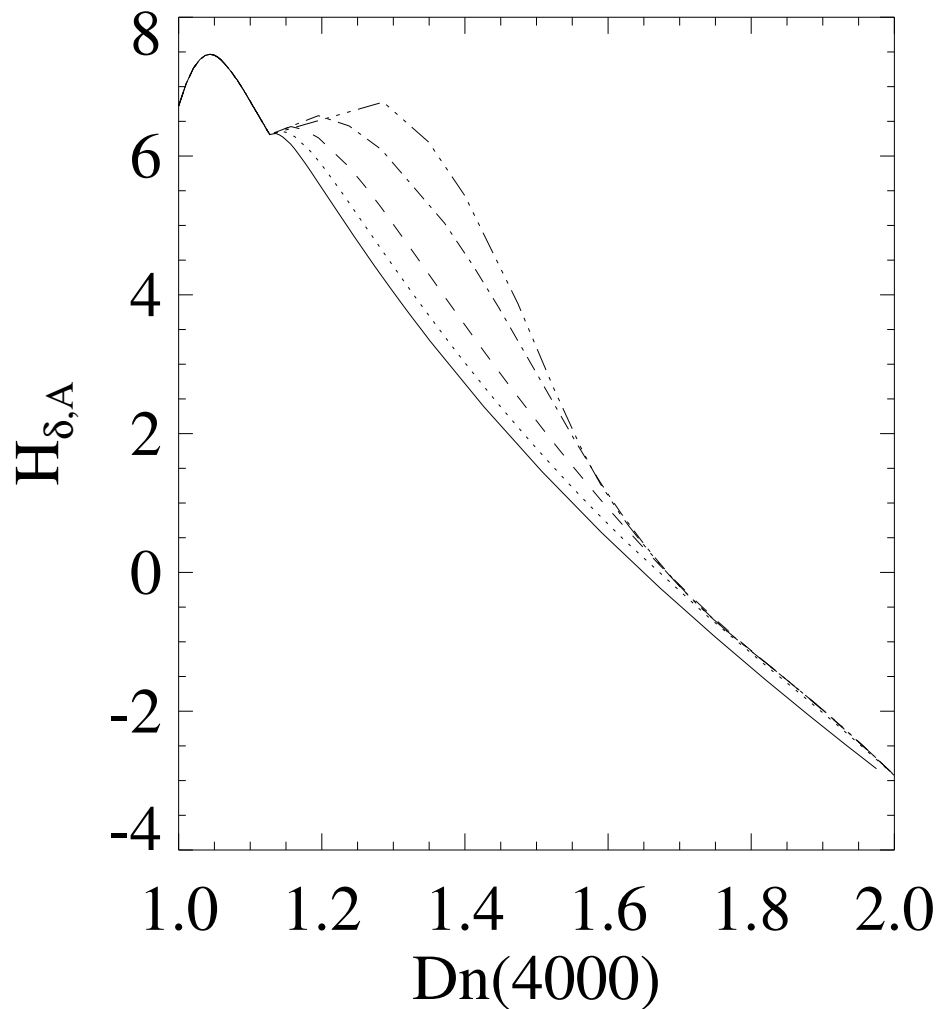
Figure 4.1: Evolution of $D_n(4000)$ vs. $H_{\delta,A}$ for models with different star formation histories. Solid, dotted, dashed, dotted-dashed and triple-dotted-dashed lines (from left to right) represent γ's equal to 0.5, 1.0, 2.0, 5.0 and 20.0 Gyr^{-1}, respectively. Therefore, models to the right are quenching star formation more rapidly.
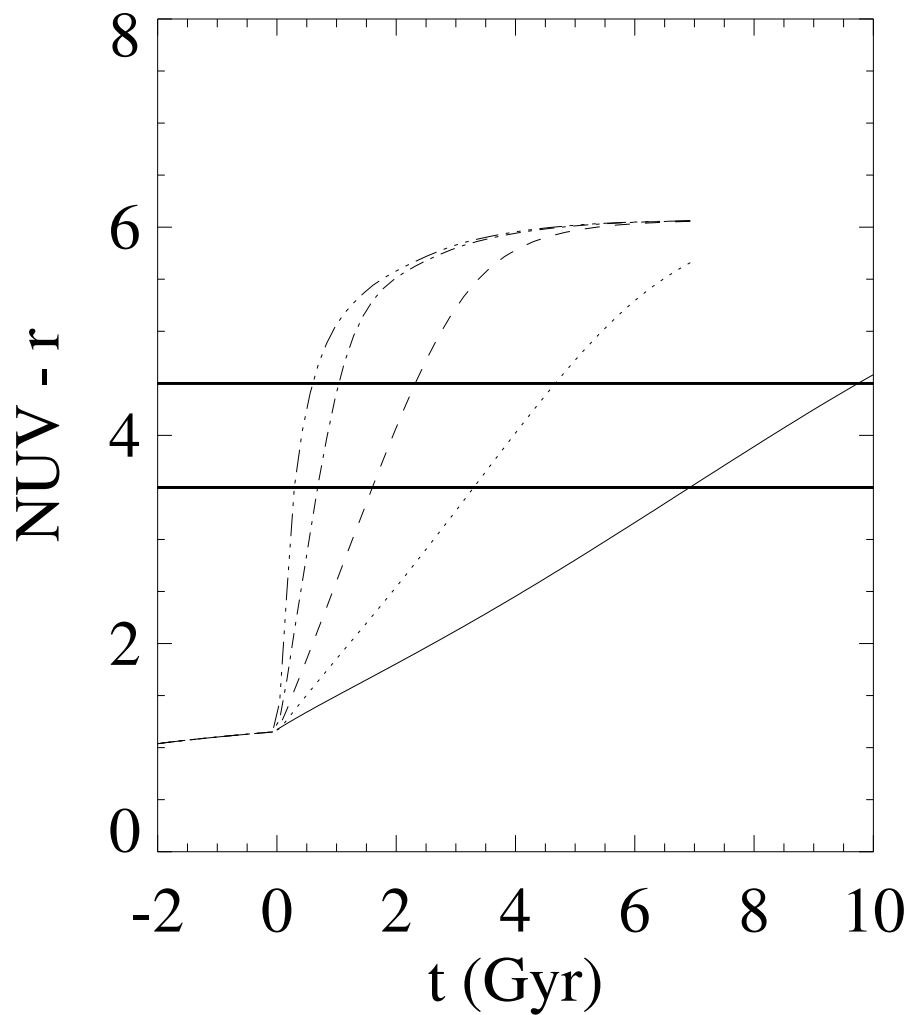
Figure 4.2: $NUV - r$ colors of model galaxies as a function of time after the onset of exponential decline in SFR. Line types are the same as in Figure 4.1. The thick horizontal lines indicate the threshold we have used to determine the green valley. dy/dt will then simply be the width of the magnitude band in colors divided by the time take for a galaxy to cross both thresholds.

4.3   Sample, observations and data processing

4.3.1   Sample selection

We have selected a sample of 163 green valley galaxies from surveys at intermediate redshift surveys. Preference has been given to galaxies in the Extended Groth Strip (EGS), which is the target of the ongoing All-wavelength Extended Groth Strip International Survey collaboration (AEGIS; Davis et al., 2007). This field is optimum for galaxy evolution studies, since the AEGIS collaboration has produced a large amount of ancillary multiwavelength data. In particular, a large subsample of galaxies has spectroscopically determined redshfits with the DEEP2 survey (Davis, 2003). However, in order to facilitate observations throughout the year, we have also used data from the Canada-France-Hawaii Telescope Legacy Survey (CFHTLS),[1] from all deep fields observed.

All galaxies observed in this work have CFHTLS photometry in all five bands (u, g, r, i, z). This is required to properly constrain SDSS r'-band magnitudes in the galaxy's rest frame, while simultaneously yielding accurate GALEX NUV rest frame magnitudes. The CFHTLS Deep Field D3 overlaps with the EGS, and in that case we match CFHTLS and DEEP2 sources. We preselect galaxies with redshifts between $0.55 \leq z \leq 0.9$; DEEP2 redshifts were used for the selection in the EGS field, CFHTLS photometric redshifts are used otherwise (approximately 50% of our final sample).

All sources have been k-corrected to redshift $z = 0$ using the Kcorrect code (version 4_2; Blanton & Roweis, 2007), so that we could select them based on rest-frame NUV-r colors. In Figure 4.3 we show the result of the k-correction processes, showing all galaxies below the completeness limits in CFHTLS-Deep. We also indicate the color selection criterium, showing the color limits for the green valley galaxies as dashed lines.

In Figure 4.4 we show image stamps obtained with HST in EGS field with the ACS instrument in the V and I bands (Davis et al., 2007; Lotz et al., 2008). We note

---

[1]http://www.cfht.hawaii.edu/Science/CFHTLS/

that although most portrayed galaxies are small spheroids, the presence of disks is significant ($\leq 40\%$). One of them is clearly an ongoing merger. A detailed morphological analysis is beyond the scope of this work; for an in-depth discussion on the morphology of green valley galaxies, see Mendez et al. (2011).
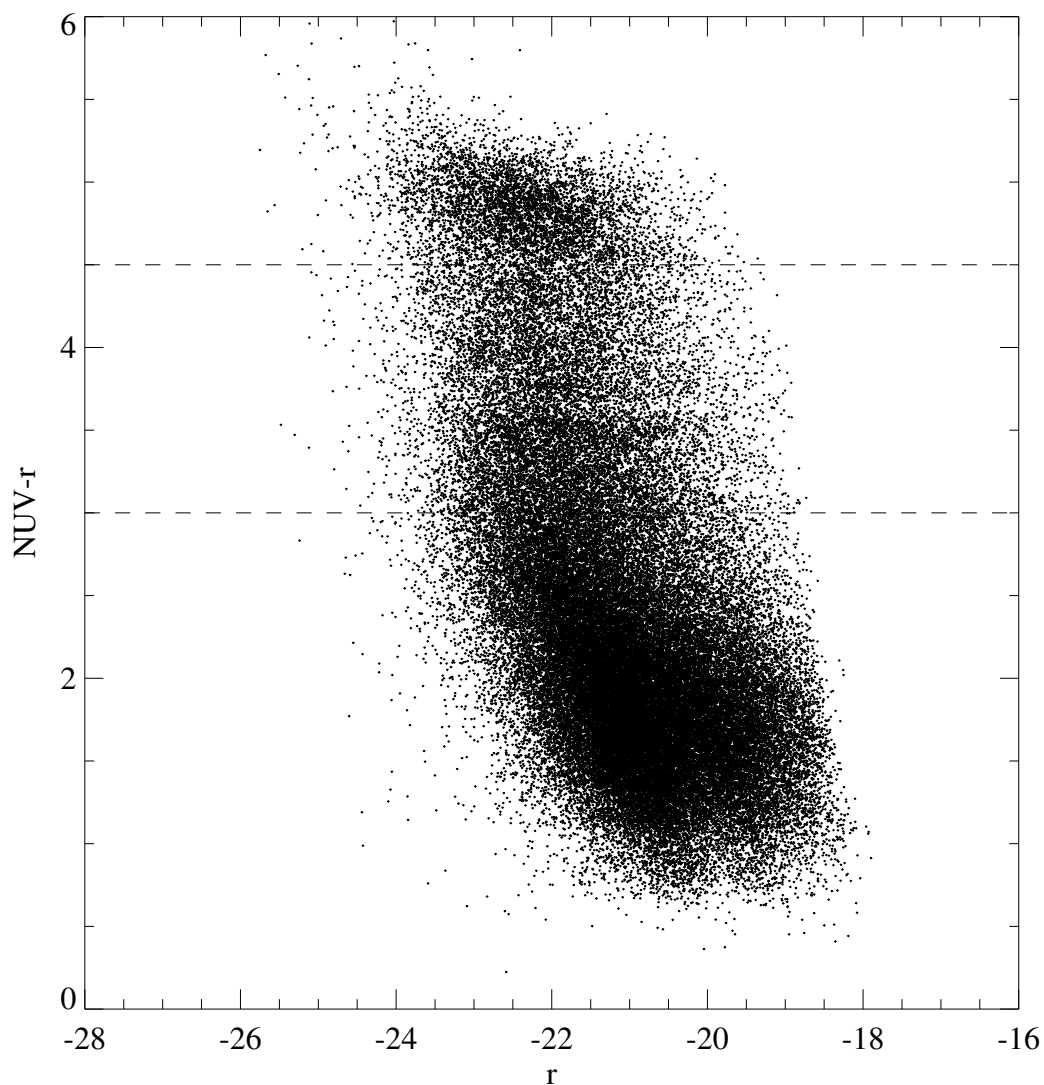
Figure 4.3: Color-magnitude diagram of all CFHTLS sources between 0.55<z<0.9. Two distinct populations are easily distinguishable, with the "green valley" in-between. The dashed lines indicate the color selection criterion used in this work.
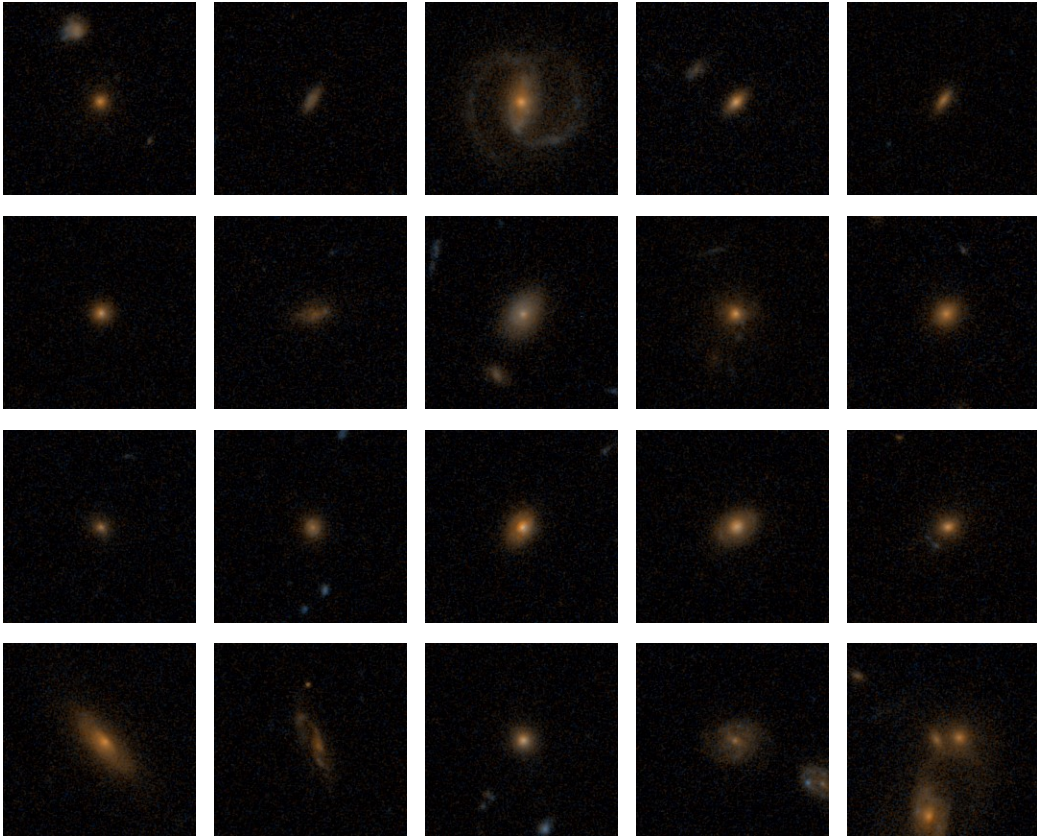
Figure 4.4: ACS $V + I$ images of a subsample of the green valley galaxies observed in this work. Images are 7.5" x 7.5". A fraction of the galaxies are apparently dusty star-forming disks.

4.3.2 Observations and data reduction

Our observations were undertaken with the DEIMOS instrument on the Keck II telescope (Faber, 2003). DEIMOS is a multi-object optical spectrograph, which allows up to nearly 100 objects per mask in a field of view of 16.7 arcmin x 5.0 arcmin. The number of GV galaxies per mask oscillated between 20–30 obj/mask; other galaxies in the aforementioned surveys were then used to complement observations. We used the 1200 mm^{-1} grating for a resolution of $R \sim 5000$. A grating angle centered on 7500 Å was chosen in order to cover all the necessary wavelength range needed to measure $D_n(4000)$ and $H_{\delta,A}$ at the redshift range of our sample. In preparing the masks, preference was given to objects in the extinction-corrected green valley (Section 4.3.4).

In order to achieve required signal-to-noise (S/N) levels, we exposed for a total of up to 9 hours per mask, weather and sky availability permitting, for a median $S/N \simeq 3$ per pixel ($S/N \simeq 2$ for galaxies fainter than $r > 23$). This comprises the deepest spectra of intermediate redshift green valley galaxies taken to date. The observations are summarized in Table 4.1.

Preliminary data reduction was performed with the DEEP2 pipeline.[2] The pipeline is currently optimized for measuring redshifts in galaxies observed with the DEEP survey; therefore, we have used it to select individual spectra, rectify slits and subtract the sky background. Extraction to one-dimensional spectra, refinement of the wavelength solution through the use of sky lines and further data analysis have been done with custom IDL procedures. All redshifts have been remeasured to ensure correct wavelengths for measuring $D_n(4000)$ and $H_{\delta,A}$.

When measuring $D_n(4000)$ and $H_{\delta,A}$ values for individual galaxies, we have interpolated the spectra so that the wavelength resolution per pixel is the same as the Bruzual & Charlot (2003) models, i.e., 1 Å. In all cases we mask out regions contaminated by sky lines. We show the resulting spectra in Figure 4.5.

---

[2]The pipeline is available at http://deep.berkeley.edu/spec2d/
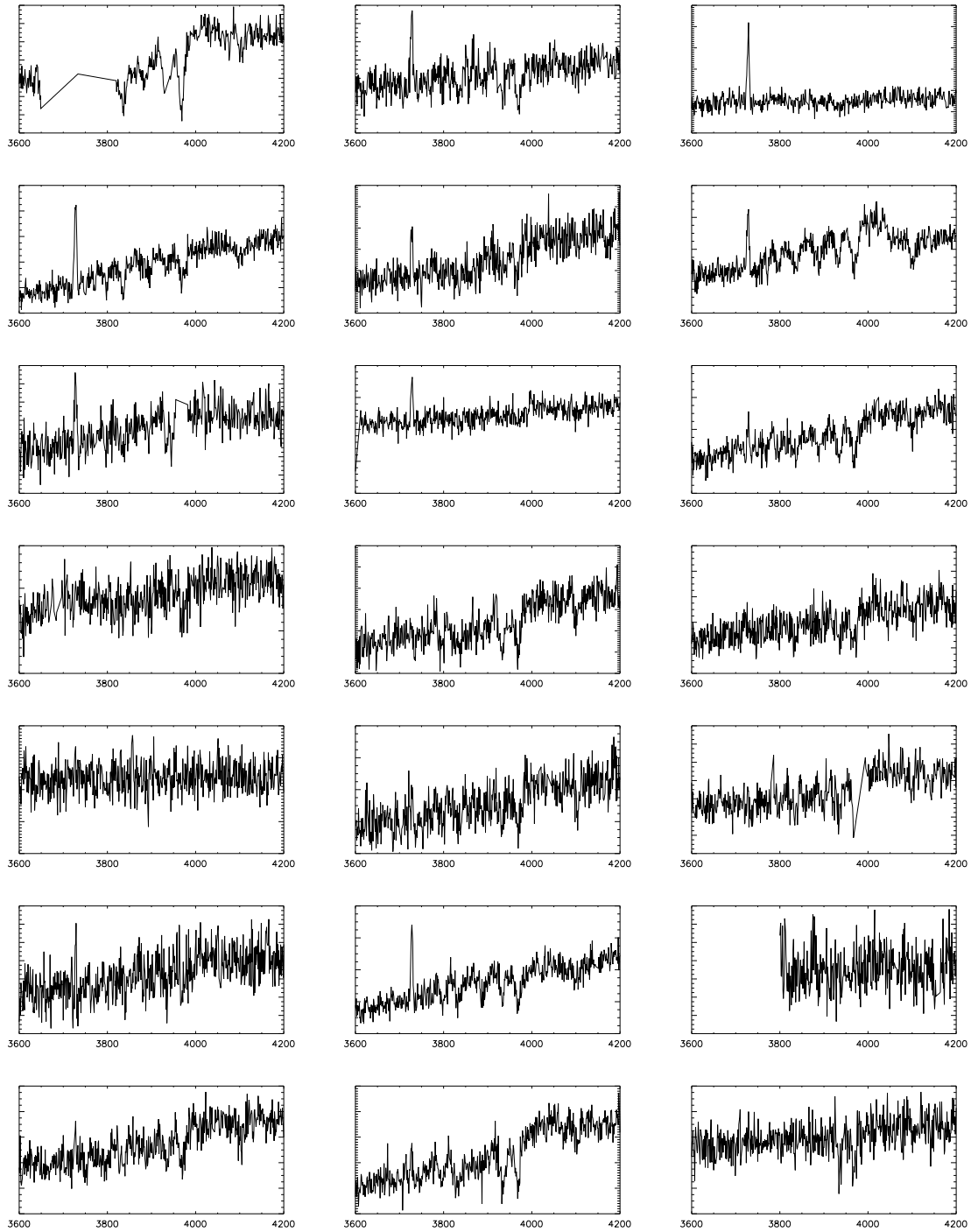
Figure 4.5: Spectra of all green valley galaxies plotted in the region of interest (between $3600\mathring{A} < \lambda < 4200\mathring{A}$). Spectra have been interpolated to match the model resolution of 1 Å per pixel.
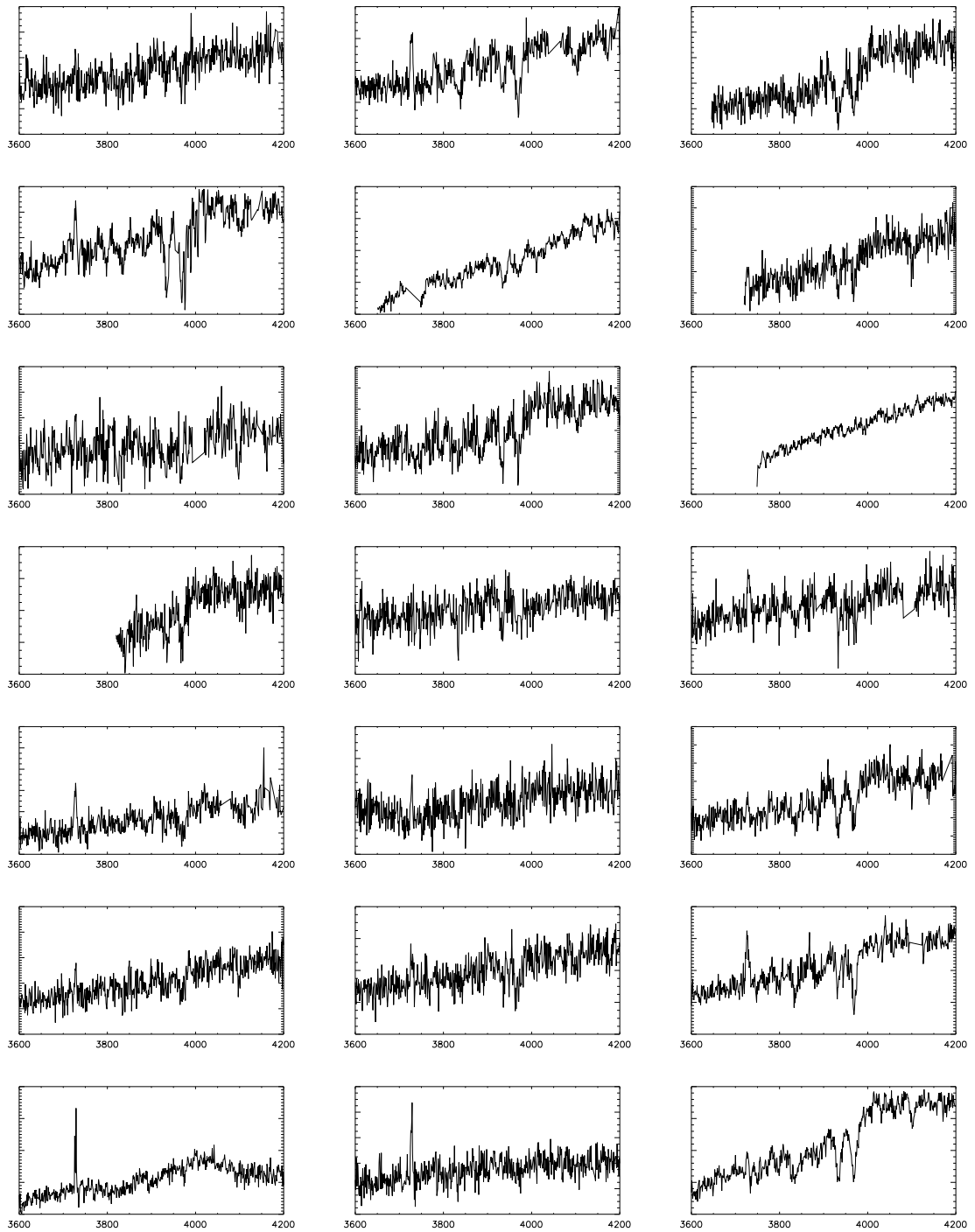
Figure 4.5: Continued.
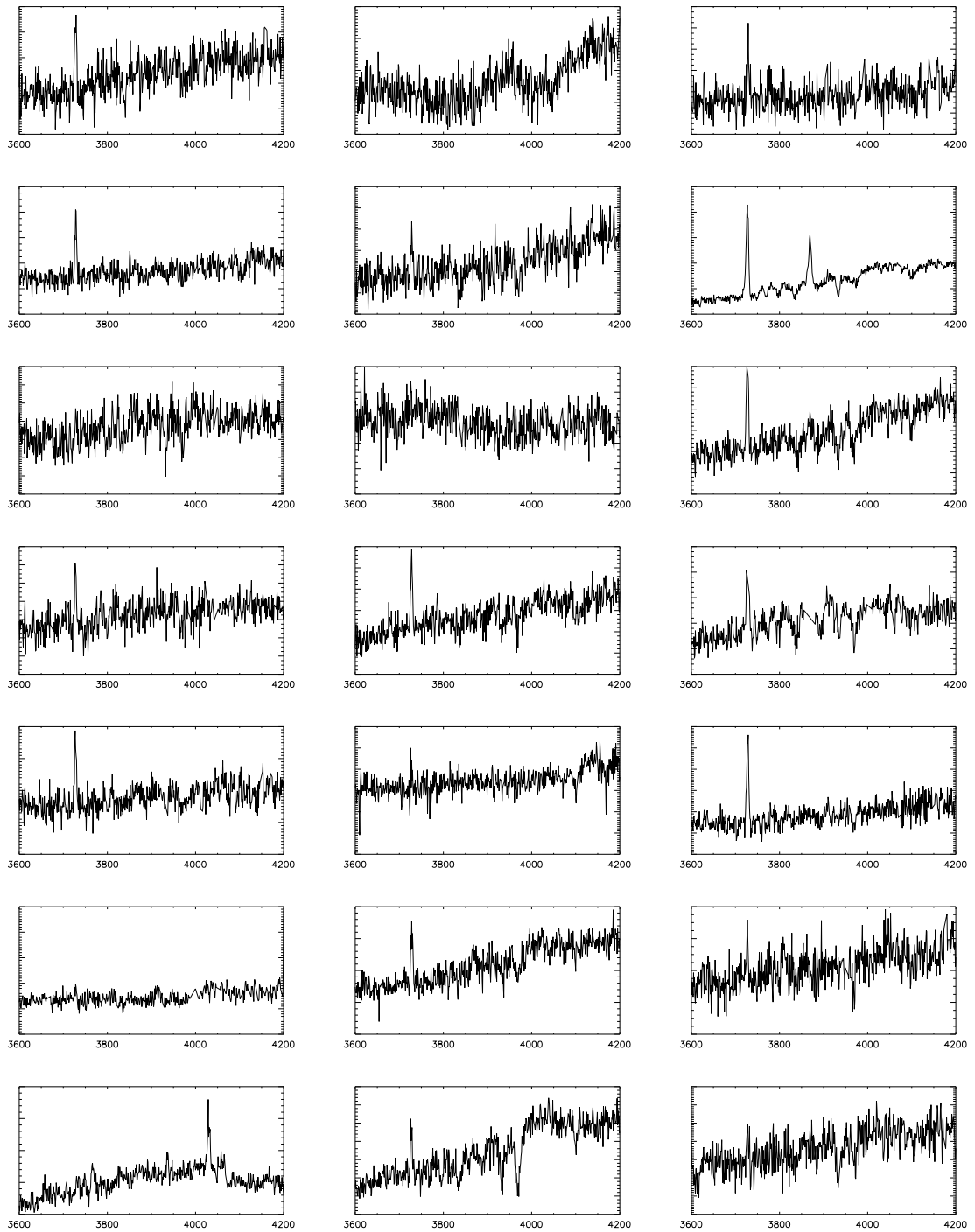
Figure 4.5: Continued.
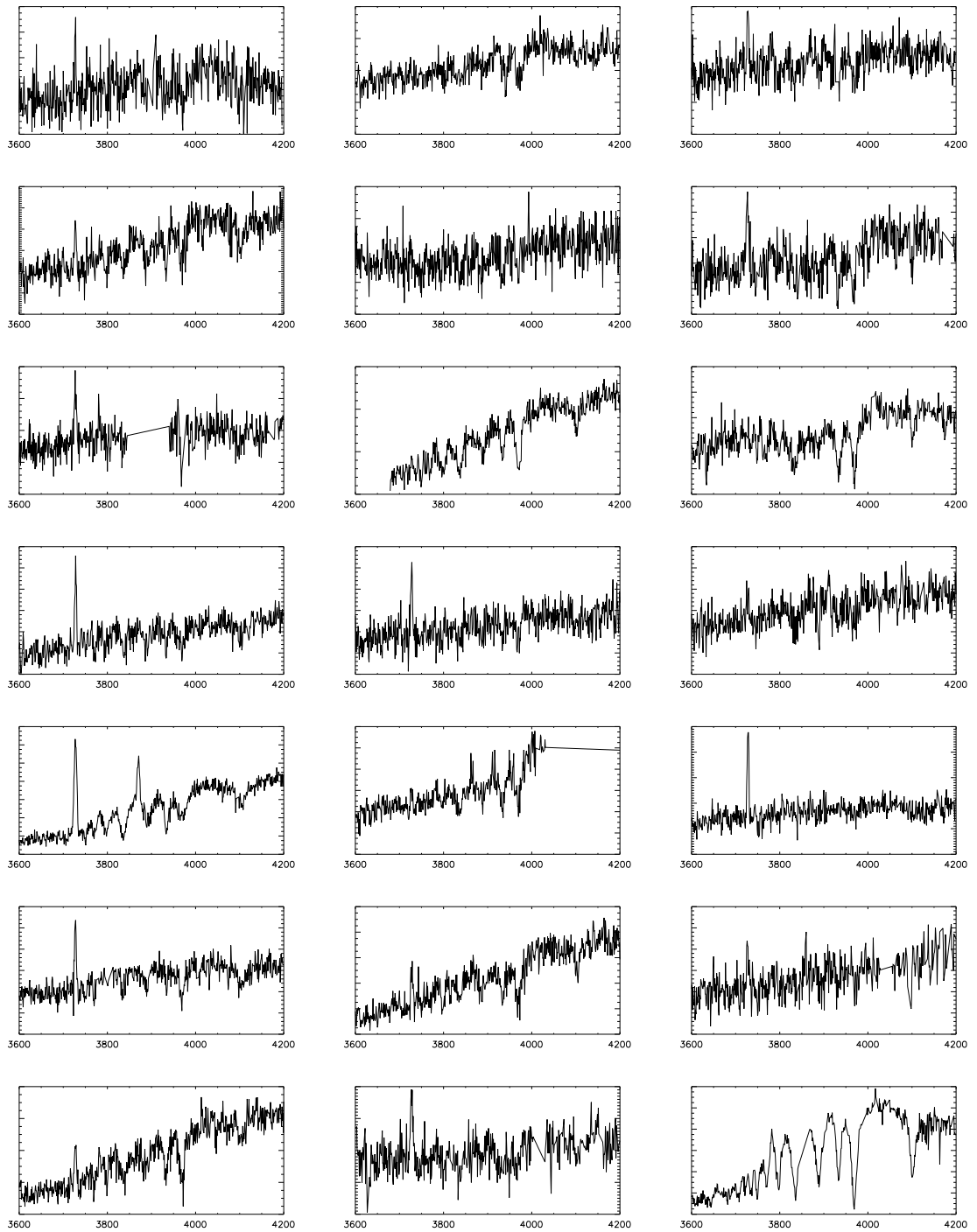
Figure 4.5: Continued.
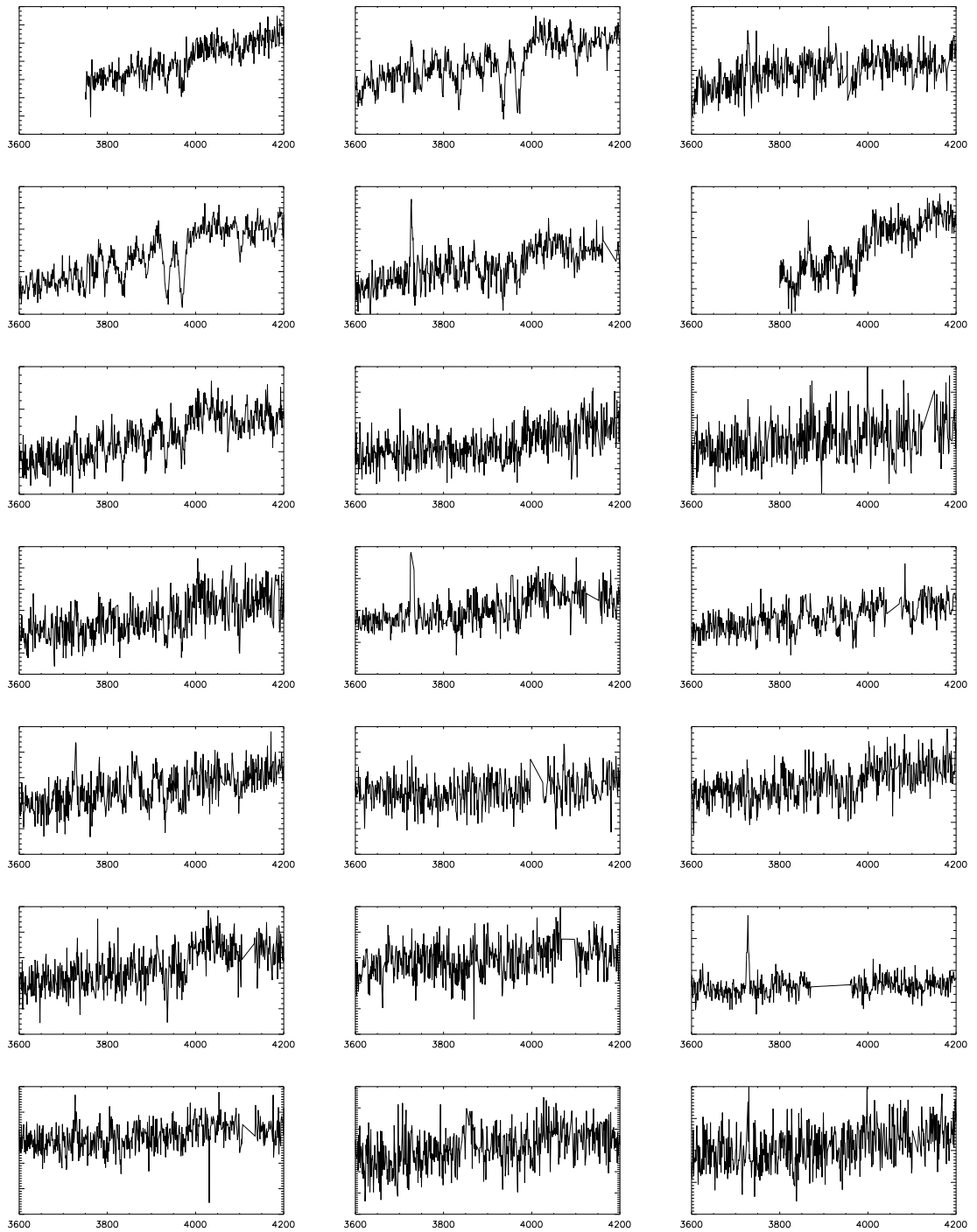
Figure 4.5: Continued.

Table 4.1: Summary of DEIMOS observations

Mask	Field	Observing date (UT)	Total integration time	Number of GV galaxies
AG0801	EGS	May 2008	32400	45
AG0802	EGS	May 2008	18000	43
AG0803	EGS	May 2008	25200	48
DZLE01	DEEP2 Field 2	May 2008	3600	18
D401	CFHTLS D4	August 2008	16200	37
XMM02	XMM-LSS	August 2008	7200	42
AG0901	EGS	April 2009	28800	33
AG0902	EGS	April 2009	28800	30

4.3.3   Number densities and the luminosity funcion

In order to determine the number density per bin in the color-magnitude diagram, we have used only CFHTLS photometric data, including photometric redshifts. These redshifts are precise enough for this exercise, and the increase in sample size and area greatly improves the statistics. Furthermore, since the CFHTLS includes four different fields in distinct regions of the sky (D1, D2, D3, D4), the influence of cosmic variance is minimized.

In determining number densities, we have used the V_{max} method. This takes into account the magnitude limits of the survey and the potential of missing low-luminosity galaxies. In that sense, we perform a k-correction of every source in the survey between the limiting redshifts ($0.55 < z < 0.9$) to determine the maximum distance at which we would be able to detect it (below the $z = 0.9$ cutoff), taking into account all five bands used to select sources. We denote the maximum redshift as

$$z_{\mathrm{max}} = \min(z_{\mathrm{CFHTLS,max}}, 0.9). \qquad (4.5)$$

z_{min} is simply 0.55, since there is no brightest magnitude cutoff. The maximum volume for each galaxy will be

$$V_{\max} = \frac{A}{3} \left(\frac{\pi}{180} \right)^2 \left(\frac{D_L(z_{\max})^3}{(1 + z_{\max})^3} - \frac{D_L(z_{\min})^3}{(1 + z_{\min})^3} \right), \tag{4.6}$$

where A is the angular area in the sky in square degrees occupied by the four fields of the survey and $D_L(z)$ is the luminosity distance to redshift z.

Finally, the number density in the color-magnitude diagram is

$$\Phi(M_r, y) = \frac{1}{\Delta M_r \Delta y} \sum \frac{1}{V_{\max}}, \tag{4.7}$$

in units of $\text{Mpc}^{-3} \text{ mag}^{-2}$, where ΔM_r and Δy are the color and magnitude bin size, respectively. We show our results in Figure 4.6. Two regions of higher number density stand out, evidence of the color bimodality still present at these higher redshifts, similar to the results of Willmer et al. (2006). However, a comparison with similar work at redshift $z \sim 0.1$ (Wyder et al., 2007) shows that the number densities in the red sequence are smaller, showing there has been a significant growth since $z \sim 1$ (Faber et al., 2007). We discuss this in more detail in Section 4.5.

We generate luminosity functions by multiplying the number densities by the color bin size Δy. In Figure 4.7, we show the resulting luminosity functions for three different color bins ($\text{NUV} - r = 1.75, 3.75, 4.75$), and compare those with the same functions at $z = 0.1$, from Wyder et al. (2007). We see that (1) green valley and red sequence number densities are smaller than in the local universe, while number densities are similar for the blue sequence, and (2) all luminosity functions are shifted towards higher luminosities – a fact that has been extensively observed at high redshift and has been cited numerously as evidence for another mode of downsizing (e.g., Bell et al., 2004; Bundy et al., 2006; Faber et al., 2007). In Table 4.2 we present the resulting parameters from a Schechter function fit in each case, as well as the low-redshift values presented in Wyder et al. (2007). The luminosity function is described as follows:

$$\Phi(M) = 0.4 \ln(10) \Phi^* 10^{-0.4(M - M^*)(\alpha + 1)} \exp[-10^{-0.4(M - M^*)}], \tag{4.8}$$
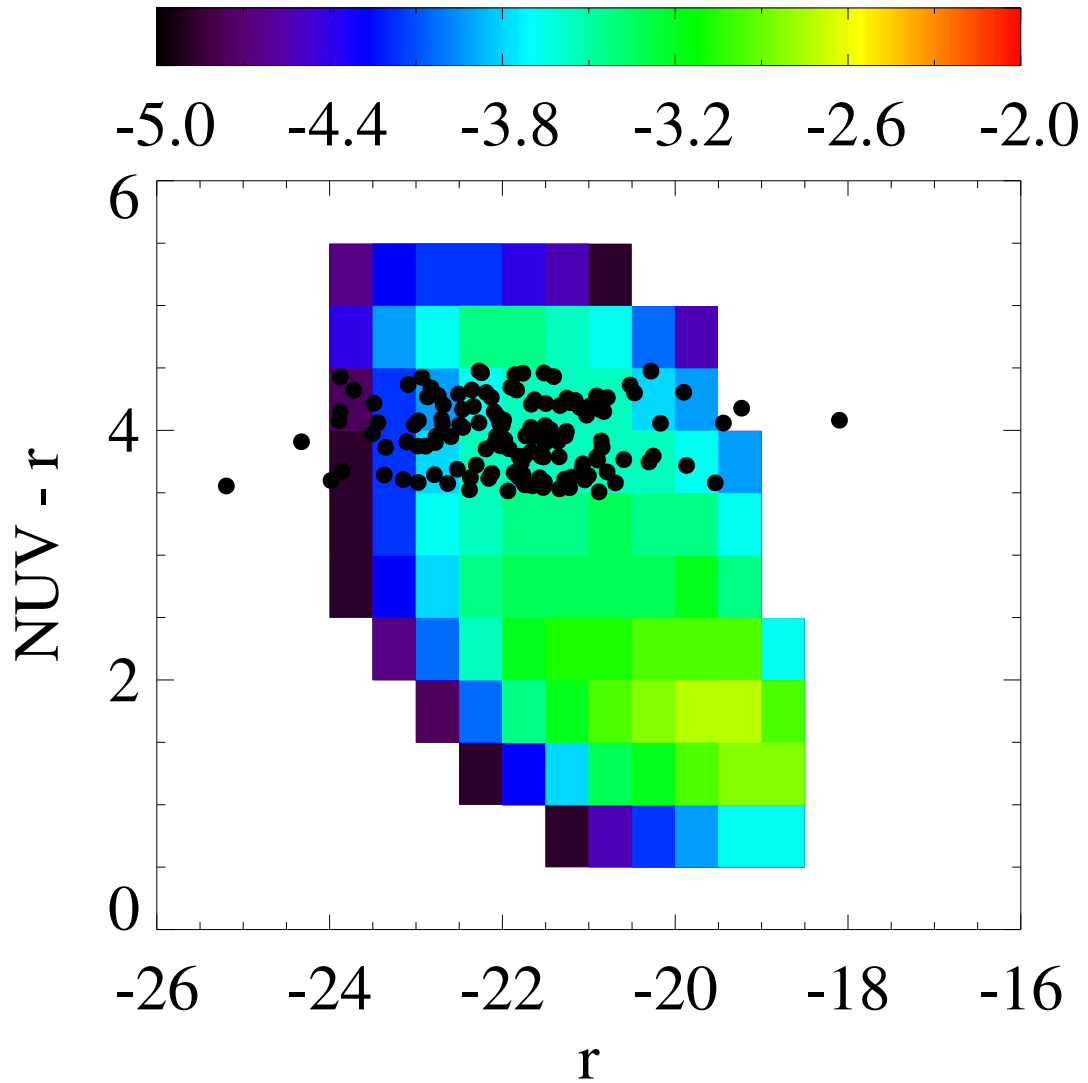
Figure 4.6: Diagram of number density of galaxies in each two-dimensional bin in the color-magnitude diagram, in $\#/\mathrm{Mpc}^{-3}$. Two populations are distinguishable: the red sequence at $\mathrm{NUV} - r \sim 5$ and the blue sequence at $\mathrm{NUV} - r \sim 2$. Green valley galaxies used in this study (black points) fall in-between these two populations, at $3.5 < \mathrm{NUV} - r < 4.5$.

Table 4.2: Schechter function parameters

Sample	Φ^* (Mpc^{-3} Mag^{-1})	M_*	α
Blue sequence (NUV $- r = 1.75$)	-2.465	-20.497	-0.401
Red sequence (NUV $- r = 4.75$)	-3.173	-21.874	0.433
Green valley (NUV $- r = 3.75$)	-3.256	-22.165	-0.365
Blue sequence ($z = 0.1$)	-2.871	-20.331	-1.465
Red sequence ($z = 0.1$)	-2.962	-20.874	-0.579
Green valley ($z = 0.1$)	-2.775	-20.711	-0.357

where M^*, Φ^* and α are the free parameters in the fit.

4.3.4 Extinction correction

Extinction correction is of fundamental importance in determining the green valley. This is mainly due to contamination by heavily obscured star-forming galaxies. This is already an important problem at $z \sim 0$, but we expect it to be worse at higher redshifts, since the number density of LIRGs and ULIRGs is expected to increase towards earlier times. To illustrate the issue, we show in Figure 4.8 the fraction of 24 μm detected galaxies in the Groth Strip per two-dimensional bin in the color magnitude diagram (for a description of the dataset, see Davis et al., 2007). We can see that most of the green valley galaxies on the bright end are actually 24 μm sources, indicative of dusty star-forming galaxies, instead of the quenching objects for which we are searching.

In an attempt to decrease contamination from such galaxies, we used an independent SED fitting result for a number of galaxies in the Extended Groth Strip (Salim et al., 2009), where extinction is a free parameter. This sample of ~ 6000 objects was then used to calculate the number densities in the color-magnitude diagram the same way as described in Section 4.3.3. The result can be found in Figure 4.9. The main difference when comparing this diagram with Figure 4.6 is a decrease in number density in the green valley and a clearer distinction between the blue and red sequences, as expected.
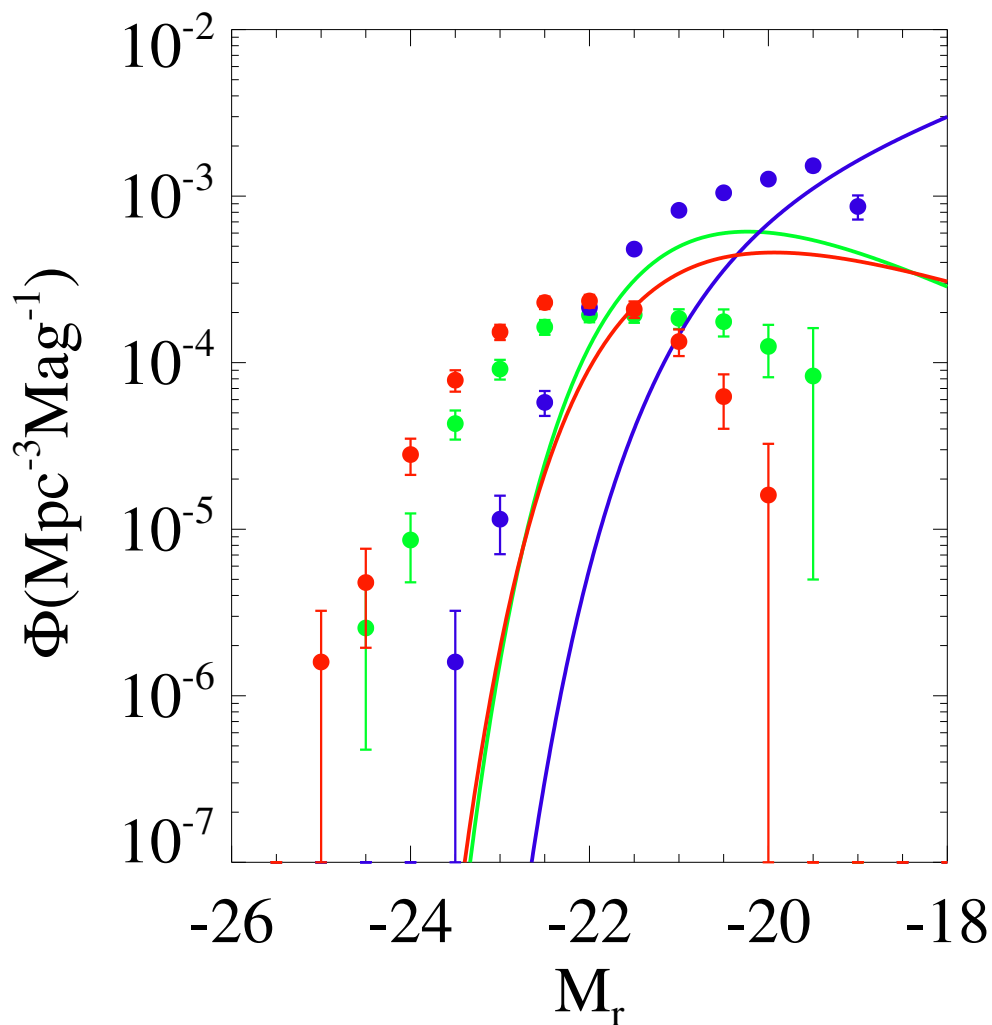
Figure 4.7: Luminosity functions at $z \sim 0.8$ measured from the CFHTLS Deep survey. Blue represents the blue sequence (NUV $-r = 1.75$), red, the red sequence(NUV $-r = 4.75$), and green, the green valley (NUV $-r = 3.75$). The solid lines indicate luminosity functions measured at $z = 0.1$ by Wyder et al. (2007), for comparison. All functions at higher redshift are shifted towards brighter magnitudes. The blue sequence shows similar number densities, while red and green galaxies are rarer than in the local universe.
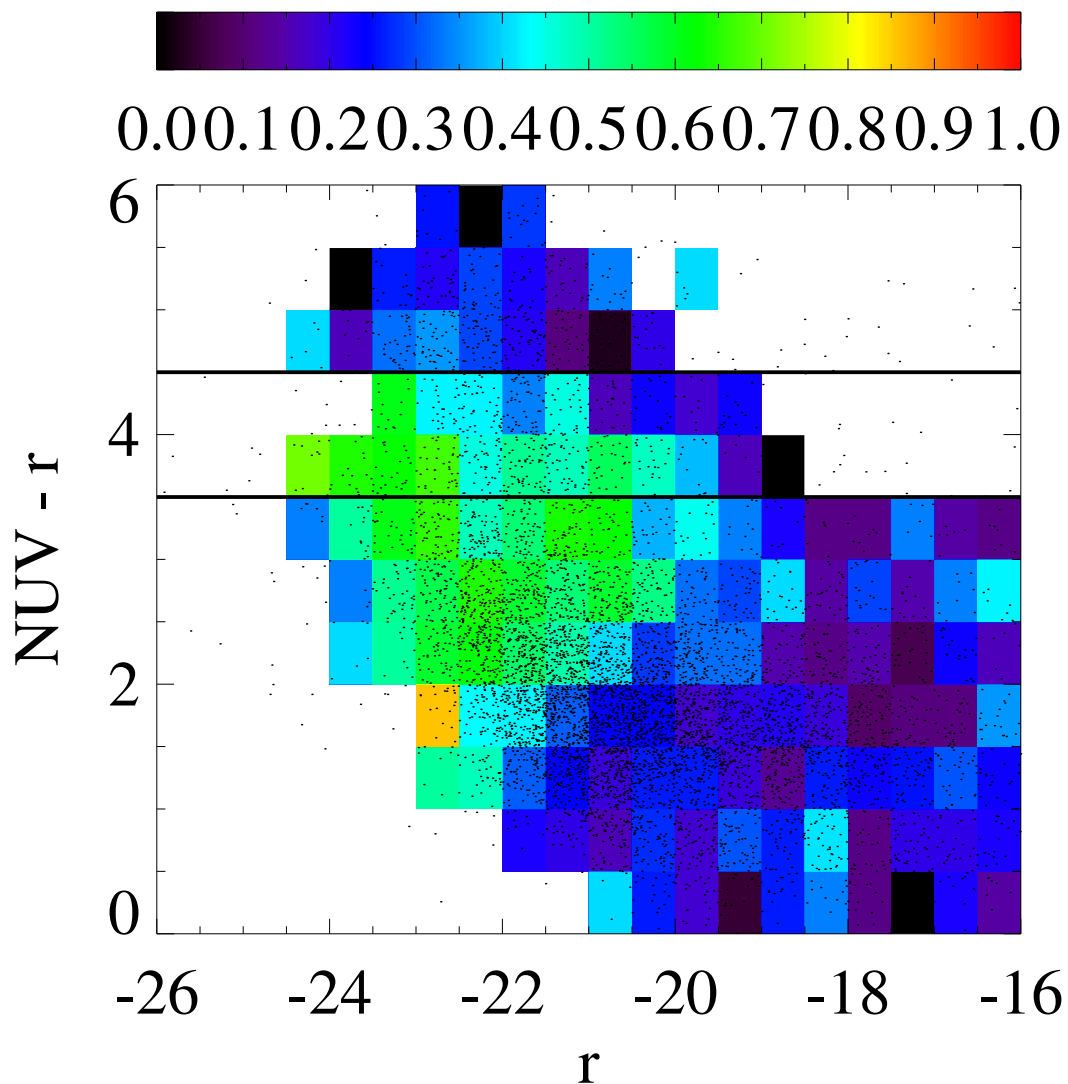
Figure 4.8: Fraction of 24 μm detections as a function of color and magnitude. We overplot all k-corrected AEGIS sources as black points. The thick horizontal lines indicate the region of the color-magnitude diagram defined as the green valley in this work. Up to 65% of the green valley galaxies in a given bin are probably dusty starbursts, and not galaxies in the process of quenching star formation.
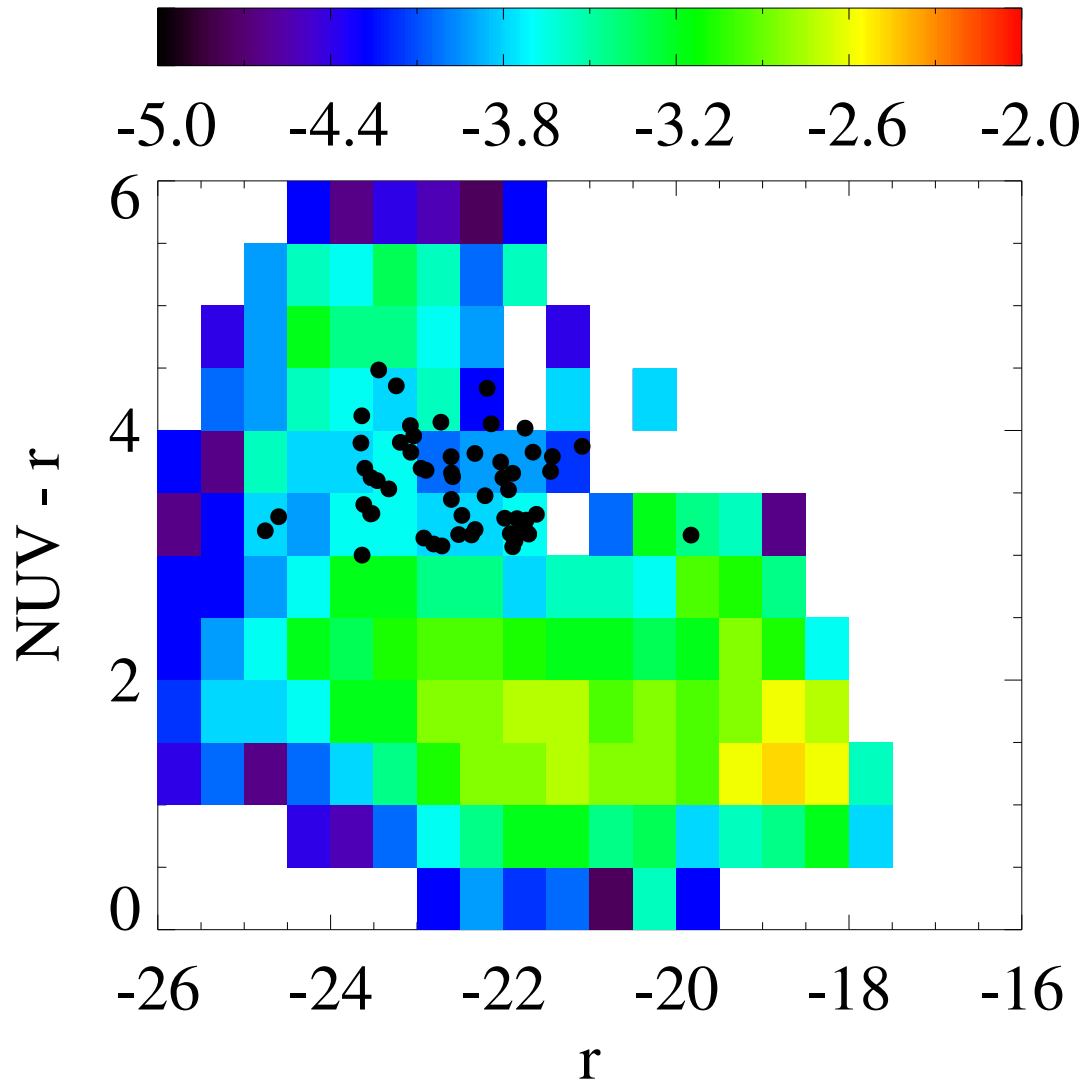
Figure 4.9: Same as Figure 4.6, after applying extinction correction of absolute magnitudes (see Section 4.3.4).

In Figure 4.10 we show again HST image stamps of the galaxies as in Figure 4.4, but now we include only galaxies in the extinction-corrected green valley. It is important to notice that there are still some objects that resemble dusty star-forming disks. Whether those are objects that are evolving passively into the red sequence, spirals with a recent starburst event or simply the result of extinction measurement errors is still unclear. We discuss these possibilites in Section 4.5.2.

4.4   Results

We have measured $D_n(4000)$ and $H_{\delta,A}$ indices for all green valley galaxies observed. A number of galaxies presented unrealistic values – outside the expected range of $1.0 < D_n(4000) < 2.0$ and $-4.0 < H_{\delta,A} < 8.0$. The spectra for most of these objects show very low signal-to-noise, placed in the masks that were observed for the shortest times. Excluding these, we are left with 105 green valley galaxies. These objects are shown in Figure 4.11, along with the models presented in Figure 4.1. The observed values agree well with the models, following the trend of lower $H_{\delta,A}$ values for higher $D_n(4000)$.

In selecting galaxies for the extinction-corrected green valley, our sample was reduced, due to smaller number densities and only a fraction (approximately 50%) of galaxies in DEEP2 (and no galaxies in the remaining CFHTLS fields) having reliable SED extinction measurements. For this reason, we have increased the color selection to include $3.0 < (\mathrm{NUV} - r)_{\mathrm{ext}} < 4.5$ colors, in an attempt to improve our statistics. These objects are highlighted in Figure 4.11 as red symbols.

Figure 4.11 also shows the $D_n(4000)$ and $H_{\delta,A}$ values for models of green valley galaxies defined at $\mathrm{NUV} - r = 4.0$, the median color value of our green valley sample. The straight diagonal lines indicate equidistant lines from two adjacent models, in which distance is defined by normalizing the $H_{\delta,A}$ index as $H_{\delta,An} = H_{\delta,A}/12$ to reflect the expected dynamic range in that measurement.

In Figure 4.12 we compare the quenching timescales we find with the obtained values at $z = 0.1$ in Paper I, showing the fraction of galaxies in each γ bin as defined
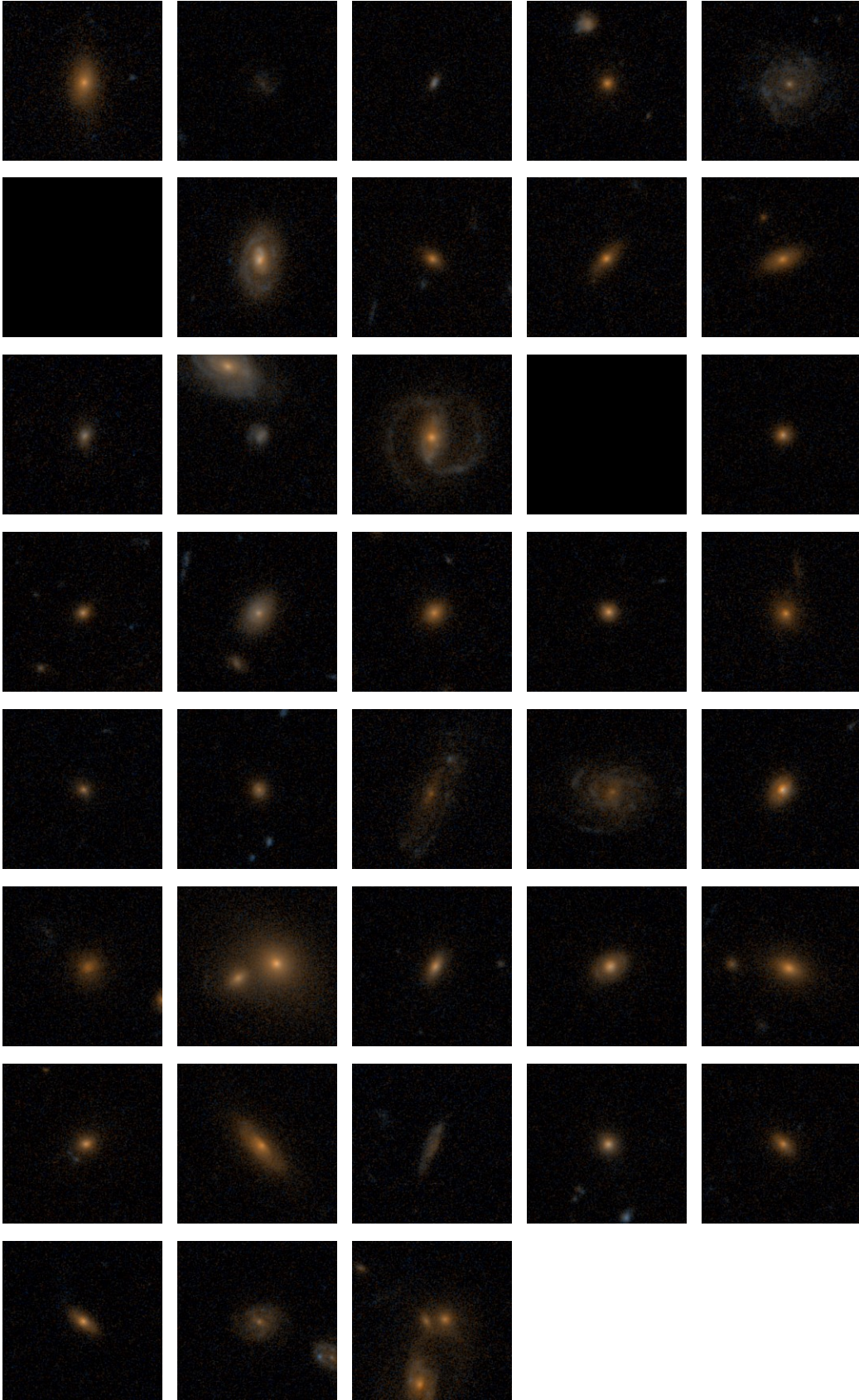
Figure 4.10: Same as Figure 4.4, but for the extinction-corrected green valley. Most galaxies are small spheroids, but a fraction still appear to be dusty disks.
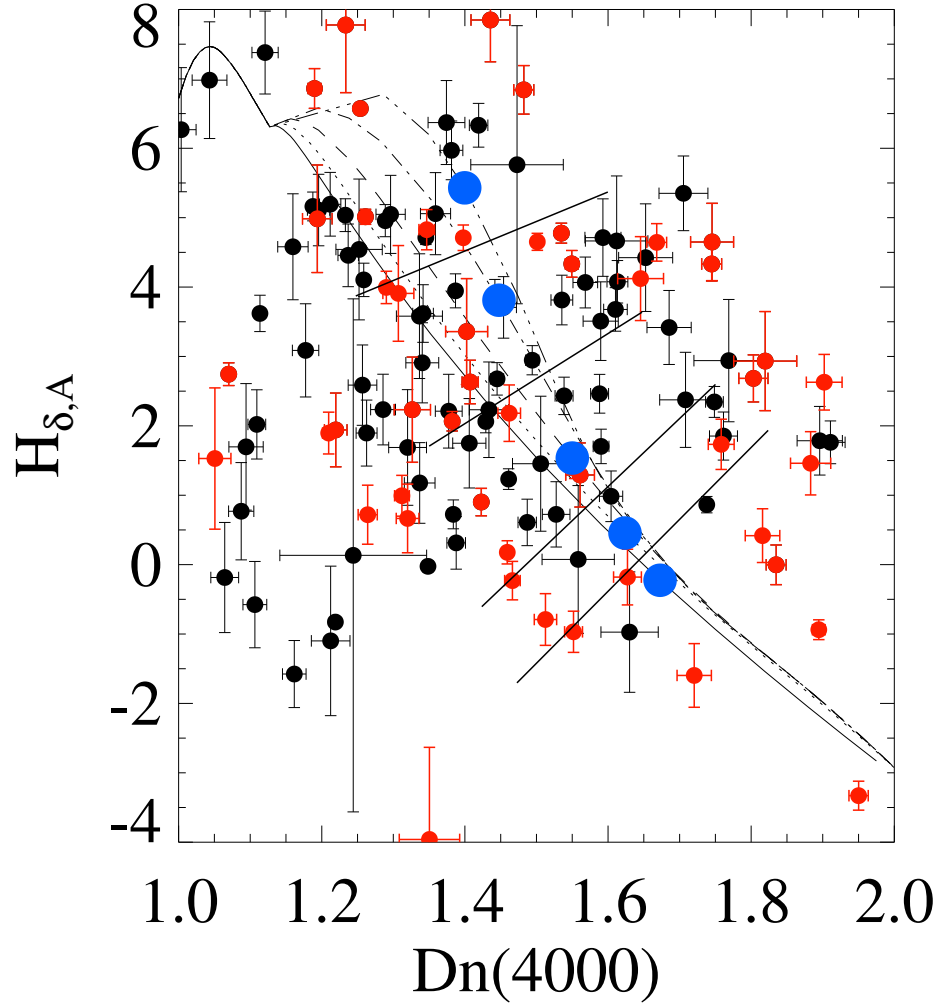
Figure 4.11: $D_n(4000)$ and $H_{\delta,A}$ indices of green valley galaxies with error bars. The different lines on the plot indicate the expected values from models with varying γ values, as in Figure 4.1. Black points are all galaxies that fall in the green valley region, prior to making a correction for extinction in the selection. Red symbols indicate galaxies in the green valley after extinction correction is applied. Big blue circles indicate the moment at which models present $NUV - r = 4.0$ colors, with diagonal straight lines representing equidistance from consecutive models.

by the dividing lines in Figure 4.11. Since γ correlates with quenching speed, that means galaxies with higher γ values will spend less time in the green valley, and are less likely to be observed. We show the fractions corrected for this (weighted by dy/dt) as dashed lines. We represent the data in this work as circles, and the values for low redshift as triangles. The main conclusion we draw from this exercise is that quenching timescales are shorter at higher redshift, since the amount of galaxies with higher γ is increased. In quantitative terms, this represents a factor 2–3 decrease in typical transitioning timescales.

We determined average $D_n(4000)$ and $H_{\delta,A}$ values for each magnitude bin by averaging over all galaxies in a given bin, weighted by the error in each case. This yields an average γ in each bin, which in turn corresponds to a period of time required to cross over the color range covered by the green valley. We combine median galaxy masses for each bin, as determined by from K-band measurements by Bundy et al. (2007), and number densities to calculate a mass flux for each given magnitude. We show these values in Table 4.3. We repeat the procedure in the case of the extinction-corrected green valley galaxies, and show the results in Table 4.4.

Finally, the total mass flux density is the sum of the mass flux through all magnitudes. We show the results in Figure 4.13. The upper circle represents the value before extinction correction ($\log \dot{\rho} = -0.36 \pm 0.08$ M$_\odot$ yr^{-1} Mpc^{-3}), while the bottom value represents the mass flux while accounting for extinction correction ($\log \dot{\rho}_{\text{ext}} = -0.80 \pm 0.51$ M$_\odot$ yr^{-1} Mpc^{-3}). The error bars represent the redshift range covered by our sample.

The first thing to notice is the difference (about a factor of 3) between both measurements. This can be attributed to a combination of factors: on one hand, measured number densities are smaller when correction for extinction is applied (section 4.3.4); on the other hand, the contamination of star-forming galaxies also biases our sample to higher $< D_n(4000) >$, $< H_{\delta,A} >$ values, which in turn represent higher γ's and shorter evolution timescales.

We compare our values to those found in Paper I at $z = 0.1$; the top triangle in Figure 4.13 represents the flux without taking into account dust extinction, and
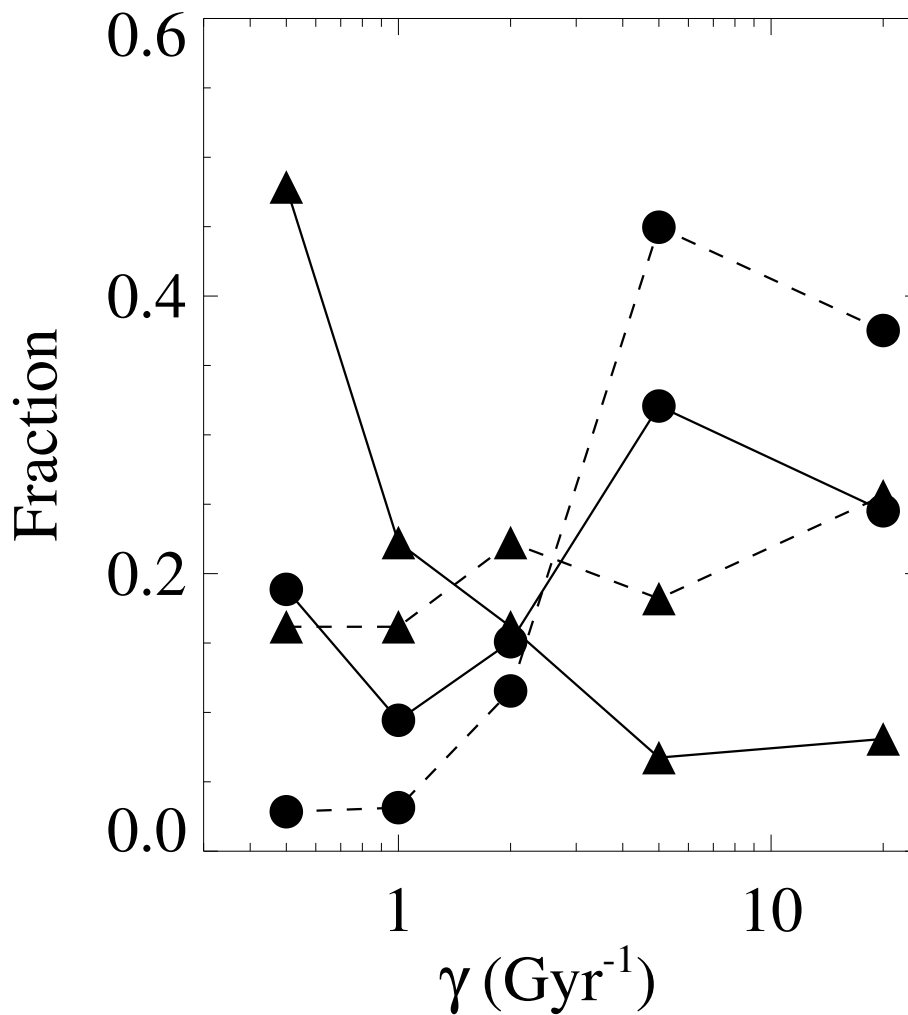
Figure 4.12: Fraction of green valley galaxies as a function of γ bins, as shown in Figure 4.11. All values shown here are for extinction corrected samples; circles represent our sample, while the triangles are the values found at redshift $z \sim 0.1$ in Paper I. The dashed lines in both cases are weighted by dy/dt to correct for the fact that galaxies that are quenching faster are less likely to be observed. We notice an evolution in the fraction of high-γ values, in that at higher redshift the timescales for star formation quenching were shorter.

Table 4.3: Mass flux results

M_r	$\log \Phi$ (Mpc^{-3})	$< \log M_* >$ M$_\odot$	$< D_n(4000) >$	$< H_{\delta,A} >$	$< \gamma >$	$\dot{\rho}$ (10^{-3} M$_\odot$ yr^{-1} Mpc^{-3})
-24.25	-5.32 ± 0.59	11.3	1.54	2.43	3.05	2.0±2.7
-23.75	-4.72 ± 0.30	11.3	1.21	-1.10	2.35	8.1±5.5
-23.25	-4.08 ± 0.14	11.2	1.24	-0.41	2.60	30.0±9.8
-22.75	-3.75 ± 0.10	11.1	1.26	1.98	6.10	87.5±19.5
-22.25	-3.51 ± 0.07	11.0	1.32	2.61	6.95	99.8±17.1
-21.75	-3.45 ± 0.07	10.9	1.30	4.18	12.80	93.4±15.1
-21.25	-3.41 ± 0.08	10.7	1.32	4.43	13.39	65.9±11.7
-20.75	-3.44 ± 0.10	10.5	1.37	0.64	2.63	25.0±5.9
-20.25	-3.59 ± 0.15	10.2	1.33	4.18	12.32	17.7±6.3
-19.75	-3.71 ± 0.30	10.1	N/A	N/A	N/A	N/A
-19.25	-4.08 ± 0.94	10.0	1.37	6.37	20.63	2.9±6.2

Table 4.4: Mass flux results (corrected for extinction)

M_r	$\log \Phi$ (Mpc^{-3})	$<\log M_*>$ M$_\odot$	$<D_n(4000)>$	$<H_{\delta,A}>$	$<\gamma>$	$\dot{\rho}$ (10^{-3} M$_\odot$ yr^{-1} Mpc^{-3})
-24.75	-3.91 ± 0.57	11.1	1.71	2.37	1.68	26.8±35.4
-24.25	-3.83 ± 0.37	11.1	N/A	N/A	N/A	N/A
-23.75	-3.93 ± 0.34	11.1	1.45	1.73	2.98	32.3±25.3
-23.25	-3.92 ± 0.35	11.1	1.18	-1.11	2.47	31.1±24.9
-22.75	-3.92 ± 0.49	10.9	1.33	2.43	6.17	37.3±41.9
-22.25	-4.28 ± 0.53	10.8	1.41	1.21	2.80	7.4±8.9
-21.75	-4.09 ± 1.33	10.7	1.35	2.35	5.63	13.3±40.8
-21.25	-4.11 ± 1.02	10.5	1.21	4.64	15.72	9.1±21.3
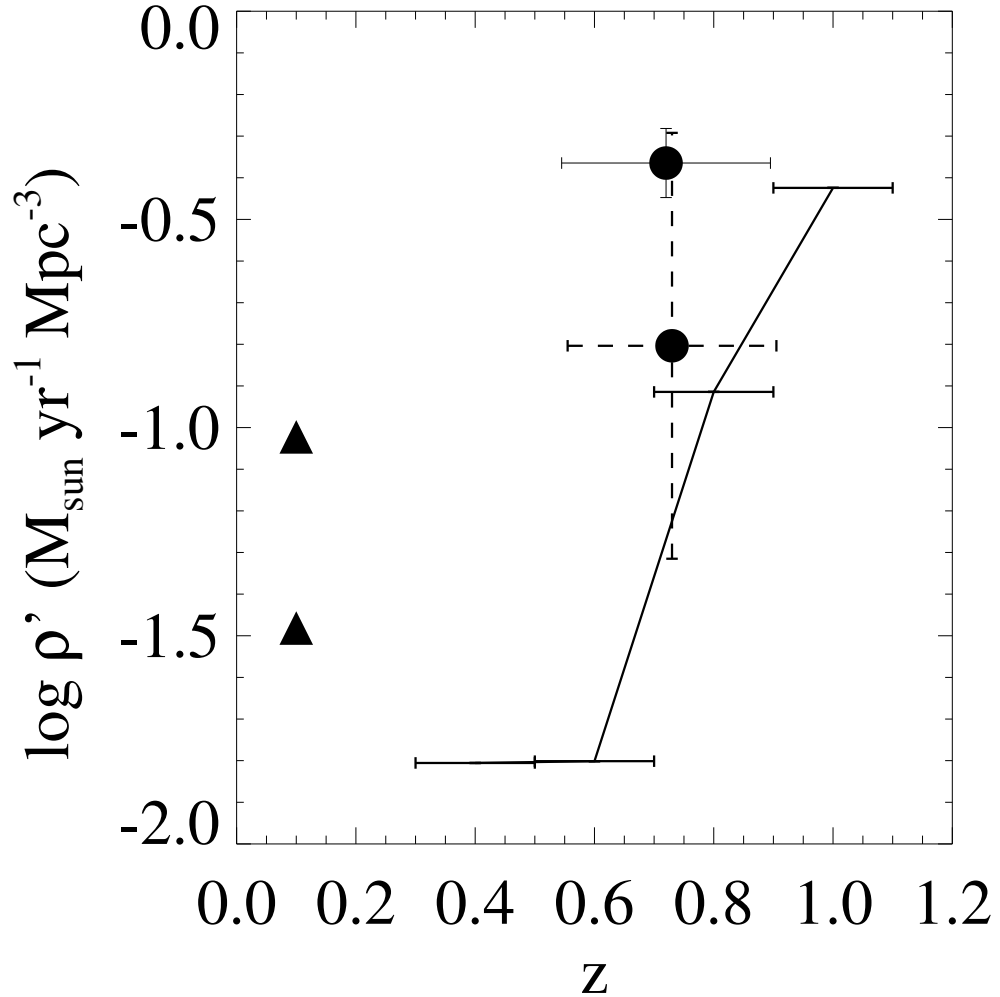
Figure 4.13: Mass flux density in the green valley. The circles represent our data; solid error bars indicate the value calculated without extinction correction, while the symbol with dashed error bars includes extinction correction. Values at $z = 0.1$ calculated in Paper I are shown as triangles, and are determined with (top) and without (bottom) extinction correction. The solid line shows the density growth rate of the red sequence, as determined from Faber et al. (2007). Our data points show a clear increase in the mass flux density across the green valley towards earlier times, in agreement with estimates from the growth of the red sequence.

the bottom one is the extinction-corrected measurement. The evolution with redshift from $z = 0.1$ to 0.8 is evident, with mass flux values at intermediate redshifts being 3 to 5 times higher than those found in the low-redshift universe. This reflects the significant change occurring in galaxy evolution over cosmic time.

In Figure 4.13 we also show the density growth of the red sequence, in units of $M_\odot$ yr^{-1} Mpc^{-3}. This has been calculated as follows: the B-band luminosity density at the local universe has been determined as $j_B = 10^{7.7}$ L$_\odot$ Mpc^{-3} (Bell et al., 2003; Madgwick et al., 2002). The mass-to-light ratio of red sequence galaxies in the B-band, in turn, is estimated at $(M/L_B) = 6$ M$_\odot$/L$_\odot$ (Gebhardt et al., 2003; Faber et al., 2007). Combined with the evolution of the evolution in the number density of galaxies in the red sequence (Faber et al., 2007), we can then calculate the mass flux at each redshift interval as

$$\dot{\rho} = j_B \left(\frac{M}{L_B}\right) \left(\frac{10^{\Delta \log \Phi_0} - 1}{10^{\Delta \log \Phi_0}}\right) \Delta t(\Delta z), \tag{4.9}$$

where $\Delta \log \Phi_0$ is the logarithmic change in the normalization of the luminosity function at each redshift, and $\Delta t(\Delta z)$ is the change in the age of the universe at each redshift interval.

We find that the mass growth rate was indeed higher by a factor of ~ 5 in the earlier universe, pointing to another manifestation of downsizing in galaxy evolution. Furthermore, our results agree within errors with the estimated growth of the red sequence at $z \sim 0.8$, reinforcing the idea that the mass flux through the green valley occurred more rapidly in the past.

4.5 Discussion

4.5.1 The build-up of the red sequence

In Faber et al. (2007), the authors discuss how the red sequence at $z = 0$ is assembled, from the brightest, most massive objects down to the smallest and faintest. From DEEP2 data out to $z \sim 1$, the authors are able to define the evolution of the lumi-

nosity function and the growth of the luminosity density – for all galaxies and for the blue and red sequences individually – to discuss how galaxies might evolve along the color-magnitude diagram. The authors argue that the red sequence is formed through a combination of star formation quenching in star-forming galaxies and dry mergers, which move galaxies along the red sequence towards the brighter end.

How are the brightest red galaxies formed? One might think that the simple quenching of individual blue galaxies, be it by mergers, AGN activity or any other mechanism, would be sufficient to produce the red sequence. However, the most massive blue galaxies in the local universe are not as massive as the most massive red ones. Even major mergers, which would produce a galaxy up to twice as massive as each individual object, are not enough to explain the observed mass function. In fact, in the morphological study by Mendez et al. (2011) of ~ 300 galaxies in the optically-defined green valley at $0.4 < z < 1.2$, they find that most green galaxies cannot be classified as mergers and that the merger fraction in the green valley is in fact lower than in the blue sequence.

Our data offers an interesting insight into the problem of red galaxy formation. Comparison with the mass flux at low-redshift (Paper I) shows that the mass flux occurred at brighter magnitudes at high redshift (Figure 4.14), indicating the build-up of the most massive end of the red sequence at earlier times, which is in qualitative agreement with the evolution of the luminosity function. This represents a *downsizing* of the green valley evolution, with the red sequence forming "from the top down": in the past, more massive star-forming galaxies were being formed and subsequently quenched, forming the more massive red sequence galaxies. At later times, star formation shifts to less massive galaxies; these are then quenched as well, and the fainter end of the red sequence is created.

However, this is not the complete picture. Faber et al. (2007) call upon dry mergers to explain observed properties of the brightest red galaxies. These mergers correspond to the interaction between two or more red sequence galaxies, with little gas involved. The absence of copious gas diminishes the subsequent burst in star formation that is otherwise expected in wet mergers, between gas-rich galaxies. These dry mergers

hence result in an increase in stellar mass, with no coupled burst in activity. It would be interesting to compare the mass flux density at the very massive end of the color-magnitude diagram to infer whether that is sufficient to create all massive galaxies or if dry mergers are a necessity, but this is currently an impossible task due to large uncertainties and small number statistics (especially at these limiting magnitudes).

The mechanism through which quenching occurs is as yet unclear. As we have seen above, merger activity may not be as relevant; AGN activity is also called upon, and it is indeed found that green valley galaxies show an increase in AGN fraction – although actual correlation with star formation quenching has not been unequivocally shown (Paper I; Nandra et al., 2007; Schawinski et al., 2009, see also discussion in Chapter 1). In a future paper, we plan to investigate this correlation by comparing our results for quenching timescales with different tracers of AGN activity, such as X-ray luminosities and optical emission line ratios.

4.5.2 The star formation history of green valley galaxies

It is important to consider, first, that most of the stellar mass in red sequence galaxies is not formed while the galaxy is in the red sequence (Salim et al., 2005). This lends support to our assumption (1), which states that galaxies are only moving redward in the color-magnitude diagram. However, this is not strictly true; we do know a fraction of elliptical galaxies, even in the local universe, show signs of recent starburst events (Thilker et al., 2010). If we take into account that a fraction of galaxies in the green valley are turning *blue*, instead, then the inferred mass flux would be *smaller*.

At the same time, in Paper I we have argued how our choice of star formation histories influences our results. In general, assuming shorter periods of constant star formation or different models for the time evolution decreases the final calculated value for $\dot{\rho}$. Therefore, we conservatively assume our measured mass flux density as an *upper value* for the actual flux in transition galaxies from the blue to the red sequence. Still, a decrease by 0.5 dex brings us to closer agreement with the inferred growth of the red sequence. At the same time, the difference in final results combined
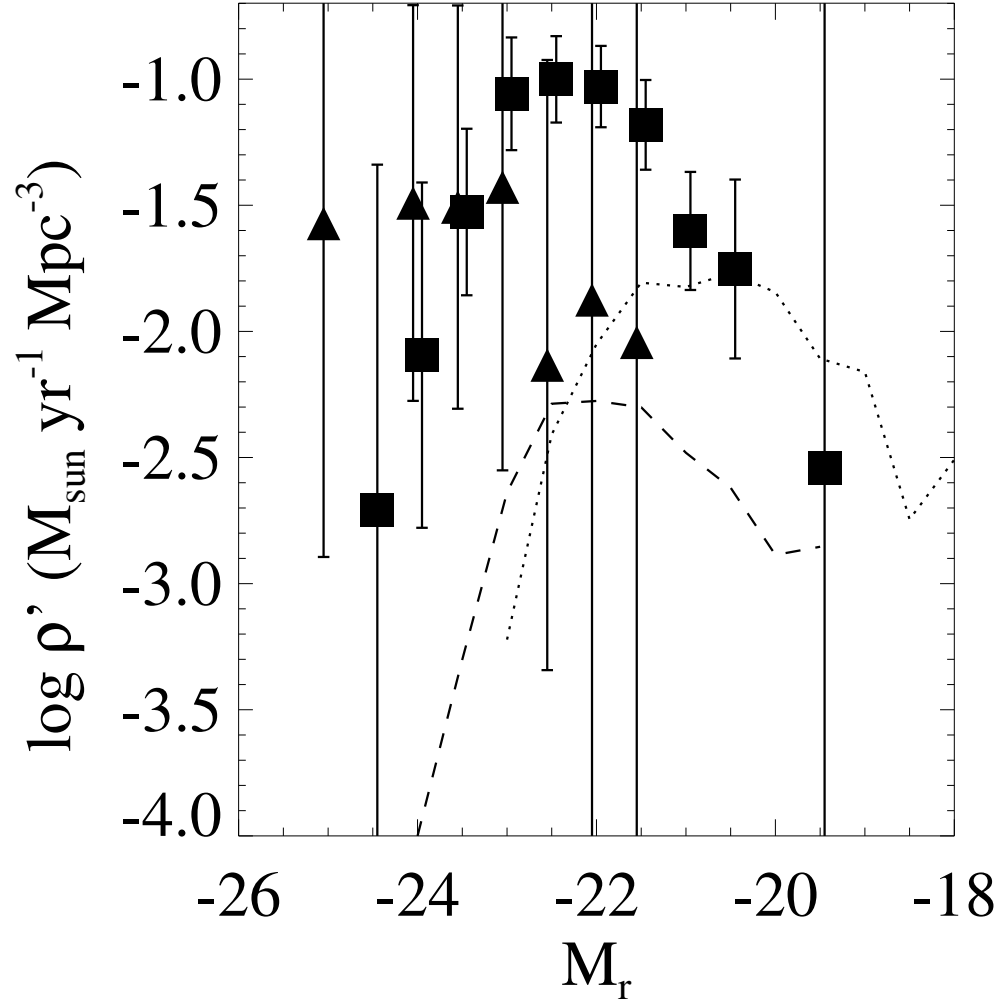
Figure 4.14: Mass flux density as a function of r magnitude. The flux at intermediate redshifts is shown as solid symbols; circles for the extinction-corrected sample, squares, no extinction correction. The lines represents the values found for the local universe in Paper I; the dashed line indicates the extinction corrected sample at $z = 0.1$. In both cases, the peak at high redshift is shifted towards brighter magnitudes by $\gtrsim 1$ mag.

with the observed change in the luminosity function and the distribution of γ values makes it safe to assume the evolution in mass flux density from $z \sim 0.8$ to $z \sim 0.1$ is real.

Finally, one can argue the star formation history assumed in this work is simplistic. It has been even argued that star-forming galaxies follow an inverted τ model, with an exponentially *increasing* star formation history (Maraston et al., 2010). In any case, a more realistic approach to modeling the star formation histories of galaxies could yield different results (likely smaller fluxes, as argued above). Thus, we are currently in the process of producing models that do not rely on *ad hoc* star formation histories, but instead are drawn from cosmological N-body simulations and semi-analytic models, generating more physically motivated star formation histories. We will compare our spectra with these more refined models in a future paper (Martin et al., in prep.).

4.6 Summary

We have shown results from a spectroscopic survey of over approximately 100 galaxies in the green valley, i.e., transition objects with intermediate colors between the blue and the red sequences that are believed to be currently quenching their star formation. The data represents the deepest spectra of green valley galaxies ever obtained at intermediate redshifts ($z \sim 0.8$).

By using measurements of spectral indices – namely the break at 4000 Å and the equivalent width of the H_δ absorption line – we are able to infer the star formation histories of these objects, following the method first presented in Martin et al. (2007). If one assumes an exponential decline in star formation rates, it is then possible to measure timescales involved in transitioning from the population of star-forming galaxies into the red sequence. Combined with independent measurements for the number densities in the green valley and typical galaxy masses, we are able to measure the mass flux density between $0.55 < z < 0.9$.

Our measurements have shown that the mass flux density at these redshifts is higher by a factor of ~ 5 than in the low-redshift universe ($z \sim 0.1$). This can be

attributed to two factors: first, the evolution of the luminosity function over the course of the last 6 Gyr, which means at z 0.8 the flux is dominated by the brighter and more massive objects. Second, quenching timescales are shorter at higher redshift, and galaxies transition more rapidly from the blue to the red sequence. In addition, we also show that our results are in good agreement with estimates for the build-up of mass in the red sequence since $z = 1$. We argue for a scenario in which the red sequence is built "from the top-down" meaning that the most massive objects were quenched at earlier times, shifting towards the evolution of less massive galaxies today.

Since we have calculated the quenching timescales of individual objects, the next logical step is to compare our results with other observable properties in the green valley galaxies, in particular merger signatures and AGN activity. We expect this analysis will help clarify the role of each of these processes in the total quenching of star formation, both at low and at high redshifts.

Chapter 5

Conclusion

5.1 Summary

In this work we show recent findings concerning galaxy formation and evolution, in an attempt to clarify general, open questions in the field. How are star-forming galaxies in the early universe different from blue star-forming spirals today? How were they formed? What are the initial conditions, and how does the gas reservoir get converted into stellar mass? After galaxies are formed, how do they evolve into red sequence, passively evolving objects, and how has that evolution changed in the last 6 billion years?

Most of this thesis discusses results for a sample of low-redshift analogs of starburst galaxies commonly found at high redshift – the Lyman break galaxies. These galaxies are defined solely on the basis of ultraviolet luminosity and surface brightness, but our group has shown how other properties – metallicities, morphologies, dust extinction – are more similar to their high-redshift counterparts than to other star forming samples at low redshift. This allows for detailed studies of the star formation and gas assembly in conditions that are common at high redshift, but rare today.

We present results from our integral field survey of these Lyman break analogs (LBAs; Chapter 2). We show how the kinematic properties of the nebular gas in these objects resembles data obtained at higher redshift, providing further evidence these objects are indeed analogs of $z \sim 2$ UV-bright starburst galaxies. Furthermore, we present evidence that these properties are strongly dependent on stellar mass,

and it is likely that most galaxies in the early universe are not rotating disks. We also show that a simple diagnostic for galaxy formation attempting to differentiate between mergers and cold accretion is not appropriate; not only will the resolution and signal-to-noise ratios at high redshift not be enough, but also with particular initial conditions (i.e., high gas fractions) a rotating disk can be formed rapidly from interactions, mimicking predictions for cold flows.

The importance of gas fractions leads to the necessity of measuring gas masses in these objects. We present early results from a 100 hr survey of the CO(1-0) emission in LBAs (Chapter 3). We show that these galaxies, even at the high mass end, have high gas fractions in good agreement with expectations from the Schmidt-Kennicutt relation, supporting the possibility of merger-triggered starbursts. We also compare our sample with other star-forming samples at $z \sim 2$, and we show that LBAs present similar gas properties to those observed at higher redshifts in "normal," less extreme star-forming galaxies. In addition, they are distinct from dusty starburst samples, presenting lower star-formation surface densities for similar gas surface densities, which indicates a different star formation mechanism in each population.

Within a slightly different context, but remaining well within our interest in galaxy evolution, we have probed within the transitioning stage of galaxies at intermediate redshifts ($z \sim 0.8$) evolving from blue, actively star-forming objects to red, passively evolving ones (Chapter 4). Through very deep spectroscopy of these sources, we have inferred star formation histories and quenching timescales. Combined with number density and mass measurements, we were able to infer the amount of stellar mass moving from the blue sequence to the red sequence per unit time, per unit volume. Our results show a rate 5 times higher than seen in the local universe, in good agreement with measurements for the growth of the red sequence. The flux occurs mostly at higher masses than seen today, indicating the red sequence has grown "from the top down": from the bright, massive end, in the past, down to fainter, smaller objects in recent times.

5.2 Future perspectives

The projects described in this thesis comprise a wide range of fields within extragalactic astrophysics and the study of galaxy formation and evolution, and as we have briefly mentioned in the previous chapters, have kindled ideas for a number of new projects meant to continue the research initiated during my PhD. As a matter of fact, in some cases we have already embarked on related work. In this section we describe a few of these new studies and future ideas.

We found that Lyman break analogs show nebular gas kinematic structures reminiscent of rotation disks – particularly so in the more massive objects. The question arises, what is the structure of the underlying stellar mass? Direct measurements of the stellar mass dynamics, even at the redshifts of LBAs, remains a challenge, but we can offer an accurate picture of the stellar mass *distribution* in these objects. In that regard, we have recently initiated a survey to obtain high-resolution, AO-assisted infrared imaging of LBAs with Keck/NIRC2. We have so far observed six objects, and the resolution surpasses that of HST.

Another interesting question concerns the environment of LBAs. In order to make any inference comparing the formation mechanisms of LBAs and LBGs, and in particular the relevance of mergers and interactions in each case, it is of the utmost importance to study the density of the environments where we typically find each population, and the proximity to larger structures such as clusters and filaments. This can be done in two ways: the first is to spectroscopically study the objects that are close to the starburst galaxies in projection, and infer halo masses from the observed velocity dispersion. This project has been started by our team, and we expect to produce results soon. Second, we need to study the connection of LBAs with the large-scale structure. This has been a challenge so far, since we only had 30 objects, which yielded poor statistics. More recently, however, due to upgraded data releases of SDSS and GALEX, we have been able to increase that number to a sample of ~ 700 objects, which can provide us with a much more precise assessment of the connection of LBAs with the large-scale structure of the universe at $z = 0.2$.

In addition, the survey presented in Chapter 3 has raised very interesting questions. Are gas fractions in low-mass objects indeed as high as expected? What is the CO-H_2 conversion factor in these cases? Will they obey the same relations as their high-mass counterparts? These questions represent a technical challenge even at low redshift, since the expected CO fluxes are very small. However, as discussed in that same chapter, we have now an amazing tool to study the molecular gas of high-redshift galaxies: ALMA. We will be able to observe the low-mass objects and, in addition, perform high-resolution mapping of the CO emission in these galaxies. The expectation of comparing gas surface densities and star formation rates at physical scales of 100–200 pc will provide theorists an unparalleled insight into the interplay between gas and star formation in these starbursts.

Finally, with our investigation of the green valley, one of the greatest challenges has been to infer physical properties of galaxies, in particular the dust extinction, without any spectral coverage redward of ~ 5000 Å. This is bound to change after commissioning of the new multi-object infrared spectrograph at Keck, MOSFIRE. MOSFIRE will allow us to measure Hα and [NII] lines of galaxies at intermediate redshifts, which, combined with the existing Hβ and [OIII] measurements, will allow, simultaneously, the determination of dust extinction by use of the Balmer decrement and the inference of AGN activity by use of the BPT diagram. While the first will yield more accurate results regarding the mass flux and number densities in the green valley, the latter will allow a direct comparison between quenching timescales and AGN activity, reinforcing (or disproving) the link between the two at $z \sim 0.8$.

Astronomy today is on the verge of a new revolution, thanks to the upcoming extremely large telescopes (Thirty-Meter Telescope, Giant Magellan Telescope, European Extremely Large Telescope) and space telescope (James Webb Space Telescope), in addition to game-changing interferometers such as ALMA and the Square Kilometer Array. All these new instruments combined will provide a fresh look into galaxies at high redshift, with an unprecedented level of detail. Applying the knowledge we are able to gather at low redshift today, we will soon be able to unveil secrets on the formation of these objects when the universe was in its infancy, getting one step

closer to telling the whole history of the universe since its inception. Which is the modest goal of astronomy, after all.

Appendix A

Appendix

A.1   English translation of poem on page iii

"Oh come now (you will say) hear stars! It's clear

You've lost your mind!" Ill tell you anyway,

I often wake to hear what they will say,

I push my windows open, pale with tear ...

And we converse throughout the night, while high

The Milky Way, like outspread robes, appears

To shine. At dawn, with longing and in tears,

I seek them still throughout the empty sky.

And next you'll say: "My poor, demented friend

What do you say to them? And tell me, pray,

What do they say when they your ears do bend?"

Im tell you: "You must love to comprehend!

For only lie who loves has ears which may

Perceive and grasp the messages stars send."

Translation by Frederick G. Williams

A.2 Resumo em português

Nesta dissertação de doutorado, apresentamos três projetos elaborados com o intuito de esclarecer questões em aberto no campo de formação e evolução de galáxias. Os dois primeiros projetos dizem respeito a uma amostra de galáxias *starburst* com baixa taxa de extinção no universo local ($z \sim 0.2$). Estes objetos são semelhantes a galáxias com altas taxas de formação estelar comuns em alto redshift ($2 \lesssim z \lesssim 3$), e podem auxiliar no entendimento de propriedades típicas observadas em tais épocas. Desta forma, estas galáxias são denominadas análogas de galáxias Lyman break, ou LBA na sigla em inglês.

Em primeiro lugar, descrevemos um estudo sobre a cinemática do gás nebular em LBAs, e como este estudo pode ajudar a explicar o processo de formação destes *starbursts*, incluindo o acúmulo de gás. Mostramos fortes evidências de que a cinemática do gás em LBAs se assemelha fortemente àquela tipicamente encontrada em alto redshift. No entanto, através de observações artificiais de nossa amostra em alto redshift, mostramos como a combinação de baixa resolução e razão sinal ruído em distâncias elevadas pode levar a conclusões errôneas, em particular no que se refere a tentativas de identificar interações e colisões entre galáxias como a origem do *starburst*.

Em seguida, apresentamos resultados de um projeto piloto para estudar o reservatório de gás molecular em LBAs. Novamente, mostramos como as propriedades observadas são análogas àquelas observadas em alto redshift, em particular no que diz respeito à fração de massa bariônica presente na forma de gás, fração esta mais alta do que normalmente encontrada em galáxias semelhantes no universo local. Mostramos também como a correlação entre densidade superficial de gás e a densidade superficial de formação estelar segue a mesma relação que galáxias locais, mas com valores mais elevados.

Finalmente, discutimos um projeto observacional com o objetivo de medir a densidade de fluxo de massa da população de galáxias azuis em direção à população de galáxias vermelhas através do "vale verde" (*green valley* em inglês). Obtemos os espectros mais sensíveis jamais observados de galáxias no *green valley* em redshifts in-

termediários ($z \sim 0.8$), de modo a medir características espectrais que nos permitem inferir o histórico de formação estelar de objetos individuais. A densidade de fluxo de massa medida é mais alta do que aquela encontrada no universo local, de tal forma que a população de galáxias vermelhas estava crescendo mais rapidamente quando o universo tinha metade de sua idade atual.

Bibliography

2000, The American Heritage Dictionary of the English Language (Houghton Mifflin Harcourt), 2076

Aird, James, et al. 2011, eprint arXiv:1107.4368

Arribas, S., Colina, L., Monreal-Ibero, A., Alfonso, J., García-Marín, M., & Alonso-Herrero, A. 2008, Astronomy and Astrophysics, 479, 687

Baker, A. J., Tacconi, L. J., Genzel, R., Lehnert, M. D., & Lutz, D. 2004, Astrophysical Journal, 604, 125

Baldry, I. K., Glazebrook, K., Brinkmann, J., Ivezić, v., Lupton, R. H., Nichol, R. C., & Szalay, A. S. 2004, Astrophysical Journal, 600, 681

Balogh, M. L., Morris, S. L., Yee, H. K. C., Carlberg, R. G., & Ellingson, E. 1999, Astrophysical Journal, 527, 54

Barnes, J. E., & Hernquist, L. E. 1992, Annual Review of Astronomy and Astrophysics, 30, 705

Basu-Zych, A. R., et al. 2009a, Astrophysical Journal, 699, L118

—. 2009b, Astrophysical Journal, 699, 1307

—. 2007, Astrophysical Journal Supplement Series, 173, 457

Baugh, C. M. 2006, Reports on Progress in Physics, 69, 3101

Beckwith, S. V. W., et al. 2006, Astronomical Journal, 132, 1729

Bell, E. F., & de Jong, R. S. 2001, Astrophysical Journal, 550, 212

Bell, E. F., McIntosh, D. H., Katz, N., & Weinberg, M. D. 2003, Astrophysical Journal Supplement Series, 149, 289

Bell, E. F., et al. 2004, Astrophysical Journal, 608, 752

Benson, A. J., & Bower, R. G. 2010, eprint arXiv:1003.0011

Bigiel, F., Leroy, A., Walter, F., Brinks, E., de Blok, W. J. G., Madore, B., & Thornley, M. D. 2008, Astronomical Journal, 136, 2846

Bigiel, F., et al. 2011, eprint arXiv:1102.1720

Blain, A. 2002, Physics Reports, 369, 111

Blanton, M. R., & Roweis, S. 2007, Astronomical Journal, 133, 734

Bouché, N., et al. 2007, Astrophysical Journal, 671, 303

Bournaud, F., et al. 2008, Astronomy and Astrophysics, 486, 741

Bournaud, F., Elmegreen, B. G., & Elmegreen, D. M. 2007, Astrophysical Journal, 670, 237

Bruzual, G. 1983, Astrophysical Journal, 273, 105

Bruzual, G., & Charlot, S. 2003, Monthly Notices of the Royal Astronomical Society, 344, 1000

Bundy, K., et al. 2006, Astrophysical Journal, 651, 120

Bundy, K., Treu, T., & Ellis, R. S. 2007, Astrophysical Journal, 665, L5

Chabrier, G. 2003, Publications of the Astronomical Society of the Pacific, 115, 763

Coil, A. L., et al. 2008, Astrophysical Journal, 672, 153

Combes, F., Garcia-Burillo, S., Braine, J., Schinnerer, E., Walter, F., & Colina, L. 2010, eprint arXiv:1009.2040, 11

Conroy, C., Shapley, A. E., Tinker, J. L., Santos, M. R., & Lemson, G. 2008, Astrophysical Journal, 679, 1192

Conselice, C. J. 2006, Astrophysical Journal, 638, 686

Conselice, C. J., & Arnold, J. 2009, Monthly Notices of the Royal Astronomical Society, 397, 208

Conselice, C. J., Bershady, M. A., Dickinson, M., & Papovich, C. 2003, Astronomical Journal, 126, 1183

Conselice, C. J., et al. 2007, Monthly Notices of the Royal Astronomical Society, 381, 962

Coppin, K. E. K., et al. 2007, Astrophysical Journal, 665, 936

Cowie, L. L., Songaila, A., Hu, E. M., & Cohen, J. G. 1996, Astronomical Journal, 112, 839

Cresci, G., et al. 2009, Astrophysical Journal, 697, 115

Croton, D. J., et al. 2006, Monthly Notices of the Royal Astronomical Society, 365, 11

Curtis, H. D. 1921, Bulletin of the National Research Council, 194

Daddi, E., et al. 2010a, Astrophysical Journal, 713, 686

Daddi, E., Cimatti, A., Renzini, A., Fontana, A., Mignoli, M., Pozzetti, L., Tozzi, P., & Zamorani, G. 2004, Astrophysical Journal, 617, 746

Daddi, E., et al. 2010b, Astrophysical Journal, 714, L118

Davis, M. 2003, Science Objectives and Early Results of the DEEP2 Redshift Survey, Vol. 4834 (SPIE), 161–172

Davis, M., Efstathiou, G., Frenk, C. S., & White, S. D. M. 1985, Astrophysical Journal, 292, 371

Davis, M., et al. 2007, Astrophysical Journal, 660, L1

de Vaucouleurs, G. 1959, Handbuch der Physik, 53

—. 1961, Astrophysical Journal Supplement Series, 5, 233

Dekel, A., & Birnboim, Y. 2006, Monthly Notices of the Royal Astronomical Society, 368, 2

Dekel, A., Sari, R., & Ceverino, D. 2009, Astrophysical Journal, 703, 785

Delgado-Serrano, R., Hammer, F., Yang, Y. B., Puech, M., Flores, H., & Rodrigues, M. 2010, Astronomy and Astrophysics, 509, A78

Denicolo, G., Terlevich, R., & Terlevich, E. 2002, Monthly Notices of the Royal Astronomical Society, 330, 69

Dey, A., et al. 2008, Astrophysical Journal, 677, 943

Di Matteo, T., Springel, V., & Hernquist, L. 2005, Nature, 433, 604

Dib, S., Bell, E., & Burkert, A. 2006, Astrophysical Journal, 638, 797

Downes, D., & Solomon, P. M. 1998, Astrophysical Journal, 507, 615

Dressler, A. 1980, Astrophysical Journal, 236, 351

Eggen, O. J., Lynden-Bell, D., & Sandage, A. R. 1962, Astrophysical Journal, 136, 748

Elmegreen, B. G., Bournaud, F., & Elmegreen, D. M. 2008, Astrophysical Journal, 688, 67

Elmegreen, B. G., & Elmegreen, D. M. 2005, Astrophysical Journal, 627, 632

Elmegreen, B. G., Elmegreen, D. M., Fernandez, M. X., & Lemonias, J. J. 2009, Astrophysical Journal, 692, 12

Erb, D. K., Shapley, A. E., Pettini, M., Steidel, C. C., Reddy, N. A., & Adelberger, K. L. 2006a, Astrophysical Journal, 644, 813

Erb, D. K., Steidel, C. C., Shapley, A. E., Pettini, M., Reddy, N. A., & Adelberger, K. L. 2006b, Astrophysical Journal, 646, 107

Faber, S. M. 2003, in Proceedings of SPIE, Vol. 4841 (SPIE), 1657–1669

Faber, S. M., et al. 2007, Astrophysical Journal, 665, 265

Fall, S. M., & Efstathiou, G. 1980, Royal Astronomical Society, 193, 189

Flores, H., Hammer, F., Puech, M., Amram, P., & Balkowski, C. 2006, Astronomy and Astrophysics, 455, 107

Förster Schreiber, N. M., et al. 2009, Astrophysical Journal, 706, 1364

Fortson, L., et al. 2011, eprint arXiv:1104.5513

Franx, M., et al. 2003, Astrophysical Journal, 587, L79

Gebhardt, K., et al. 2003, Astrophysical Journal, 597, 239

Genel, S., et al. 2008, Astrophysical Journal, 688, 789

Genzel, R., et al. 2008, Astrophysical Journal, 687, 59

—. 2011, eprint arXiv:1106.2098

—. 2010, Monthly Notices of the Royal Astronomical Society, 407, 2091

Giavalisco, M., Steidel, C. C., & Macchetto, F. D. 1996, Astrophysical Journal, 470, 189

Gonçalves, T. S., et al. 2010, Astrophysical Journal, 724, 1373

Gonçalves, T. S., Overzier, R., Basu-Zych, A., & Martin, D. C. 2011, eprint arXiv:1102.1740

Greve, T. R., et al. 2005, Monthly Notices of the Royal Astronomical Society, 359, 1165

Harris, A. I., Baker, A. J., Zonak, S. G., Sharon, C. E., Genzel, R., Rauch, K., Watts, G., & Creager, R. 2010, Astrophysical Journal, 723, 1139

Heckman, T. M., et al. 2005, Astrophysical Journal, 619, L35

Hernquist, L. 1989, Nature, 340, 687

Hoopes, C. G., et al. 2007, Astrophysical Journal Supplement Series, 173, 441

Hopkins, A. M. 2004, Astrophysical Journal, 615, 209

Hopkins, A. M., & Beacom, J. F. 2006, Astrophysical Journal, 651, 142

Hubble, E. P. 1926, Astrophysical Journal, 64, 321

—. 1927, The Observatory, 50, 276

Hubble, E. P. 1925, The Observatory, 48, 139

Huchra, J., Davis, M., Latham, D., & Tonry, J. 1983, Astrophysical Journal Supplement Series, 52, 89

Immeli, A., Samland, M., Gerhard, O., & Westera, P. 2004, Astronomy and Astrophysics, 413, 547

Jones, T., Swinbank, M., Ellis, R., Richard, J., & Stark, D. 2010, Monthly Notices of the Royal Astronomical Society, 404, 1247

Kauffmann, G., et al. 2003, Monthly Notices of the Royal Astronomical Society, 341, 33

Kennicutt, J. 1998, Astrophysical Journal, 498, 541

Kereš, D., Katz, N., Fardal, M., Davé, R., & Weinberg, D. H. 2009, Monthly Notices of the Royal Astronomical Society, 395, 160

Kewley, L. J., & Ellison, S. L. 2008, Astrophysical Journal, 681, 1183

Kormendy, J., & Fisher, D. B. 2005, The Ninth Texas-Mexico Conference on Astrophysics (Eds. S. Torres-Peimbert & G. MacAlpine) Revista Mexicana de Astronomía y Astrofísica (Serie de Conferencias) Vol. 23, 23, 101

Kormendy, J., & Kennicutt, R. C. 2004, Annual Review of Astronomy and Astrophysics, 42, 603

Koyama, Y., Kodama, T., Nakata, F., Shimasaku, K., & Okamura, S. 2011, eprint arXiv:1103.2180, 14

Krajnovic, D., Cappellari, M., de Zeeuw, P. T., & Copin, Y. 2006, Monthly Notices of the Royal Astronomical Society, 366, 787

Krumholz, M. R., McKee, C. F., & Tumlinson, J. 2009, Astrophysical Journal, 699, 850

Larkin, J., et al. 2006, in Proceedings of the SPIE, ed. I. S. McLean & M. Iye, Vol. 6269 (Orlando, FL, USA: SPIE), 42

Law, D. R., Steidel, C. C., & Erb, D. K. 2006, Astronomical Journal, 131, 70

Law, D. R., Steidel, C. C., Erb, D. K., Larkin, J. E., Pettini, M., Shapley, A. E., & Wright, S. A. 2007a, Astrophysical Journal, 669, 929

—. 2009, Astrophysical Journal, 697, 2057

Law, D. R., Steidel, C. C., Erb, D. K., Pettini, M., Reddy, N. A., Shapley, A. E., Adelberger, K. L., & Simenc, D. J. 2007b, Astrophysical Journal, 656, 1

Leavitt, H. S. 1908, Annals of Harvard College Observatory, 60

Lehnert, M. D., Nesvadba, N. P. H., Tiran, L. L., Matteo, P. D., van Driel, W., Douglas, L. S., Chemin, L., & Bournaud, F. 2009, Astrophysical Journal, 699, 1660

Leroy, A. K., et al. 2011, eprint arXiv:1102.4618

Leroy, A. K., Walter, F., Brinks, E., Bigiel, F., de Blok, W. J. G., Madore, B., & Thornley, M. D. 2008, Astronomical Journal, 136, 2782

López-Sanjuan, C., et al. 2010, eprint arXiv:1009.5921

Lotz, J. M., Jonsson, P., Cox, T. J., & Primack, J. R. 2008, Monthly Notices of the Royal Astronomical Society, 391, 1137

Lotz, J. M., Madau, P., Giavalisco, M., Primack, J., & Ferguson, H. C. 2006, Astrophysical Journal, 636, 592

Madau, P., Ferguson, H. C., Dickinson, M. E., Giavalisco, M., Steidel, C. C., & Fruchter, A. 1996, Monthly Notices of the Royal Astronomical Society, 283, 1388

Madgwick, D. S., et al. 2002, Monthly Notices of the Royal Astronomical Society, 333, 133

Magdis, G. E., Rigopoulou, D., Huang, J.-S., & Fazio, G. G. 2010, Monthly Notices of the Royal Astronomical Society, 401, 1521

Maraston, C., Pforr, J., Renzini, A., Daddi, E., Dickinson, M., Cimatti, A., & Tonini, C. 2010, Monthly Notices of the Royal Astronomical Society, 407, 830

Martin, D. C., et al. 2005, Astrophysical Journal, 619, L1

—. 2007, Astrophysical Journal Supplement Series, 173, 342

Masters, K. L., et al. 2011, American Astronomical Society, 43

Menci, N., Fontana, A., Giallongo, E., & Salimbeni, S. 2005, Astrophysical Journal, 632, 49

Mendez, A. J., Coil, A. L., Lotz, J., Salim, S., Moustakas, J., & Simard, L. 2011, Astrophysical Journal, 736, 110

Mo, H. J., Mao, S., & White, S. D. M. 1998, Monthly Notices of the Royal Astronomical Society, 295, 319

Monreal-Ibero, A., Arribas, S., Colina, L., Rodriguez-Zaurin, J., Alonso-Herrero, A., & Garcia-Marin, M. 2010, eprint arXiv:1004.3933

Nandra, K., et al. 2007, Astrophysical Journal, 660, L11

Nesvadba, N. P. H., et al. 2006, Astrophysical Journal, 650, 661

Noeske, K. G., et al. 2007, Astrophysical Journal, 660, L43

Noguchi, M. 1999, Astrophysical Journal, 514, 77

Osterbrock, D. E., & Ferland, G. J. 2006, Astrophysics of gaseous nebulae and active galactic nuclei (University Science Books)

Overzier, R. A., et al. 2008, Astrophysical Journal, 677, 37

Overzier, R. A., Heckman, T. M., Schiminovich, D., Basu-Zych, A. R., Gonçalves, T. S., Martin, D. C., & Rich, R. M. 2010, Astrophysical Journal, 710, 979

Overzier, R. A., et al. 2009, Astrophysical Journal, 706, 203

Papovich, C., Dickinson, M., Giavalisco, M., Conselice, C. J., & Ferguson, H. C. 2005, Astrophysical Journal, 631, 101

Peebles, P. J. E. 1982, Astrophysical Journal, 263, L1

PérezGonzález, P. G., Trujillo, I., Barro, G., Gallego, J., Zamorano, J., & Conselice, C. J. 2008, Astrophysical Journal, 687, 50

Pettini, M., Shapley, A. E., Steidel, C. C., Cuby, J., Dickinson, M., Moorwood, A. F. M., Adelberger, K. L., & Giavalisco, M. 2001, Astrophysical Journal, 554, 981

Polletta, M., Nesvadba, N. P. H., Neri, R., Omont, A., Berta, S., & Bergeron, J. 2011, eprint arXiv:1107.2129

Prochaska, L. C., Rose, J. A., Caldwell, N., Castilho, B. V., Concannon, K., Harding, P., Morrison, H., & Schiavon, R. P. 2007, Astronomical Journal, 134, 321

Puech, M. 2010, Monthly Notices of the Royal Astronomical Society, 406, 535

Reddy, N. A., & Steidel, C. C. 2009, Astrophysical Journal, 692, 778

Reid, I. N., et al. 1991, Publications of the Astronomical Society of the Pacific, 103, 661

Riechers, D. A., Carilli, C. L., Walter, F., & Momjian, E. 2010, Astrophysical Journal, 724, L153

Riechers, D. A., et al. 2009, Astrophysical Journal, 703, 1338

Robertson, B., Bullock, J. S., Cox, T. J., Di Matteo, T., Hernquist, L., Springel, V., & Yoshida, N. 2006, Astrophysical Journal, 645, 986

Robertson, B. E., & Bullock, J. S. 2008, Astrophysical Journal, 685, L27

Sales, L. V., Navarro, J. F., Schaye, J., Dalla Vecchia, C., Springel, V., Haas, M. R., & Helmi, A. 2009, Monthly Notices of the Royal Astronomical Society: Letters, 399, L64

Salim, S., et al. 2005, Astrophysical Journal, 619, L39

—. 2009, Astrophysical Journal, 700, 161

Sandage, A. 1961, Washington: Carnegie Institution

Sanders, D. B., & Mirabel, I. F. 1996, Annual Review of Astronomy and Astrophysics, 34, 749

Sanders, D. B., Soifer, B. T., Elias, J. H., Madore, B. F., Matthews, K., Neugebauer, G., & Scoville, N. Z. 1988, Astrophysical Journal, 325, 74

Schawinski, K., Virani, S., Simmons, B., Urry, C. M., Treister, E., Kaviraj, S., & Kushkuley, B. 2009, Astrophysical Journal, 692, L19

Schmidt, M. 1959, Astrophysical Journal, 129, 243

—. 1963, Nature, 197, 1040

Shapiro, K. L., et al. 2008, Astrophysical Journal, 682, 231

Shapley, A. E. 2011, eprint arXiv:1107.5060

Shapley, H. 1921, Bulletin of the National Research Council, 171

Silk, J. 1997, Astrophysical Journal, 481, 703

Smoot, G. F., et al. 1992, Astrophysical Journal, 396, L1

Solomon, P., & Vanden Bout, P. 2005, Annual Review of Astronomy and Astrophysics, 43, 677

Solomon, P. M., & Barrett, J. W. 1991, Dynamics of Galaxies and Their Molecular Cloud Distributions, 146, 235

Spergel, D. N., et al. 2007, Astrophysical Journal Supplement Series, 170, 377

Springel, V., et al. 2005, Nature, 435, 629

Steidel, C. C., Adelberger, K. L., Shapley, A. E., Pettini, M., Dickinson, M., & Giavalisco, M. 2003, Astrophysical Journal, 592, 728

Steidel, C. C., Giavalisco, M., Pettini, M., Dickinson, M., & Adelberger, K. L. 1996, Astrophysical Journal, 462, L17

Steidel, C. C., Shapley, A. E., Pettini, M., Adelberger, K. L., Erb, D. K., Reddy, N. A., & Hunt, M. P. 2004, Astrophysical Journal, 604, 534

Tacconi, L. J., et al. 2010, Nature, 463, 781

—. 2008, Astrophysical Journal, 680, 246

Taniguchi, Y., & Shioya, Y. 2001, Astrophysical Journal, 547, 146

Thilker, D. A., et al. 2010, Astrophysical Journal, 714, L171

Ueda, Y., Akiyama, M., Ohta, K., & Miyaji, T. 2003, Astrophysical Journal, 598, 886

van Dam, M. A., et al. 2006, Publications of the Astronomical Society of the Pacific, 118, 310

van den Bergh, S. 2002, Publications of the Astronomical Society of the Pacific, 114, 797

Veilleux, S., Kim, D., & Sanders, D. B. 2002, Astrophysical Journal Supplement Series, 143, 315

Weiß, A., Downes, D., Neri, R., Walter, F., Henkel, C., Wilner, D. J., Wagg, J., & Wiklind, T. 2007, Astronomy and Astrophysics, 467, 955

White, S. D. M., & Rees, M. J. 1978, Royal Astronomical Society, 183, 341

Williams, R. E., et al. 1996, Astronomical Journal, 112, 1335

Willmer, C. N. A., et al. 2006, Astrophysical Journal, 647, 853

Wizinowich, P. L., et al. 2006, Publications of the Astronomical Society of the Pacific, 118, 297

Wolfire, M. G., Hollenbach, D., & McKee, C. F. 2010, Astrophysical Journal, 716, 1191

Wright, S. A., Larkin, J. E., Law, D. R., Steidel, C. C., Shapley, A. E., & Erb, D. K. 2009, Astrophysical Journal, 699, 421

Wyder, T. K., et al. 2007, Astrophysical Journal Supplement Series, 173, 293

Zakamska, N. L. 2010, Nature, 465, 60